LUND UNIVERSITY

Synchrotron X-ray based characterization of technologically relevant III-V surfaces and nanostructures

Troian, Andrea

2019

Synchrotron X-ray based characterization of technologically relevant III-V surfaces and nanostructures

ANDREA TROIAN
DEPARTMENT OF PHYSICS | FACULTY OF SCIENCE | LUND UNIVERSITY

Synchrotron X-ray based characterization of technologically relevant III-V surfaces and nanostructures

Synchrotron X-ray based characterization of technologically relevant III-V surfaces and nanostructures

Andrea Troian

LUND
UNIVERSITY

DOCTORAL DISSERTATION
by due permission of the Faculty of Science, Lund University, Sweden.
To be defended in Lund, Lundmarksalen, Astronomihuset, Sölvegatan 27, on the
12th of April 2019 at 09:15.

Faculty opponent
Prof. Andrew C. Kummel
University of California, San Diego, CA, USA.

Organization LUND UNIVERSITY	Document name: DOCTORAL DISSERTATION
	Date of disputation: 2019-04-12
Author(s): Andrea Troian	Sponsoring organization

Title and subtitle: Synchrotron X-ray based characterization of technologically relevant III-V surfaces and nanostructures

Abstract

Innovative design and materials are needed to satisfy the demand for efficient and scalable devices for electronic and opto-electronic applications, such as transistors, LEDs, and solar cells. Nanostructured III-V semiconductors are an appealing solution, combining the excellent functional properties of III-V materials with the flexibility typical of nanostructures, such as the nanowires (NWs) studied here. However, there are a number of open challenges, that currently hinder the performance of III-V nanostructure devices: first, the surface quality of III-V materials is still one of their main limiting factors. Other problems specific of III-V NWs are the control of dopant incorporation - crucial for their functionalization -, and of their structural inhomogeneity (e.g. lattice strain and tilt), that can affect opto-electronic performance. These problematics require a set of non-trivial cutting-edge characterization tools: here an approach based on a combination of X-ray synchrotron techniques is demonstrated.

Synchrotron based X-ray photoelectron spectroscopy (XPS) has been used to study the surface chemistry of III-V model systems and to monitor industrially relevant processing on them. A new passivation process improving the surface quality of InAs substrates used for electronics has been investigated: the surface structure and composition resulting from thermal oxidation followed by ex situ deposition of a high-k material via atomic layer deposition (ALD) has been assessed with XPS. The implementation of this passivation approach in gate stacks showed improvements in performance, that were attributed to the specific stoichiometry of the thermal oxide. The dynamics of the ALD process on InAs was also studied in situ with ambient pressure XPS: it was observed that the chemisorption of the precursor is an important step to ensure a good quality of the high-k oxide deposition.

Dopant evaluation in NWs is challenging due to their small dimensions. Here, a first approach to this problem was to perform XPS to study the effects of Zn dopant incorporation on the surface of GaAs NWs, used for solar cells. High doping conditions during growth were found to form a Zn layer on the outside of the NW that suppresses the native oxides, which are generally a cause of poor passivation of III-V surfaces. In another experiment, XPS scanning microscopy was used to study surface Zn doping in an InP NW with an axial pn junction, also used for solar cells. The surface potential drop along the junction was monitored in operando, while applying a bias to the NW device, and it was found smaller than what expected for the bulk. Finally, a quantitative evaluation of Zn dopants incorporation in III-V NWs was studied for the first time with nano-focused X-ray fluorescence, due to the excellent combination of low detection limits and spatial resolution. Dopant gradients and memory effects were noted along InP and InGaP NWs, showing complex dopant incorporation mechanisms during the growth.

The structural inhomogeneity in InGaN nano-pyramids for next generation LEDs was also investigated. The influence of different processing parameters on lattice and strain were studied with full field X-ray diffraction microscopy. This imaging technique uses Bragg diffraction intensity as contrast mechanism and has a large field of view, useful for imaging at once large areas patterned with pyramids, giving valuable statistical consistency. The growth parameters providing the best lattice quality and homogeneity were assessed.

This thesis shows how cutting edge synchrotron characterization methods can provide useful information for improving III-V surfaces and nanostructures for next generation devices. Moreover, in most cases advances in the characterization methods are achieved, that can be relevant also in other and broader scientific fields.

Key words: synchrotron radiation, III-V semiconductors, high-k oxides, passivation, doping, XPS, AP-XPS, SPEM, XRF, Full field X-ray diffraction microscopy

Classification system and/or index terms (if any)

Supplementary bibliographical information		Language English
ISSN and key title		ISBN (print): 978-91-7753-978-0 ISBN (pdf): 978-91-7753-979-7
Recipient's notes	Number of pages 131	Price
	Security classification	

Signature  Date 2019-03-04

Synchrotron X-ray based characterization of technologically relevant III-V surfaces and nanostructures

Andrea Troian

LUND
UNIVERSITY

Front cover: false color map of an array of InGaN nanopyramids, measured with full field X-ray diffraction microscopy.

Back cover: optical microscope image of a sample holder for cross-sectional STM with a cleaved GaAs wafer sample.

Division of Synchrotron Radiation Research
Department of Physics, Faculty of Science
Lund University
SE-221 00, Lund
Sweden

ISBN 978-91-7753-978-0 (Print)
978-91-7753-979-7 (Pdf)

Printed in Sweden by Media-Tryck, Lund University
Lund 2019

Table of Contents

Abstract

Innovative design and materials are needed to satisfy the demand for efficient and scalable devices for electronic and opto-electronic applications, such as transistors, LEDs, and solar cells. Nanostructured III-V semiconductors are an appealing solution, combining the excellent functional properties of III-V materials with the flexibility typical of nanostructures, such as the nanowires (NWs) studied here. However, there are a number of open challenges, that currently hinder the performance of III-V nanostructure devices: first, the surface quality of III-V materials is still one of their main limiting factors. Other problems specific of III-V NWs are the control of dopant incorporation - crucial for their functionalization -, and of their structural inhomogeneity (e.g. lattice strain and tilt), that can affect opto-electronic performance. These problematics require a set of non-trivial cutting-edge characterization tools: here an approach based on a combination of X-ray synchrotron techniques is demonstrated.

Synchrotron based X-ray photoelectron spectroscopy (XPS) has been used to study the surface chemistry of III-V model systems and to monitor industrially relevant processing on them. A new passivation process improving the surface quality of InAs substrates used for electronics has been investigated: the surface structure and composition resulting from thermal oxidation followed by ex situ deposition of a high-k material via atomic layer deposition (ALD) has been assessed with XPS. The implementation of this passivation approach in gate stacks showed improvements in performance, that were attributed to the specific stoichiometry of the thermal oxide. The dynamics of the ALD process on InAs was also studied in situ with ambient pressure XPS: it was observed that the chemisorption of the precursor is an important step to ensure a good quality of the high-k oxide deposition.

Dopant evaluation in NWs is challenging due to their small dimensions. Here, a first approach to this problem was to perform XPS to study the effects of Zn dopant incorporation on the surface of GaAs NWs, used for solar cells. High doping conditions during growth were found to form a Zn layer on the outside of the NW that suppresses the native oxides, which are generally a cause of poor passivation of III-V surfaces. In another experiment, XPS scanning microscopy was used to study surface Zn doping in an InP NW with an axial pn junction, also used for solar cells. The surface potential drop along the junction was monitored in operando, while applying a bias to the NW device, and it was found smaller than what expected for the bulk. Finally, a quantitative evaluation of Zn dopants incorporation in III-V NWs was studied for the first time with nano-focused X-ray fluorescence, due to the excellent combination of low detection limits and spatial resolution. Dopant gradients and memory effects were noted along InP and InGaP NWs, showing complex dopant incorporation mechanisms during the growth.

The structural inhomogeneity in InGaN nano-pyramids for next generation LEDs was also investigated. The influence of different processing parameters on lattice and strain were studied with full field X-ray diffraction microscopy. This imaging technique uses Bragg diffraction intensity as contrast mechanism and has a large field of view, useful for imaging at once large areas patterned with pyramids, giving valuable statistical consistency. The growth parameters providing the best lattice quality and homogeneity were assessed.

This thesis shows how cutting edge synchrotron characterization methods can provide useful information for improving III-V surfaces and nanostructures for next generation devices. Moreover, in most cases advances in the characterization methods are achieved, that can be relevant also in other and broader scientific fields.

Populärvetenskaplig sammanfattning

En studie publicerad av NASA:s Goddard Institute for Space Studies år 2019 visade att de genomsnittliga globala temperaturerna under de senaste fyra åren (2015-2018) var de högsta som någonsin registrerats i människans historia. Den nyheten passar väl in i de alarmerande prognoserna om global uppvärmning, och kräver snabba och radikala handlingar. Att studera "tekniskt relevanta III-V halvledares nanostrukturer och ytor med hjälp av synkrotronljus", som är en omformulering av denna avhandlings titel, syftar till att ge ett litet bidrag till denna fråga. Det är dock svårt att se ett enkelt samband mellan titeln och den globala uppvärmningen. Att klargöra avhandlingens beståndsdelar kan kanske hjälpa till att belysa kopplingen.

Halvledare, som t.ex. kisel (Si), är material som finns närvarande i hela vårat vardagsliv. De har två typer av laddningar som rör sig inuti: elektroner (negativa) och "hål" (positiva). Genom att lägga till orenheter som kallas "dopants" i halvledare, kan man få "*n*-dopning" när de flesta av laddningar är elektroner, eller "*p*-dopning" när de är hål, beroende på dopant. *p* och *n* dopade halvledare kan kombineras för att skapa dioder och transistorer, som ofta används i datorer. Dessutom kan, i lysdioder (mer kända som LEDs), hål och elektroner återförenas och generera fotoner, som producerar ljus. Halvledare är också avgörande för att fånga upp solenergi: fotoner kan generera ström och denna effekt utnyttjas i solceller.

Framsteg inom halvledarteknik kan ha stor inverka på miljön: genom att öka prestandan hos apparaterna kan energiförbrukningen minskas markant, samtidigt som effektivare solceller kan ge renare energi.

I den här avhandlingen studeras prover av klass III-V halvledare som är nära att bli tillämpningsbara. III-V:er är föreningar av två (eller flera) element, en som tillhör III-gruppen (t.ex. In, Ga, och Al) och en av V-gruppen (t.ex. N, As, och P) av den periodiska tabellen. III-V halvledare har enastående ledningsförmåga och effektiva egenskaper för att generera ljus. Detta gör dem till perfekta kandidater för framtida enheter: till exempel är indiumarsenid (InAs) optimalt för transistorer, indiumfosfat (InP) för solceller och indiumgalliumnitrid (InGaN) för LEDs.

III-V:er har faktiskt varit kända under lång tid och undersökts redan före Si. Anledningen till att de inte har ersatt Si beror främst på den relativt höga kostnaden och den dåliga kvaliteten på deras ytor, vilket är avgörande för elektronik och solceller. Under de senaste decennierna, har forskning om dessa material upplevt en renässans, på grund av nya metoder för att förbättra ytorna och också för möjligheten att tillverka III-V halvledare som nanostrukturer, som t.ex. nanotrådar (NW) som studeras i denna avhandling. NWs är nålformade objekt som är cirka en mikrometer (1 μm = 0,000001 m) långa och med diametrar på cirka 30-200 nanometer (1 nm = 0,001 μm). De erbjuder en mycket flexibel grund för att

kombinera olika III-V material utan att producera stora deformationsfält (som kan hämma prestandan) i samma nanostruktur. Många fysiska processer, som laddningstransport, är i sig effektivare i NWs än i materialets normala storlek.

För att utveckla banbrytande effektiva nanostrukturenheter behövs dock en fullständig förståelse av fysiken bakom dem. Framsteg måste uppnås i deras behandling genom att 1) förbättra ytkvaliteten, 2) kontrollera NW-dopningen, 3) övervaka den strukturella deformationen.

Karaktärisering av III-V ytor och NWs är därför nödvändigt, men detta är extremt utmanande på grund av deras ringa storlekar. Avhandlingen föreslår ett steg framåt i denna riktning genom att använda en kombination av avancerade tekniker baserade på röntgenljus från en synkrotronkälla. Röntgenljus som produceras av en synkrotron - en cyklisk partikelaccelerator - är optimala på grund av dess mycket höga intensitet, som är utmärkt för detaljerade kemiska och strukturella analyser och även mikroskopi, när ljusstrålen är ordentligt fokuserad.

En ny behandling för att förbättra kvaliteten på InAs-ytor undersöktes med en teknik som kallas fotoelektronspektroskopi (XPS). Denna metod är baserad på insamling av provelektroner som matas ut av röntgenljuset, som fungerar som kemiska fingeravtryck. Genom att utveckla denna teknik, studerades den ytkemiska utvecklingen under depositionen av ett högkvalitativt oxidskikt i realtid. Resultaten visade de viktiga aspekterna i denna behandling. XPS användes också för att studera dopants på NWs ytor, som visade sig ha en stark effekt på ytan egenskaper.

Resultatet av dopning i NWs är generellt svårt att förutsäga och mäta. För första gången har en röntgenstråle med ett fokus på bara några tiotals nanometer använts för att kartlägga dopants-distribution i III-V NWs. Dopants räknades tack vare deras emission av karakteristiskt röntgenljus, en effekt som kallas fluorescens. Resultaten är användbara för att förstå hur man optimerar tillverkningen för att få den önskade dopants-distributionen för effektiva NW-solceller.

Slutligen studerades de deformationsseffekter som orsakas av tillverkning av NWs-mönster som används för LEDs med en teknik som kallas full field röntgens-diffraktionsmikroskopi. Denna metod är baserad på diffraktion, en reflektion av röntgenstrålar som endast förekommer i specifika riktningar, beroende på atomavståndet, som självt beror på deformation. För första gången erhölls bilder på InGaN NW-mönster med kontrasten som ges av deras olika deformationer. Denna studie hjälper till att hitta de bästa parametrarna för att tillverka högkvalitativa NW LEDs.

Denna avhandling utforskar ett brett spektrum av viktiga aspekter i specifika III-V nanostrukturer. Användningen av moderna röntgenkarakteriseringsverktyg syftar till att ge konkreta svar för att förbättra dessa material och enheter, med förhoppningen att göra dem mer effektiva.

Popular science summary

A study published by the Goddard Institute for Space Studies of NASA in 2019 put in evidence that the average global temperatures of the last four years (2015-2018) were the highest ever recorded in human history. This recent news fits well into the alarming forecasts on global warming, demanding prompt and radical interventions. Studying "technologically relevant III-V semiconductor nanostructures and surfaces with techniques based on synchrotron radiation", which is a rephrasing of the title of this thesis, aims to give a little contribution to this issue. Apparently, there is not a straightforward connection between the title and the global warming: a clarification on the elements of this thesis can help in highlighting the link.

Semiconductors, like for instance silicon (Si), are materials present in almost all aspects of our everyday life. They have two different types of charges that can move in the solid: electrons (negative) and "holes" (positive). By adding impurities called "dopants" into semiconductors, one can obtain "*n* type doping" when most of the charge carriers are electrons, or "*p* type doping" when they are holes, depending on the dopant. *p* and *n* doped semiconductors can be combined together to create diodes and transistors, widely used in computers. Moreover, in the class of the light emitting diodes, better known as LEDs, holes and electrons can recombine together generating photons, that is producing light. Semiconductors are also crucial in harvesting solar energy: the photons can generate a current and this effect is exploited in solar cells.

Advances in semiconductor technology can have a big impact for the environment: by boosting the performance of devices, the energy consumption can be sensibly decreased, while more efficient solar cells can provide more clean energy.

Here, samples of the class of the III-V semiconductors close to realistic applications are studied. III-Vs are compounds of two (or more) elements, one belonging to the III group (for example In, Ga, and Al) and one of the V group (for example N, As, and P) of the periodic table. III-V semiconductors have outstanding charge transport and charge-photon conversion properties, making them perfect candidates for future devices: for example, indium arsenide (InAs) is optimal for transistors, indium phosphate (InP) for solar cells and indium gallium nitride (InGaN) for LEDs.

III-Vs have actually been known for a long time and investigated even before Si. The reason why they have not supplanted Si is mainly due to the relatively high cost and to the poor quality of their surfaces, which is crucial for electronics and solar cells. In the last decades, the research on these materials experienced a renaissance, due to new methods for improving the surfaces and especially for the possibility of implementing III-V semiconductors in nanostructures, like for instance the nanowires (NW) studied in this thesis. NWs are needle shaped objects ca. 1 micron (1 μm = 0.000001 m) long and with diameters of ca. 30-200 nanometers (1 nm =

0.001 μm), and they offer a very flexible platform to combine different III-V materials avoiding large strain fields (that can hamper performances) in the same nanostructure. Many physical processes, like charge transport, are intrinsically more efficient in NWs than in their bulk counterpart.

However, for developing cutting-edge efficient nanostructure devices, a complete understanding of the physics behind them is still needed. Advances need to be achieved in their processing by 1) improving the surface quality, 2) controlling the NW doping, 3) monitoring the structural strain.

A characterization of III-V surfaces and NWs is therefore needed, but this is very challenging due to their small size. This thesis proposes a step forward in this direction by using a combination of advanced techniques based on X-rays from a synchrotron source. The X-rays produced by a synchrotron - a cyclic particle accelerator - are ideal because of their very high intensity, excellent for detailed chemical and structural analyses and even microscopy, when focused properly.

A new processing to improve the quality of InAs surfaces was investigated with a technique called synchrotron based X-ray photoelectron spectroscopy (XPS). This method is based on the collection of the sample electrons ejected by the X-rays, acting as chemical fingerprint. By pushing this technique to its limits, the surface chemistry evolution during the deposition of a high quality oxide layer was studied in real time. The results showed the critical aspects in this industrially relevant processing. XPS was also used for studying the dopants on the surface of NWs, that were found to have a strong effect on the surface properties.

The doping incorporation in NWs is in general difficult to predict and measure. For the first time, an X-ray beam with a focal spot of only few tens of nanometers was used to map the dopant distribution in III-V NWs. The dopants were identified and counted thanks to their emission of characteristic X-rays, an effect called fluorescence. The results are useful to understand how to tailor the processing to have the desired dopant distribution for very efficient NW solar cells.

Finally, the strain effects caused by patterning arrays of NWs used for LEDs were studied with a technique called full field X-ray diffraction microscopy. This method is based on diffraction, a selective reflection of X-rays that occurs only in specific directions, depending on the atomic spacing: if there is strain, the atomic spacing (and the diffraction angle) is different. For the first time, images of InGaN NW arrays were obtained with the contrast given by their different strain. This study helps to find the optimal parameters for fabricating high quality NW LEDs.

This thesis explores a wide range of criticalities in specific III-V nanostructures. The use of modern X-ray based characterization tools is aimed to give concrete answers to improve these materials and devices, with the hope of making them more energetically efficient.

List of papers

This doctoral thesis is based on the following papers, which will be referred to in the text by their Roman numerals.

Paper I

Surface smoothing and native oxide suppression on Zn doped aerotaxy GaAs nanowires

S. Yngman, S. R. McKibbin, J. V. Knutsson, **A. Troian**, F. Yang, M. H. Magnusson, L. Samuelson, R. Timm and A. Mikkelsen

Journal of Applied Physics **2019,** *125* (2), 025303.

I took part in the XPS experiment and contributed to the discussion of the manuscript.

Paper II

InAs-oxide interface composition and stability upon thermal oxidation and high-k atomic layer deposition

A. Troian, J. V. Knutsson, S. R. McKibbin, S. Yngman, A. S. Babadi, L.-E. Wernersson, A. Mikkelsen and R. Timm

AIP Advances **2018,** *8* (12), 125227

I took part in the experiment planning and in the XPS, STM, and LEED experiment, I did the data analysis and I was the main responsible for writing the manuscript.

Paper III

Self-cleaning and surface chemical reactions during hafnium dioxide atomic layer deposition on indium arsenide

R. Timm, A. R. Head, S. Yngman, J. V. Knutsson, M. Hjort, S. R. McKibbin, **A. Troian**, O. Persson, S. Urpelainen, J. Knudsen, J. Schnadt and A. Mikkelsen

Nature Communications **2018**, 9 (1), 1412.

I took part in the AP-XPS experiment and I contributed to the discussion of the manuscript.

Paper IV

Operando surface characterization of an InP p-n junction nanowire diode
S. R. McKibbin, J. V. Knutsson, J. Colvin, **A. Troian**, J. Webb, G. Otnes, K. Dirscherl, H. Sezen, M. Amati, L. Gregoratti, M. Borgström, A. Mikkelsen and R. Timm

In manuscript

I took part in the experiment planning and in the SPEM experiment, and I contributed to the discussion of the manuscript.

Paper V

Nanobeam X-ray Fluorescence Dopant Mapping Reveals Dynamics of in Situ Zn-Doping in Nanowires
A. Troian, G. Otnes, X. Zeng, L. Chayanun, V. Dagytė, S. Hammarberg, D. Salomon, R. Timm, A. Mikkelsen, M. T. Borgström and J. Wallentin

Nano Letters **2018,** *18* (10), 6461-6468.

Selected for "ESRF highlights 2018"

I took part in the experiment planning and in the nano-XRF experiment, I did the nano-XRF data analysis and I was the main responsible for writing the manuscript.

Paper VI

Lattice Tilt Mapping using Full Field Diffraction X-Ray Microscopy at ID01 ESRF

T. Zhou, T. Stankevic, **A. Troian**, Z. Ren, Z. Bi, J. Ohlsson, L. Samuelson, J. Hilhorst, T. Schulli, A. Mikkelsen and O. Balmes

Microscopy and Microanalysis **2018,** *24* (S2), 126-127

I took part in the experiment planning and in the FFXDM experiment and I contributed to the manuscript discussion.

Paper VII

Full field X-ray diffraction imaging of structural variations in arrays of InGaN nanopyramids

A. Troian, Z. Ren, T. Zhou, T. Stankevic, R. Timm, Z. Bi, J. Ohlsson, L. Samuelson, J. Hilhorst, T. Schulli, O. Balmes, and A. Mikkelsen

In manuscript

I took part in the experiment planning and in the FFXDM experiment, I did the FFXDM data analysis and I was the main responsible for the manuscript writing.

Publications to which I contributed that are not included in this dissertation:

Paper VIII

A. Troian, L. Rebuffi, M. Leoni, P. Scardi, Toward a reference material for line profile analysis. *Powder Diffraction* **2015,** *30* (S1), S47-S51.

Paper IX

L. Rebuffi, **A. Troian**, R. Ciancio, E. Carlino, A. Amimi, A. Leonardi, P. Scardi, On the reliability of powder diffraction Line Profile Analysis of plastically deformed nanocrystalline systems. *Scientific Reports* **2016,** *6*, 20712

Paper X

L. Chayanun, V. Dagytė, **A. Troian**, D. Salomon, M. T. Borgström, J. Wallentin, Spectrally resolved x-ray beam induced current in a single InGaP nanowire. *Nanotechnology* **2018,** *29* (45), 454001.

Paper XI

L. Chayanun, G. Otnes, **A. Troian**, S. Hammarberg, D. Salomon, M. T. Borgstrom, J. Wallentin, Nanoscale mapping of carrier collection in single nanowire solar cells using X-ray beam induced current. *Journal of Synchrotron Radiation* **2019,** *26* (1)

List of recurrent acronyms and symbols

ALD	Atomic layer deposition
AP-XPS	Ambient pressure X-ray photoemission spectroscopy
CB	Condution band
CDI	Coherent diffraction imaging
CRL	Compound refractive lens
E_b	Binding energy
EDS	Energy dispersive X-ray spectroscopy
EEA	Electron energy analyzer
E_f	Fermi level
E_k	Kinetic energy
FFXDM	Full field X-ray diffraction microscopy
FoV	Field of view
FZP	Fresnel zone plate
HSB	Hue-saturation-brightness
IMFP	Inelastic mean free path
LED	Light emitting diode
LEED	Low energy electron diffraction
MCP	Micro channel plate
MOSFET	Metal oxide semiconductor field effect transistor
MOVPE	Metal organic vapor phase epitaxy
nano-XRF	Nanofocused X-ray fluorescence microscopy
NW	Nanowire
PEEM	Photoemission electron microscopy
QCSE	Quantum confined Stark effect
SAE	Selected area epitaxy
SPEM	Scanning photoemission microscopy/microscope
SPV	Surface photovoltage
STM	Scanning tunneling microscopy/microscope
TDMA-Hf	Tetrakis-dimethylamino hafnium
TMA	trimethylaluminum
UHV	Ultra high vacuum
VB	Valence band
Wz	Wurtzite
XPS	X-ray photoemission spectroscopy

XRD	X-ray diffraction
XRF	X-ray fluorescence
Zb	Zinc blende
κ	Permittivity (also referred as k)

Acknowledgements

A thesis usually has the name of only one author on the front page: this does not entirely reflect the truth, since a thesis is the result of a long lasting team work, that would not have ever seen the light without the contribution of many different people. And making an ordered list of people to be thanked is tough, you are so many and I thank you all! I tried to keep some order in this list, but then it got out of my hands and got unorganized, a bit like my office desk: I apologize if I forgot someone.

I would start thanking the coach of this team work, my supervisor Rainer Timm, for always supporting and motivating me during my studies and always finding time for me: I am quite sure that this is one of the most appreciable supervisor's virtues from a PhD student perspective. It was really a pleasure working with you, and I learnt an amazing quantity of stuff just from our discussion, from your feedbacks or just when sitting at a beam line doing experiments.

I am also very indebted towards my co-supervisor, Anders Mikkelsen: I am very grateful for introducing me to many different fields of synchrotron and STM science and to involve me in many different and exciting projects. It was great to find a co-supervisor with the door always open for me and with a such positive attitude, that always boosted my morale even in the toughest experiments.

Thank you both, I have been very lucky in having you as supervisors!

A special acknowledgement goes to Jesper Wallentin: working with you on the nano-XRF project has been an awesome opportunity, with so much science and super-exciting beam times. I have learnt so many different things that I consider the nano-XRF project as a PhD inside the PhD. I would like to also thank Magnus Börgström, Gaute Otnes, Xulu Zeng and Vilgailė Dagytė from FTF for the excellent collaboration in this project.

I am very indebted to Olivier Balmes for introducing and guiding me into a new dimension of XRD: it was real fun to work at the nano-pyramids imaging project. Special thanks goes to Zhe Ren, one of the kindest and most XRD-expert colleagues I've ever met. I would also like to thank Thao Zhou, one of the most science-enthusiast colleagues I have ever worked together, with wonderful ideas and endless energy. I am also very thankful to Zhaoxia Bi and Olof Hultin for growing the samples and for the fruitful discussions.

I am also very grateful to Lars Erik Wernersson, for all the discussions about our nano-electronics projects together. I would like to acknowledge also Aein S. Babadi, for the precious collaboration on the project about thermal oxidation of InAs.

Doing experimental science is though, disappointing sometimes: it would be even tougher if during beam times (and STM-times) I wouldn't have had wonderful

colleagues like Sofie Yngman, Lert Chayanun, Sarah McKibbin, Zhihua Yong, Yen-Po Liu, Yi Liu, Susanna Hammarberg and Dimitry Dzhigaev.

Beam times would not be possible if there were not expert and helpful beam line scientists like Damien Salomon and Matteo Amati: thank you for all your support!

I would like to thank Heiner Linke and Gerda Rentschel for organizing the PhD4Energy project. One of the nicest things about PhD4Energy was doing the internship: I would like to thank Dina Carbone, Virginie Chamard and Marc Allain for this wonderful opportunity!

I would like to thank the two administrative pillars of our division that makes our life much (much) easier: Anne Petterson-Jungbeck and Patrik Wirgin. Patrik, be aware I will ask you one more time whether I have to put the tick on "diary allowance" or not.

A great (great) thank you goes to Lisa Rullik, for being an excellent friend, colleague and proof-reader and for always supporting me. Talking about great proof readers, I am very indebted to Hanna Dierks: thank you for your support during the thesis writing! A special thanks goes to Bart Oostenrijk, for sharing with me not only super-precious help in programming, but also a sharp sense of humor and the passion for bicycles. Talking about passions, I would like to thank Lukas Wittenbecher (and Veronika!) for all the support and for our board game nights! I am very grateful to Stefano Albertin and Giulio D'Acunto, who with all the laughs, talks, and dinners made me always feel at home (and we got an espresso machine). Since Payam Shayesteh is an expert of the motto "daje Roma", I would like to thank him here among the Italians, for all the talks, laugh and support during my thesis writing. When it comes to languages: tusen tack till Susanna och Sofie för att hjälpa mig varje dag att förbättra min Svenska!

I would like to thank Erik Malm for being an excellent office mate and Jovana Colvin for sharing with me the joys and pains of lab supervision. I would like to thank Sandra Benter, Yi Liu, Tamires Gallo, Foqia Rehman, Virginia Boix, Veronica Linpé, Claudiu Bulbucan (ciao, ragazzo!), Edvin Lundgren, Estephania Lira and all my colleagues of SLJUS for all the scientific and non-scientific discussions and for making SLJUS a very nice and enjoyable working place.

I gratefully remember also my previous co-workers at SLJUS: I would like to start thanking Niclas Johansson, a very good friend and probably the most Igor expert person I have (and will ever) met. I would like to thank Martin Hjort, Olof Persson and Johan Knutsson for initiating me to the cult of STM and STS, Milena Moreira for sharing beam times and the passion for art, Elin Grånäs and Olesia Snezhkova for being excellent office mates and for our coffee breaks, and Andreas Schaefer for all your energy, good tips and friendship. I would like to thank Mattias Åstrand, for being a great STM colleague and a dear friend sharing my passion for videogames! Having beam times at Elettra was for me more fun than any other beam time, also

because of the nice discussions and lunches with Luca Rebuffi: thank you for all your support during these years.

I would especially like to thank two colleagues that I have known from day -45, already at the interviews: Artis Svilans and Vilgailė Dagytė (it has been great working with you!).

I would like to thank all the friends here in Lund, especially Annita, David, Christel, Marie-Laure, Tasos, Lisa Z., Hadi, Orwah, and Alireza.

A special thanks goes to my dear friends Stefano R., Francesca, Francesco and Mathias: all far from me in distance, but always close, who gave me a huge support. And how could I forget my dear friends Rocco and Stefano Z.?

Vorrei infine dedicare un grazie speciale alla mia famiglia: ai miei genitori ed alla mia sorella, ai miei nonni, ai miei zii ed alle mie cugine, ad Antonio, Giuliana, Paola ed a tutta la Lubiana crew, per avermi sempre sostenuto in tutti questi anni. Ed ovviamente, grazie Roberta: tutto questo (e non solo!) non sarebbe semplicemente stato possibile senza di te.

1. Introduction

1.1. Motivation

In the last decades it has become more and more challenging to reduce the consumption of resources and at the same time satisfy an unstoppable growth of goods demand in the global market. In addition to this, global warming[1] and pollution issues impose sustainable long term policies for energy harvesting and consumption, in which renewable energy sources will play the lion part in the future. In order to tackle these challenges, a technological revolution is needed, especially into the semiconductor industry. The ambitious aim is to research and produce efficient electronic and optoelectronic components for mass production, like transistors, solar cells and lighting devices. More specifically, the goal is to look for new materials and innovative design architectures: an interesting approach is to shape these new materials into nanostructures, for compact and efficient devices.

Regarding the research on new semiconductor materials, nowadays almost the totality of electronics is based on silicon (Si), which is relatively inexpensive and easy to manufacture and functionalize in devices. However, Si does not have the best functional properties *per se*[2], and its indirect band gap in the infrared spectral range puts fundamental limits to performance in opto-electronic applications, like e.g. solar cells. Moreover, Si based devices are approaching their scalability limits and new substitutes of Si are needed for small and more efficient devices.

For these reasons, one of the most effective approaches to develop new efficient and powerful devices is to find novel material candidates to replace Si: considering the huge market share of electronics, even marginal improvements in performance gained from substituting Si can have a big impact in energy consumption (and also in energy harvesting, in the case of photovoltaic cells).

One promising candidate for these applications is constituted by the class of III-V semiconductors. They are compound materials which combine one or more elements of group III (e.g. Al, Ga, and In) with elements of group V (e.g. N, P, As, and Sb) of the periodic table. In general, these materials are characterized by a high charge carrier mobility[3-4] and a direct band gap, that can be tuned by alloying different III and V elements. These factors determined the interest in performing research on these materials, which are actually already used successfully in industry and can be found in everyday devices.

The possibility of implementing such III-V materials in nanostructures, such as the rod-shaped nanowires (NWs) that are discussed in this thesis, has furthermore expanded the possible device designs, opening new intriguing perspectives on scalability, functionality, and efficiency.

III-V NWs can be functionalized by designing heterostructures, i.e. combining different III-V materials in the same structure. Another milestone in NW functionalization is given by the possibility of controlling the doping, i.e. the incorporation of intentional impurities in the NW, which strongly affects the charge transport characteristics. Moreover, III-V NWs are highly viable for integration with the established Si technology[5]: the strain due to the different lattice constant of the Si substrate and the NW can be easily relaxed due to the small footprint of the NW. This compatibility of III-V NWs with inexpensive Si substrate makes them very interesting candidates for industrial scale production.

However, a fundamental understanding of III-V semiconductor nanostructures is still needed. The complete knowledge of the underlying physics and chemistry can be usefully capitalized on novel applications which can have a strong impact in the urgent demands of society stated above.

In this thesis a step forward in this direction is presented: different characteristics relevant for device performance have been identified and selected, and the characterization of these properties has been addressed with a complementary variety of techniques. Several open problems are explored in this thesis: first, one of the biggest hindrances to the development of III-V technology is the poor surface quality, which can be improved with dedicated processing approaches, whose mechanisms and physical and chemical electronic effects on the surface are yet not completely understood. The open problem of surface quality and its intimate correlation with technologically relevant processing is of high interest, since it affects both flat surfaces and nanostructures. Regarding NWs, a new degree of control and understanding of doping and structural quality is needed. High precision in concentration and spatial distribution of dopants is needed to obtain the desired functionality, whereas structural defects, such as lattice strain and tilt can compromise opto-electronic features. While a more detailed discussion on the relevance of these aspects will be provided afterwards, it is important to underline here that a more complete control of these aspects of NWs can pave the way to a wider spread in their applications.

X-rays are an excellent probe to characterize the structure and chemistry of these systems, and they have been used in this thesis as the main investigation tool. A wide plethora of advanced characterization techniques involving different kinds of matter-radiation interactions is available: in this work, I will focus on X-ray photoelectron spectroscopy (XPS) and its variants, X-ray fluorescence (XRF) microscopy, and X-ray diffraction (XRD) imaging. Moreover, the work presented here relies on X-rays produced by synchrotron sources, that offer unprecedented

possibilities in terms of high brilliance, coherence, and energy tunability, compared to traditional X-ray sources. Dedicated cutting edge X-ray optics also allows to perform microscopy studies with the aforementioned techniques, which is fundamental in case of nanostructures. Due to these advantages, synchrotron based techniques are an excellent resource to integrate and complete the information on the nanostructures obtained with standard laboratory techniques, such as scanning probe and scanning electron microscopy and optical and electrical measurements.

The viable information from synchrotron X-ray based tools has been extended, whenever possible, by performing *in situ* and *operando* studies. This approach brings fundamental studies a step closer to real applications: *in situ* studies allow to study a sample of interest, for instance a surface deposition treatment, in environmental conditions close to industrial standards. *Operando* studies instead are relevant when studying devices, since they can unveil physical phenomena during operation.

In most of the cases of study treated in this dissertation, the characterization approaches are not routinely used in academia and/or industry, but are new. This is actually one of the main motivation for this work, i.e. the development of new characterization approaches adequate for successfully investigating novel material system for future efficient devices.

1.2. Outline of the thesis

This thesis is structured in two main blocks: a first introductory part is meant to guide the reader to the second part, which is a collection of scientific articles and manuscripts. The goal of the introductory part is to give a general background on the topics covered in the whole thesis, contextualizing the papers of the second part in a congruent scientific framework and making the results accessible to a wider audience. The numbering order of the papers is intended to be coherent with the structure of the introductory part. Whenever needed, the reader is readdressed to specialized literature for the details.

In **Chapter 2**, a general background on the III-V semiconductor systems of interest is provided. The aim is to provide general information about III-V systems, their structure and surface properties, and their implementation in fundamental devices. The chapter underlines the open scientific questions about the control of processing aspects which can undermine the real device performances.

Chapter 3 introduces a powerful and flexible approach to tackle these problematics, that is X-ray based characterization. This chapter provides a framework for the following ones, pointing out the X-ray interactions that can be experimentally

exploited, explaining also the benefits of synchrotron X-rays compared to lab sources.

From Chapter 4 to 7, the experimental techniques that I used during my PhD project are discussed, with the aim of answering the open issues stated in the previous chapters. For this reason, the main experimental results are shown right after the respective technique. The detailed results, supported also by other characterization tools, are fully described in the papers, whereas this dissertation aims to pinpoint the practical relevance of the results in a wider context and to give a common framework for the papers.

Chapter 4 deals with III-V surface characterization with X-ray photoemission spectroscopy (XPS) and its variants. The theoretical and experimental grounds are discussed, introducing the results of Papers I and II: high resolution XPS was used for studying the effects of doping on NW surfaces (Paper I) and to monitor a surface processing on a III-V substrate (Paper II). A variant of XPS, the ambient pressure XPS, is then discussed since it has been used in Paper III. The highlights of this publication regarding an *in situ* investigation of a thin layer deposition on InAs are presented. Scanning photoemission microscopy is also treated, since it has been used in Paper IV to study the surface potential of NWs devices during operation.

Chapter 5 shows a novel characterization approach based on X-ray fluorescence microscopy for doping quantification in III-V nanowires; the chapter introduces paper V.

In **Chapter 6** X-ray diffraction imaging, a powerful technique to study strain in nanostructured materials is introduced. The case of interest (discussed in detail in Paper VI and VII) regards NW (or better, "nano-pyramids") arrays relevant for solid state lighting, in which the relation between structural inhomogeneity and manufacturing parameters is studied.

Chapter 7 briefly introduces complementary laboratory techniques which were needed for a well-rounded characterization of the samples, like scanning tunneling microscopy (STM) and low energy electron diffraction (LEED) used in Paper II.

In **Chapter 8** concluding remarks are stated, stressing the relevance of the results in answering the questions motivating this project. Open questions and challenges are also stated and future possible developments are suggested.

2. III-V nanostructures for new devices

2.1. Properties of III-V semiconductors

This thesis focuses on III-V semiconductors with different chemical composition and shape. Here, an overview on features that are common to the whole III-V family are presented to give the reader a proper framework for the specific material systems and cases of study described afterwards in the thesis.

The chemical bond in III-V semiconductors is sp^3, which is mainly covalent, with a certain amount of ionic character[6] due to the difference in electronegativity between the group III and V constituents. Most of the III-V materials (e.g. InP, InAs, GaAs, etc…) crystallize in the zinc blende (Zb) structure (Figure 2.1a, left), which can be regarded as the resultant of two face centered cubic sublattices of the single components, translated by a [¼ ¼ ¼] vector in atomic units. Depending on the ionic character of the bonds, some III-V materials (e.g. GaN) can also crystallize in the wurtzite (Wz) form (Figure 2.1b, left): similarly, Wz can be seen as two interpenetrated hexagonal lattices. Wz and Zb are actually morphologically similar since they differ only in the stacking sequence along the [111] direction (corresponding to the [0001] direction in the hexagonal lattice coordinates). This can be better visualized by considering bilayers of atomic planes, e.g. pairs of group III and group V planes: the stacking sequence is ABCABC… for Zb (Figure 2.1a, right), whereas it is ABAB… for Wz (Figure 2.1b, right).

In addition to binary components, optoelectronic properties like the band gap of III-V semiconductors can further be modulated by alloying two or more different types of group III and/or V components, giving rise to ternary or quaternary alloys. In this thesis, two ternary alloys have been explored: $In_xGa_{1-x}N$ nano-platelets and $Ga_xIn_{1-x}P$ nanowires, which will be described more in detail in the dedicated sections.

Conductivity of III-V semiconductors can be tailored by doping[7], i.e. by the addition of atomic impurities, which increases the number of free charge carriers. Dopants typically belonging to group II of the periodic table (e.g. Zn) act as *acceptors*, i.e. at temperatures (T) higher than 0 K, they get ionized by accepting electrons from the semiconductor valence band, increasing the number of holes there, which are

the majority charge carriers. The chemical potential of the *p* doped material is different from the undoped (or *intrinsic*) case, and the Fermi level $E_{f,p}$ is shifted towards the valence band. Dopants from group VI act instead as *donors*, i.e. the additional valence electrons can be excited to the conduction band (at $T>0$ K), increasing the number of electrons there, which become the majority charge carriers. In this case, the Fermi level $E_{f,n}$ of the *n* doped semiconductor is shifted towards the conduction band. When combining a sequence of *p* and *n* doped regions, the Fermi levels $E_{f,p}$ and $E_{f,n}$ are aligned at thermal equilibrium, causing band bending of the *p* and *n* sides, which act as a barrier for the further diffusion of free charge carriers to the other side. This barrier height, and therefore the resistivity of the *pn* junction can be controlled with a proper bias, and this concept is at the basis of most optoelectronic and electronic devices, as explained afterwards. A detailed discussion about the properties of *pn* junctions can be found in references[7-8].

Doping is crucial in controlling the functionality of semiconductor devices. This is even more important for nanostructured devices, where even small amounts of dopants can dominate their behavior. Controlled doping incorporation in nanostructures is therefore an active field of research, which requires adequate doping characterization tools[9]: parts of this thesis (**Papers I, IV and V**) are dedicated to investigate open issues related to doping in nanostructures.

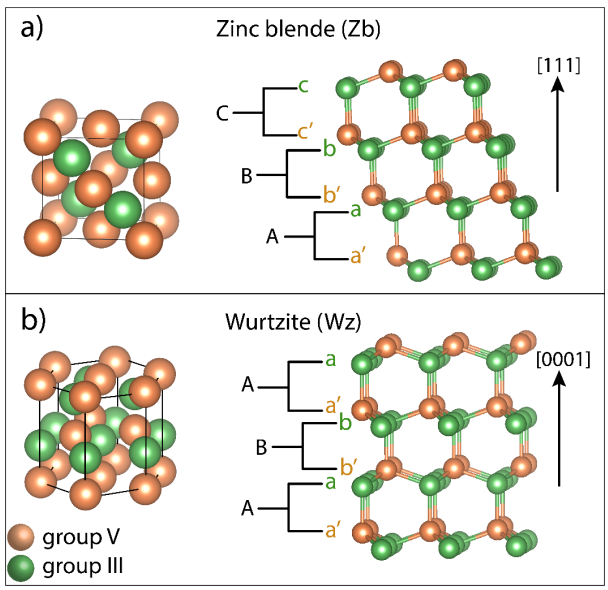

Figure 2.1: III-V bulk lattices: zinc blende structure (a) is composed by two interpenetrating face centered cubic structures (left), and can be seen as stacking sequence of ABCABC III-V bilayers (*a* and *b* represent layers of III and V atoms). Wurtzite (b) is composed of two hexagonal closed pack structures (left) and can be seen as a sequence of ABAB bilayers. [Drawn with VESTA software[10]]

2.1.1 Semiconductor surfaces

As in most material systems, surfaces play a major role also in semiconductor devices, since this is the region interfacing with the extern.

Surfaces constitute necessarily a disruption of the crystal symmetry, and the atoms at the boundary have under-coordinated (or dangling) bonds. This means that there are additionally available states localized at the surface, pointed out with the generic term *surface states*. Therefore, the chemical potential of even a perfect defect-free surface is in general different from the one of the bulk (Figure 2.2a). At thermal equilibrium, the chemical potential of bulk and surface is equalized[11-12], implying the formation of a space charge region beneath the surface (Figure 2.2b). The space charge region can for example be caused by the filling of the unsaturated dangling bonds at the surface with free electrons. This charge accumulation at the surface is balanced by the ionized donors from the inner region. The formation of this electrostatic potential consequently causes a band bending towards the surface, and its entity can be modelled with Poisson's equation.

Similar phenomena at the surface can also be described for more complicated (but more useful, in practice) interfaces, i.e. semiconductor-metal and semiconductor-insulator. In case of the semiconductor-metal interface, a spatial charge is formed at equilibrium to level up the respective Fermi levels. A band bending results from the charge exchange between the metal and the semiconductor. The entity and sign of this band bending (known as Schottky barrier) depends mainly on the work function of the metal and on electron affinity and doping of the semiconductor. It is noteworthy that this concept describes the ideal Schottky barrier, which depends only on intrinsic properties of the two separated systems.

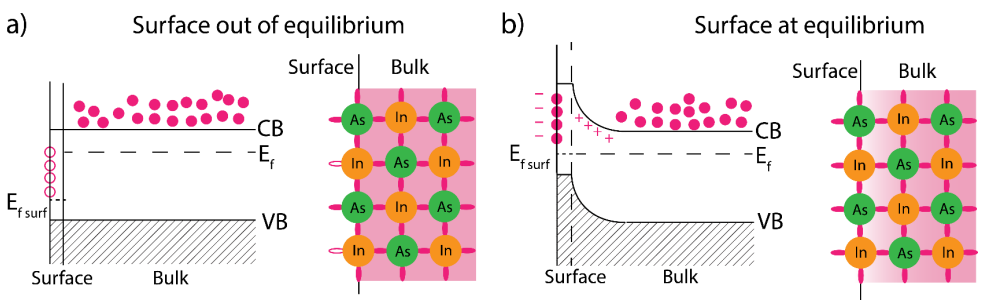

Figure 2.2 a) On the left: the band energy diagram with the surface not at equilibrium, in the case of a *n* doped semiconductor. The Fermi level of the surface ($E_{f,surf}$) is not aligned with the Fermi level of the bulk (E_f). CB and VB are respectively the conduction and valence band edges. On the right: representation of atomic bonding: atomic filled bonds are represented as traits filled with dark pink, unfilled bonds as void traits. The pink area represents the electrons in CB. b) Surface at equilibrium: band diagram on the left, with $E_{f,surf} = E_f$ and formation of the space charge layer ("+" signs). In the bond sketch on the right, the faded pink area represents the space charge region, depleted of electrons.

In reality, one has to consider also the effects of surface states at the interfaces, which can modify the barrier properties.

The interface towards an insulator or oxide is, ideally, similar to the semiconductor-vacuum case, since no charge exchange can take place at the interface. However, additional polarization charges and impurities (e.g. interface traps or oxide charges) will influence the number of surface states. The impact of the surface states on device performance will be discussed more in detail in Section 2.4.

An important factor in determining the amount and type of surface states is actually the atomic plane cutting the crystal and defining the surface. Technologically relevant surface orientations[11] are the (100), (111) and (110) facets, defined by their Miller indices (*hkl*). Actually, the atomic pattern defined by these facets (except the (110)) is often not preserved, since these conformations leave many dangling bonds, which are energetically not stable. The surface usually undergoes a reconstruction, which means that the surface atoms self-reassemble into a structure of lower energy. These patterns, which are important in determining the electronic states of the surface can be determined by low energy electron diffraction and scanning tunneling microscopy, which will be discussed in Chapter 7.

2.2. From bulk to nanowires

Nanostructured materials have one or more dimensions in the nanometer range and their thermodynamics and functional properties[13] may differ significantly from their bulk counterpart. Nanostructures can be classified depending on their characteristic dimensions, which determine the density of states and charge transport properties[14]; one can identify zero-dimensional nanostructures, such as quantum dots, one-dimensional, such as nanowires (NWs), and two-dimensional nanostructures, such as graphene and other thin films[15]. In this dissertation I focus on planar substrates, i.e. three-dimensional samples with a flat surface, and on NWs. Flat substrates are in fact an useful model systems and a simple case of study that can be extended to NWs[16] in a second moment.

III-V NWs are needle shaped structures of III-V semiconductors with a high aspect ratio, in which the radius ranges typically between 10 and 200 nm and the length can extend up to several μm[17] (Figure 2.3).

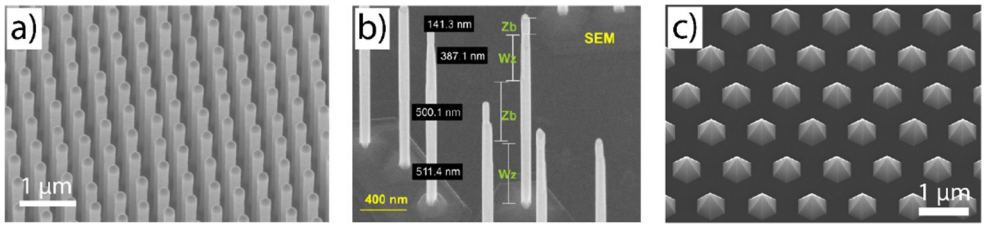

Figure 2.3: III-V nanowires examples. a) InP NW array for solar cell applications [adapted from Paper V]. b) InAs NWs for electronics; Wz and Zb segments are put in evidence [courtesy of Dr. Sebastian Lehmann]. c) $In_xGa_{1-x}N$ nano-pyramids for LED applications [courtesy of Dr. Zhaoxia Bi].

They are promising candidates for electronic and opto-electronic applications due to their high charge carrier mobility, the direct band gap, and the possibility of incorporating dopants *in situ* with high control. The remarkable freedom in designing defect-free heterostructures[18-19] in NWs is also one of the major breakthroughs for their implementation in electronic devices. For example, axial heterostructures in III-V NWs are viable due the low radial dimensions. They in fact allow to accommodate the strain at the interface caused by the different lattice parameters and to compensate for different thermal expansion coefficients, assuring an epitaxial continuity of the two matching phases.

III-V nanowires can also be interfaced directly with Si substrates[5, 20]: the (hetero)epitaxial growth of III-V on Si is particularly attractive from a practical point of view, since the process can be potentially integrated in the existing Si technology platform. The feasibility of the concept has already been demonstrated and implemented in real opto-electronic devices[21].

When it comes to devices, the high aspect ratio of NWs can result very useful in wave guiding effects for solar cells applications[22] or for improved electrostatic control for electronics[23], as it will be discussed afterwards. Interestingly, the limited radial dimensions in NWs allow also to obtain crystallographic variants that are not stable in the bulk form[24]: this feature can be interesting for quantum devices, in which a Wz quantum well can be for instance inserted between two Zb segments[17]. The high surface to bulk ratio of nanowires has however also the consequence that the electronic behavior can be dominated by the surface, affecting the whole nanostructure. An example is the Fermi level pinning effect, that can be summarized as the inability to change the semiconductor Fermi level due to a high number of surface states; this effect can extend to the whole NW diameter, dominating its behavior. For this reason, an effective passivation[I] of electronically active defects is even more important for nanostructures.

[I] Passivation will be discussed more in detail in Section 2.4. For now, it can be defined as processing reducing the active surface defect density.

2.2.1. Nanowire growth

Nanowire growth is a broad research field and a wide variety of NWs with different composition, shape and properties can be produced: the goal of this section is therefore not to give a complete overview on the topic, but only to contextualize the samples presented in the papers.

Nowadays, a plethora of technologies is available for growing needled shaped structures such as NWs, which can be categorized in two big families: top-down and bottom-up approaches. In the top-down paradigm, a bulk material is consumed selectively giving rise to a NW pattern, whereas the bottom-up approach consists in growing NW structures by assembling them from basic building blocks[25].

All the NWs treated in this thesis are produced with a bottom-up approach, which enables precise control on their geometry and structure, with efficient material consumption. The bottom-up approach can be implemented with different crystal growth techniques, and two popular options are the molecular beam epitaxy (MBE) and the metal organic vapor phase epitaxy (MOVPE). Both are epitaxial techniques, meaning that the crystal order is not disrupted between the substrate and the NW, and they differ mainly for the supply source of the reactants.

Most[II] of the NWs used in this thesis were grown using MOVPE, where one or more of the reactants are supplied in vapor phase in the form of metalorganic compounds, which are metals stabilized by organic groups (typically aliphatic compounds, like methyl $–CH_3$ or ethyl $–C_2H_5$).

In the MOVPE process, the reactants are supplied in gas phase and then deposited in solid phase, and the growth can be mediated by an intermediate liquid phase, as it will be discussed in the next section. A necessary - but not sufficient - condition to deposit the reactant in solid phase is that the transition from gas to solid is thermodynamically favored, i.e. there is a decrease of the Gibbs free energy which can favor the nucleation of the stable solid phase. In order to grow NW structures, the nucleation and growth need to be done with proper size selection and control, that can be accomplished in different ways. A way to achieve this goal is the *particle assisted growth*, where a catalytic particle provides a preferential reaction interface for the epitaxial growth, determining also the radial dimension of the NWs. A different approach consists in the particle free growth, where the catalyst is absent: in this case, the directionality and the size selectivity are typically guaranteed by a mask deposited on a substrate and the process is therefore called *selective area epitaxy*[26-27]. It is worth noting that a neat taxonomy does not exist, since many processing variants have been developed. As a matter of fact, the NWs of **Paper V** have been produced using both a mask and Au particles placed in the openings of

[II] The NWs of paper I were deposited with a new approach called *aerotaxy*, which does not require a growth substrate and is treated afterwards.

the former[28]: this strategy is useful to control the consistency of the NW pattern for large substrate areas.

Particle assisted growth

The particle assisted growth is widely used in the community[29] and its mechanism is useful not only to describe the NWs used in **Papers II, IV and V**, but also some general features of NW growth, without loss of generality. The particle (also known by "seed") melts in the process, which is characterized by the compresence of vapor-liquid-solid (VLS) phases, and it is therefore described and known as VLS growth[30].

The process can be summarized as follows:

i) A catalytic particle (typically Au) is deposited on the growth substrate (Figure 2.4a). The choice of the growth substrate is important, since the growth is epitaxial and it influences the morphology of the NW. Usually, the atomic dense facet (111) is chosen.

ii) Before the actual growth is started, the substrate is heated and the group V precursor (e.g. arsine AsH_3 or phosphine PH_3) is flown into the reactor (Figure 2.4b). This step is effective in removing native oxides from the surface[31], which could undermine the epitaxial continuity and also allows to melt the Au particle. The Au particle melting is important from a thermodynamic point of view (the Gibbs free energies in play depend on the phase state) and also because the meniscus of the melted particle is useful in preventing its movement on the surface[28].

iii) The growth is carried out by supplying both the group III and group V precursors in conditions allowing a complete pyrolysis (i.e. break of the ligands from the metal atom) of the group III reactants (Figure 2.4c). The liquid metallic particle gets supersaturated of the group III atoms, which precipitate in solid phase at the interface with the substrate. The group V precursor usually reacts directly from the gas phase. During this step, dopants can be also introduced *in situ*, i.e. together with other reactants, and get incorporated similarly to the NW components (Figure 2.4d). More in general, axial or radial heterostructures can be grown at this stage, by modulating the type of precursor, the growth temperature, and their relative molar fraction and flux[32].

iv) The growth can be stopped by switching off the flux of reactants in gas phase and by decreasing the substrate temperature. It is worth noting that, even if the reactants are not present in gas phase any more, they can still be present in the liquid Au particle. This is particularly relevant for the group III metal, e.g. In, which has a high solubility in Au, and can therefore precipitate further. This effect of an In-enriched tip of the NW can be observed in Chapter 5 and in **Paper V**.

Summarizing, the interface between the molten Au particle and the solid semiconductor provides an energetically favored site for the heterogeneous nucleation of the new solid surface through the supersaturation of the group III precursor material in the particle.

It has to be kept in mind that also kinetics plays a central role and therefore the growth is eventually controlled by processes whose rate is limited by temperature. The two main limiting factors determined by temperature are the pyrolysis of the precursors and their diffusion to the nucleation interface. The diffusion can take different paths: the precursors can impinge directly to the seed particle and diffuse through it (Figure 2.4e, path 1) or can adsorb to the substrate (path 2) or to the NW (path 3) surface and diffuse along it. The growth can therefore be limited by species diffusion, which is typically slower on the surface rather than in the liquid particle.

This effect can be readily seen in **Paper V** for the ternary NWs, like $In_xGa_{1-x}P$. It is in fact known[33-34] that even if the ratio between the two group III components, Ga and In, is kept constant during growth, one can observe a gradient in the In/Ga ratio along the NW, which can be due to different diffusion lengths of the group III precursors, different pyrolysis efficiency or different incorporation paths[33].

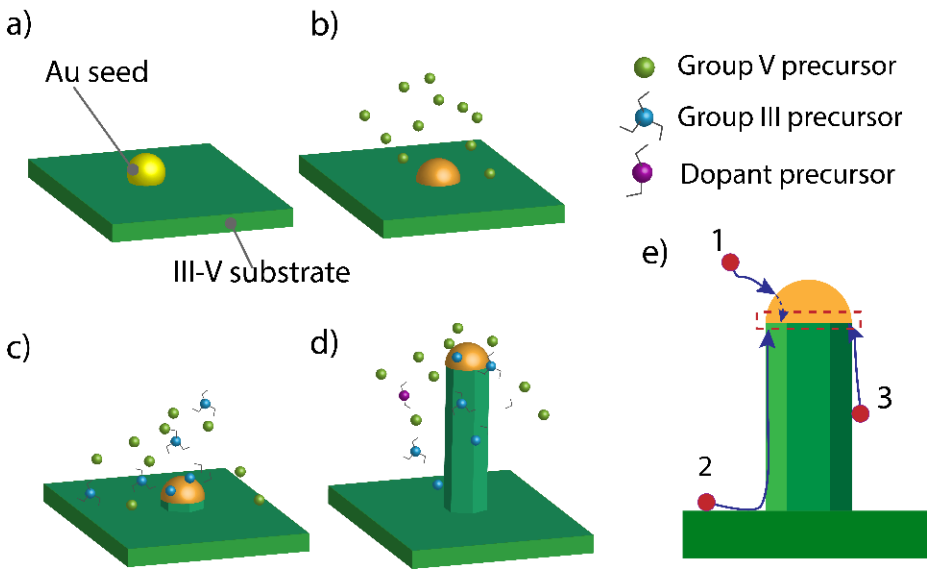

Figure 2.4: a)-d): Particle assisted growth steps of a NW. a) Au seed is deposited on the substrate; b) Temperature is increased and the group V precursor is flowed in the reactor. c) Introduction of group III and V precursors and growth of the NW. The sticks around the precursors symbolize the carbon chains of the ligands d) Introduction of dopants. e) Diffusion path of the metalorganic precursors in the VLS model: 1. Diffusion through the gold particle. 2. Surface diffusion from the substrate 3. Surface diffusion from the NW.

Selected area epitaxy (SAE)

The particle assisted growth has the disadvantage of embedding a metallic particle at the top of the NW, which can be undesirable for some applications[35-36]. An interesting alternative is a particle free growth technique, which is called selected area epitaxy (SAE). Also in this case, the idea is to force an anisotropic growth reaction in one crystallographic direction, suppressing lateral growth. This goal is typically pursued by the apposition of an inert mask (e.g. Si_3N_4) on the growth substrate. Consequently, when the reactants are supplied in gas phase, the growth can only take place on the mask openings. In the case of study of **Papers VI and VII**, the liquid interface is missing and the reactants are incorporated directly from the gas phase or, mostly, via surface diffusion from the mask. Two important parameters are diameter of mask opening and pitch, which is the distance between the openings. The opening is a parameter comparable to the seed diameter, and the pitch is an important parameter (also in case of particle assisted growth), since it is inversely proportional to the collection area, i.e. the mask portion from which each NW is supplied with the precursors via their surface diffusion. Consequently, it controls the distribution of precursors to the NWs and, in case of precursors with different diffusion lengths, the homogeneity of the NWs.

Regarding the relevance of SAE in the present work, it has been used for a novel approach to grow GaN-$In_xGa_{1-x}N$ platelets (or "nano-pyramids")[37], as it will be specified in Chapter 6 and **Papers VI and VII**.

Aerotaxy growth

Aerotaxy growth is a revolutionary paradigm for fabricating NWs[38] and more in general size-selected nanocrystals[39-40]. Aerotaxy takes place in a continuous gas phase, which means that it is not subject to the batch production restrictions imposed by epitaxy growth methods. Remarkably, the growth rate for NWs produced via aerotaxy is about 1μm/s, that is 20-10^3 times more than the traditional epitaxy routes[38]. These facts imply the important advantage of a mass production which is additionally very cost competitive, since the expensive III-V epitaxial substrate is not anymore required.

Aerotaxy has been demonstrated to be a versatile method for NW production with different compositions and doping[41-43]; however, here the discussion of the aerotaxy mechanism is confined to the Zn doped GaAs NWs studied in **Paper I**.

An aerosol of Au nanoparticles, which are needed as growth catalyst, is generated by evaporation followed by controlled condensation in gas phase. This dispersion of Au nanoparticles in gas phase has in general a wide size distribution (a typical value[44] being 40-80 nm). A size selection is therefore usually operated by charging the Au agglomerate and selecting them with a differential mobility analyzer[45]. The reason why a monodispersed distribution is needed is because the size of the Au

particles determines the diameter and shape of the NWs, consequently affecting also the homogeneity of the physical properties of the whole NW ensemble.

The Au particles suspended in the carrier gas are flowed into the reactor, where the precursors are supplied in gas phase: Ga metalorganic precursor for the group III and arsine (AsH_3) for the group V. Tailoring the III/V molar ratio and the temperature, a directional growth starts from the Au particle, along the [111] direction. In this step diethyl-Zn, the *p* type dopant precursor, is supplied. Finally, the NWs exit the reactor and are collected on a substrate (usually Si).

Interestingly, GaAs aerotaxy NWs can accept higher *p* type doping levels compared to the epitaxial counterpart[44], due to the absence of out-diffusion of Zn to the epitaxial growth substrate.

However, the dopant incorporation mechanism in aerotaxy NWs is still not understood, and it is known[46] that doping can strongly influence the morphology and quality of NWs. These aspects are studied in **Paper I** by using scanning probe microscopy and synchrotron based XPS. Surprisingly, the latter technique showed that high *p* type doping can actually suppress the oxide naturally present on the surface of the NWs. This fact can have important consequences for the chemical quality of the surface, as discussed afterwards.

2.3. Electronic and optoelectronic devices based on III-V semiconductors

In this section those III-V electronic and optoelectronic devices relevant for the cases of study of this thesis are introduced. The discussion will therefore be limited to light emitting diodes (LEDs), solar cells and field effect transistors (FETs).

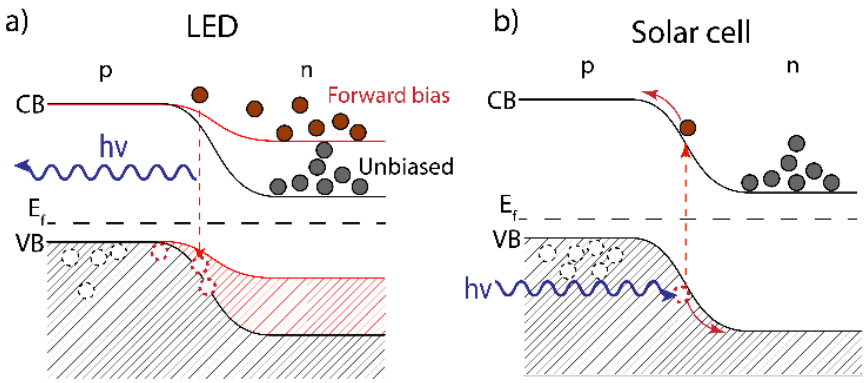

Figure 2.5: a) LED working principle: in the band diagram of the *pn* junction, holes in the *p* doped side are represented as void circles in the valence band (VB). Electrons in the conduction band (CB) of the *n* doped side are represented as filled circles. The application of the forward bias (in red) cause carrier injection and radiative recombination in the junction (red dashed arrow) with emission of a photon of energy hv. b) Solar cell working principle: a photon of energy hv generates an electron-hole pair, which constituents are accelerated in opposite direction due to the built-in electric field.

2.3.1. Light emitting diodes

Light emitting diodes are based on the concept of the *pn* junction (Figure 2.5a): the majority charge current can be modulated by opportunely changing the potential between the two poles of the device. In a *pn* junction there is a strong asymmetry in the current-voltage characteristics: if a forward bias is applied to the junction, this is taken out of equilibrium conditions, the built-in potential is reduced and the diffusion current of the majority charge carriers gets dominant (Figure 2.5). The dependence of the number of injected charge carriers per second I on the applied voltage V can be modelled[7] with $I = I_0 e^{\frac{eV}{kT}}$, where k is the Boltzmann constant, T is the temperature and I_0 is the equilibrium current. The dependence resembles an exponential due to the distribution of the charge carriers in the conduction and valence bands, which follow a Fermi-Dirac distribution. Conversely, when a reverse voltage is applied, the band offset increases, and the diffusion current gets suppressed, leaving only the drift current of the minority charge carriers. Additionally, in LEDs the majority charge carriers can experience radiative recombination, and emit light. This happens in proximity of the junction when a

sufficient forward bias is applied: in this region, there is an excess of charge carriers compared to the equilibrium ($pn \gg n_i^2$, where n_i is the number of intrinsic charge carriers), and radiative recombination of electrons and holes can happen.

A condition *sine qua non* is that the LED material has a direct band gap, i.e. the transition of electrons from the conduction band to the valence band holes is permitted without need of phonons to match the momentum difference of the electron between the initial and the final state. This is one of the two main reasons why III-V semiconductors are so appealing as LEDs, since most of them are characterized by a direct band gap, in contrast to Si. The second reason is the fact that the light color, i.e. the energy released in the radiative recombination, depends on the band gap of the material, which can be tailored easily by alloying different group III and V elements into the compound.

The depiction of the LED as a *pn* junction is a naïve representation of a real device. More complex architectures are actually designed to increase the rate of radiative recombination and reduce losses: the interposition of one or more thin heterostructures (quantum wells) with straddling band alignment (i.e. "type I") between the *p* and *n* regions is beneficial in producing charge carrier confinement, enhancing the probability of electron-hole wave function overlap and therefore radiative recombination. Other layers and processing are typically utilized to reduce the influence of undesired side effects which reduce the efficiency of LEDs.

The intrinsic efficiency of light emission, i.e. the internal quantum efficiency, is in fact hindered by two competing processes. The first one is the trap-induced non-radiative recombination, also known as Schottky-Read-Hall (SRH) mechanism. In the SRH mechanism, electrons in the conduction band lose energy in a non-radiative path: defects such as dislocations[47], surface traps, or compositional inhomogeneities[48] act as non-radiative recombination centers. The other major loss is given by Auger recombination, i.e. the energy balance by an electron-hole recombination is satisfied with the emission of a secondary electron. It is worth noting that SRH is the dominant loss for low charge carrier density, whereas the Auger mechanism is problematic for high current densities.

Nitride NW LEDs

Nitrides, i.e. III-N compounds, are one of the preferred material classes for LED applications, due to the high light output efficiency and to the possibilities in band gap engineering by alloying different group III elements like Ga, In, and Al. For example, GaN emits in the UV spectral range, but when increasing the fraction *x* of In as an alloy element, the whole visible spectrum can be covered (Figure 2.6a). Moreover, nitride LEDs emitting in short wavelengths (e.g. blue) are used in combination with phosphors to produce white light, revolutionizing the energy saving for general lighting. For this reason, in 2014 I. Akasaki, H. Amano and S. Nakamura were awarded with the Nobel prize[49] for developing the blue LED.

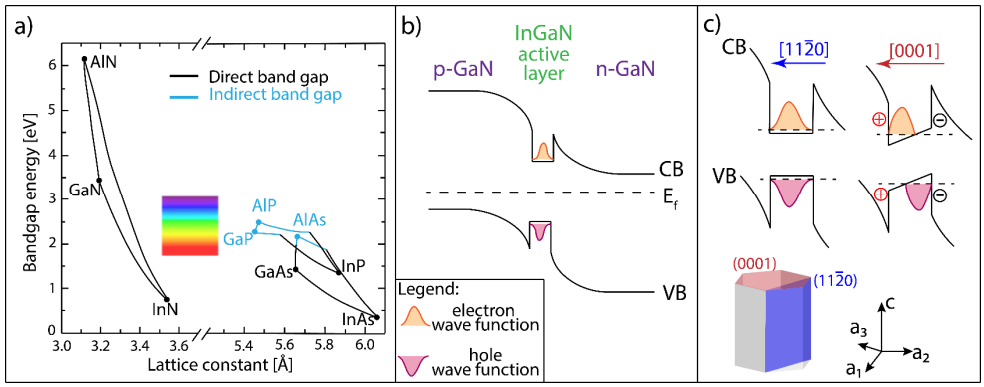

Figure 2.6: a) Band gap energy (at 300 K) for some technologically relevant III-V materials. Nitrides can cover the whole visible spectrum (highlighted with a rainbow bar). [adapted from ref. [52], data from refs. [53-54]] b) Nitride LED with an $In_xGa_{1-x}N$ active layer. c) Quantum confined Stark effect (QCSE): active layers with non polar [11$\bar{2}$0] orientation (left) do not show the QCSE. Active layers with [0001] orientation (right) show the QCSE due to piezoelectricity ("+" and "–" signs), resulting in reduced overlapping of electron and hole wave function.The non polar (11$\bar{2}$0) and the polar (0001) planes are represented in the hexagonal cells at bottom.

Besides their flexibility, in general nitrides show a critical efficiency droop when increasing the In content, when approaching to the green spectral range[48, 50]. This has been attributed mainly to an increase of the SRH mechanism, due to fluctuations in In concentration, and to increased strain and dislocation density[51].

Nitrides typically crystallize in the Wz structure, and the [0001] direction (c-axis) is the preferred one for epitaxial growth of nitrides; however, this crystallographic direction is affected by a strong internal electric field, which leads to polarization effects and piezoelectricity. This fact causes a critical issue in quantum wells, which are inserted in LEDs acting as active layers with high recombination efficiency (Figure 2.6b): the strong internal electric field is responsible for the quantum confined Stark effect[55-56] (QCSE), which consists in a spatial separation between the *n* and *p* type charge carriers in the active layer quantum well (Figure 2.6c). This corresponds to a reduced overlap of their wave functions, which in turn means lower recombination efficiency. This effect can be worsened by the presence of a strong strain field, that due to the piezoelectricity can contribute to the internal electric field.

Shaping nitrides into nanowires can bring several improvements: i) the strain accommodation typical of NWs is beneficial in reducing strain and dislocation density, compared to traditional 2D structures grown on sapphire. ii) for the same reason, a higher content of In can be accepted without generating strong strain fields or increase the dislocation density. iii) The lateral overgrowth of NWs can be enhanced, and non-polar or semi-polar facets like the (11$\bar{2}$2) can be exploited,

reducing the QCSE and at the same time increasing the active area compared to a planar device.

Considering that the NW quality is intimately related to the processing, and that lattice defects hamper LEDs device efficiency, it is important to relate lattice variations such as tilt and strain to the growth parameters. This aspect has been investigated with the help of X-ray diffraction microscopy (Chapter 6) and reported in detail in **Paper VI and Paper VII**, where a clear correlation was found between the NWs - or better nano-pyramids - array quality and the parameters of the mask used for the SAE growth.

2.3.2. Solar cells

One of the most important devices for energy harvesting are solar cells. The goal of solar cells is to absorb light energy, to convert it into electrical energy and transport it into a circuit, from which it can be conveniently stored, for instance in a battery, or utilized. This can be fulfilled by a *pn* junction (actually, the solar cell working principle can be regarded as the opposite of the LED). An incoming photon can be absorbed by the semiconductor (Figure 2.5b): the photon energy is transferred to an electron in the valence band which is promoted to the conduction band, generating an electron hole pair. If the electron hole pair is generated far away from the junction, there is a high probability that the electrons and holes recombine and don't contribute to energy harvesting. Instead, if the photon absorption and the generation of the electron hole pair happen in the depletion region of the *pn* junction, holes and electrons are accelerated in opposite directions by the electric field generated by the space charge region, and they can be collected at the poles of the device.

A necessary condition for the absorption of a photon is that its energy needs to be bigger than the band gap, otherwise the semiconductor is said to be transparent to that photon energy. This is actually one of the major losses in solar light conversion and it is typical of large band gap materials (e.g. GaN). A second fundamental loss is related to thermalization, i.e. a relaxation phenomenon in which the electrons excited into the conduction band loose energy down to the conduction band edge; this loss is typical of narrow band gap materials (e.g. Si or Ge).

Beside other loss mechanisms such as bulk and contact resistance, photon reflection, etc., one loss that is especially important for nanostructures is electron-hole pair recombination at the surface: if not opportunely passivated, surfaces have many available states in which the highly mobile conduction band electron can recombine, not contributing to the photovoltaic current.

III-V NW solar cells

III-V semiconductors such as InP and GaAs offer a fundamental advantage of a more efficient radiative absorption compared to crystalline Si due to the direct band gap. Moreover, the use of ternary compounds, such as $Ga_xIn_{1-x}P$ can be useful to

tailor the band gap for optimal light absorption, similarly to what has been mentioned for LEDs.

A nanowire architecture can lead to several additional advantages in a solar cell: optics in arrays of NWs can be significantly different from flat substrates and the absorption cross section can be enhanced by promoting and suppressing certain wave propagation modes[27, 57]. Furthermore, NWs offer a wide liberty and dimensional control in designing *ad hoc* heterostructures, in which the *pn* junction can be designed radially or axially. NWs can even be designed to contain more than one *pn* junction, which opens up the possibility of designing NW tandem solar cells[29], i.e. devices with multiple *pn* junctions with different band gaps, a paradigm which was shown to be already very successful for thin films. Moreover, aerotaxy might boost the expansion on market of III-V NW solar cells, since this technique can cut production costs, not requiring the expensive III-V substrates like in traditional MOVPE growth.

That said, even if III-V NW solar cells efficiencies increased abruptly recently[58-59], there is need for a careful control of the surface quality and of the doping. Passivation is even more critical for NW solar cells due to the high surface-to-bulk ratio, whereas the complex interplay of several growth parameters determines the abruptness of doping gradients. In **Paper IV** a novel *operando* procedure using scanning photoemission microscopy was established for assessing the surface quality and functionality of InP NWs used as template for solar cells. The method and the results are discussed in detail in Chapter 4.4. Regarding doping control, a novel *ad hoc* characterization method was presented in **Paper V**, with the aim of providing a new method and valuable data for obtaining precise doping gradients in the future. The details are discussed in Chapter 5. It is finally important to remark that doping and passivation are not necessarily two separated issues, but the former can play a central role also in determining the surface chemistry of NWs: this has been observed in **Paper I**, where high doping levels in GaAs NWs modify the surface morphology and even suppress the formation of the native oxide.

2.3.3. Metal oxide field effect transistors

Modern electronics would be unconceivable without the transistor, a device which is the fundamental building block for all integrated circuits and is widely used in information storage, power electronics, and communication technology. The name is a contraction for transfer resistor[7] and the working principle can be described as a switch: the resistance between two terminals (source and drain) is controlled by a third one, known as the gate (Figure 2.7a). The use of a proper gate voltage to control the current between the source and drain is the main feature of a transistor. The wide variety of transistor architectures differs on the mechanism, the materials and the desired operating conditions with which this source-drain resistance variation is achieved.

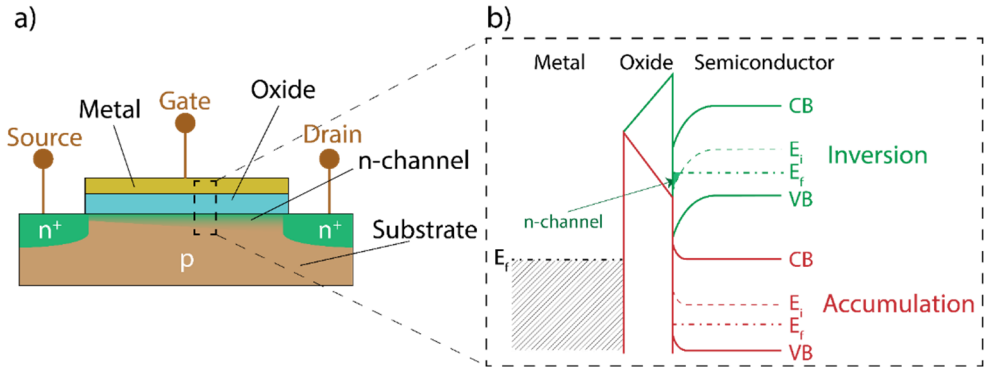

Figure 2.7: a) Sketch of an *n*-type channel MOSFET. b) Band diagram of the metal-oxide-semiconductor stack of the MOSFET. In red the band diagram of the semiconductor in the is shown accumulation regime. In green, the inversion regime, in which in a thin layer adjacent to the oxide the majority charge carrier switches from *p* to *n,* and the resistance between source and drain is lowered (ON state).

In this thesis the particular case of the metal oxide semiconductor field effect transistor (MOSFET) is considered, due to its importance as a basic module for integrated circuits. The working principle of MOSFETs is sketched in Figure 2.7b.

The crucial element of the MOSFET is the metal-oxide-semiconductor junction, which acts as a capacitor. Let's assume that the body of the MOSFET is *p* type and the two end terminals (source and drain) are heavily (to compensate effects of Schottky barriers with contacts) *n* doped. If no bias is applied to the gate, the resistance across source and drain is very high, due to the presence of a double *pn* junction. However, the application of a positive bias to the gate pushes away the holes from the semiconductor-oxide interface (depletion) until the electrons become the dominating type of charge carriers, in other words *inversion* occurs (Figure 2.7b, green curves). A thin region close to the surface (channel) gets *n* type and, if a bias between source and drain is applied, a diffusion current can be run between these two poles and the transistor is in an ON state. If a reverse bias is applied to the junction, the MOS is in *accumulation* regime (Figure 2.7b, red curves), meaning that the majority *p*-type charges are accumulated at the interface and the transistor is kept in an OFF state. ON and OFF states can be exploited in digital logic and computer memories: for this reason, it is important to have fast and efficient switching between these two states at high frequency, with low energy dissipation.

III-V NW MOSFETs

Even if the theoretical grounds of field effect transistors were already proposed in the 30's by Heil and Lilienfeld, they are still nowadays a very active field of research, due to the need of improving performances and reducing their overall dimensions to increase the computational density of devices. The dominant Si electronics is reaching its scalability limits[60], and III-V semiconductors are optimal

candidates for next generation field effect transistors (FETs) due to their high mobility, which improves the transfer characteristics of transistors. III-V materials, like In(Ga)As, have also the advantage to have a smaller band gap compared to Si, which allows lower operation voltage, significantly reducing power consumption.

Performances can be even more enhanced when using a NW architecture. The main advantage of having a NW based FET compared to the traditional planar one is related to the fact that the gate can be wrapped all around a standing NW, giving improved electrostatic control[61-62]. Furthermore, a pattern of vertical NWs helps in increasing the computational density of an integrated circuit[63]. Other advantages to use NWs are the great flexibility in designing heterostructures and tailored doping (e.g. for the so called tunnel FETs) and to grow them on the inexpensive and industrially established Si substrates. On the other hand, the large surface to area ratio of NWs makes surface related defects a critical issue, which can even dominate over the bulk properties of the NW FET channel: the study of the surface and the related processing is therefore of outermost importance. In **Paper II and III** the interface of InAs with typical gate oxides was studied, with the goal to improve FET characteristics.

2.4. III-V surfaces and their influence on device performance

Silicon is still the dominant semiconductor material in electronic device industry, even if it has a weaker performance of charge carrier mobility than many III-V semiconductors. A natural question is therefore why Si has not yet been supplanted by these materials. Besides practical considerations regarding the re-conversion of an entire industrial apparat and the higher cost of III-Vs, one of the main reasons resides in the surface quality of Si, or better, between Si and its oxide, SiO_2, which is far less defective than interfaces between III-V semiconductors and their natural oxides (also called native oxides) [64-65].

Surface states can be intrinsic, which means that they are related to the necessary break of symmetry of the crystal at the surface, but some of them instead are extrinsic and related to defects at the interface, adsorbates[66], or to the local chemical bonding[8, 12]. Surface states are particularly harmful for device performance if they are positioned in the band gap[67-68]. The reason is related to the fact that the Fermi level gets "pinned" at the surface, where its position depends mainly on the nature (acceptor or donor) and quantity of the surface states, rather than the externally applied bias.

A practical consequence for FETs is that the gate does not work as an efficient capacitor: the offset between the Fermi levels of the metal and the semiconductor

gets less than the applied gate voltage, due to the fact that part of it is used to fill/empty the defect states at the surface (also called trap states), or in other terms it is not possible to control the density of charge carriers at the surface[64]. Surface defects can have also a negative influence on solar cells devices, since they can act as preferential recombination sites for electron and holes, therefore limiting the current that can be extracted from the cell.

Surface defects and Fermi level pinning are even more dramatic for nanostructures such as NWs, since the space charge region can extend from the surface in the entire NW diameter, conditioning the whole device performance.

2.4.1. Surface cleaning and passivation

Native oxides on III-V surfaces

The main reason why III-Vs semiconductors are characterized by a high surface defect density is the poor quality of the native oxides. III-V oxides have a complex stoichiometry, which is not simple to determine *a priori*, due to the multiple oxidation states of the group III and V components[69]. Moreover, ternary oxides containing both of the group III and V elements and even non stoichiometric components are possible[70]. Defects are in general due to a poor mismatch with the oxide and unsaturated bonds arising at the interface[71-72], and they consist typically of under-coordinated bonds with oxygen[73], dangling bonds, and dimers (e.g. As-As bonds) of the group V element[67, 74]. Dimers and dangling bonds are also features which depend on the surface reconstruction: surface orientation and reconstruction therefore have a critical influence on surface state density[11, 75], even in oxide free III-V surfaces.

Removal of the native oxides

A natural action to improve the surface quality of III-V semiconductors is to remove the native oxides. Several processes have been tested up to now to accomplish this task[64, 73], which include both wet chemistry treatments (e.g. $(NH_4)_2S$[76], HF, or calchogenides solutions) and dry treatments (e.g. H-plasma or atomic hydrogen[31, 77-78] and ion sputtering[78-80]). The atomic hydrogen treatment is important in this dissertation, since it has been used in **Paper II and IV**, and it is described with major detail hereafter.

Surface cleaning and removal of the native oxides is done in ultra-high vacuum (UHV) conditions by annealing the substrate under a flux of atomic hydrogen. Atomic hydrogen (also known as hydrogen radicals) is produced through thermal cracking of hydrogen molecules by a W filament heated to 1700 °C. The hydrogen radicals are extremely unstable and they are thought to react with the native oxides of the III-V substrate (e.g. InAs) giving volatile products[31]. The main advantage of

assisting the annealing with atomic hydrogen is the reduced heating temperature of the substrate needed for oxide removal (ca. 380 °C for InAs). This fact prevents the incongruent melting of III-V substrates, which occurs for relatively low temperatures (e.g. around 500 °C for InAs[81-82]).

Passivation of III-V surfaces

Nevertheless, oxide removal is usually not sufficient to have good quality interfaces, that need to be preserved in the following processing steps. In order to have efficient transistors with a good modulation of the electrostatic potential at the gate, one needs to make the surface states electrically passive, through a proper passivation process. This is important also for solar cells (e.g. InP solar cells), in order to reduce the number of intrinsic surface states typical of a clean reconstructed surface. Simplifying, passivation means that the surface states in the band gap get moved in energy into the valence or conduction band. Passivation is therefore a surface treatment which goal is to improve the electronic surface quality of the semiconductor interface, and this process is particularly crucial for III-V surfaces[III]. Passivation strategies are therefore not only contemplating native oxide removal, but consider more generally *ad hoc* treatments like nitridation or deposition of interfacial passivation layers[74] to reduce surface defect density.

Improvements in surface quality were also noticed when high permittivity oxides are deposited via a process called atomic layer deposition (ALD)[83]. ALD is particularly important for III-V devices, not only for oxide removal, but mainly because it is one of the most important factors when scaling down the device size.

2.4.2. Atomic layer deposition of high permittivity (high-κ) oxides

High permittivity (high-κ) oxides

Increasing the computational power of devices is a persistent concern for semiconductor industry, as summarized by the well-known Moore's law[84]. Compact devices can be obtained with two approaches: new device architectures[61] and device scaling, which is the approach more relevant for this thesis. Downscaling a MOSFET channel is challenging due to detrimental effects known as short-channel effects[7] and to lower control of the gate stack. In fact, the electrostatic control needs to be kept with a certain charge Q. By modeling the gate stack as a parallel plate capacitor, one can see that $Q = \frac{A\epsilon_0\kappa}{d_{ox}}V$, where A is the area of the capacitor, ϵ_0 is the

[III] The discussion should actually be focused more on III-As rather than the general III-Vs. In fact, materials like GaN have a totally different surface chemistry compared to In(Ga)As materials[64]. Even if the oxide stoichiometry is similar in different III-As alloys, usually the influence of defects is worse in large band gap materials, such as GaAs, since it is more likely that some defects fall in the band gap range[67].

vacuum dielectric constant, d_{ox} and κ are respectively the thickness and permittivity of the oxide and V is the voltage applied at the gate. When downscaling the channel length, A decreases quadratically and it is not energy efficient to compensate this effect with increasing V. On the other hand, there are limitations in scaling d_{ox}, since tunneling through the oxide starts to be problematic for thin oxide thicknesses. The most efficient way to get around these conflicting requirements is therefore to increase ϵ_{ox}, i.e. to use a high permittivity (high-κ) oxide. For example, the high-κ oxides used in this dissertation are alumina (Al_2O_3) and hafnia (HfO_2) and have relative dielectric constants of 25 and 40, respectively, compared to 3.9 for SiO_2[85].

In the specific case of III-V devices, high-κ oxides are beneficial for two reasons: they are necessary for device scaling and they are also helpful in passivating the surface and removing the III-V native oxides[86].

Atomic layer deposition

ALD is a thin film deposition process, in which two (or more) precursors are dosed on the surface sequentially, one atomic layer per time. In the work presented here, the first precursor is a metalorganic compound and the second one is water, which acts as an oxidizer for the metal, resulting in a high-κ oxide. More specifically, the metalorganic compounds used here are trimethylaluminum (TMA) $Al(CH_3)_3$ when carrying out ALD of alumina and tetrakis-dimethylamino hafnium (TDMA-Hf) $Hf(N(CH_3)_2)_4$ in case of hafnia.

The result of ALD is therefore a thin homogeneous and uniform film, with atomic layer precision (which explains the name of the technique). These characteristics are a consequence of the reaction mechanism, which is shortly sketched hereafter (Figure 2.8). The control of atomic thickness is granted by the fact that the reactions are self-limited, i.e. the reactants of a given precursor in the gas phase are incorporated in the surface only if there are proper reaction sites available at the surface.

The first precursor is dosed in the reactor in gas form. It reacts with the heated substrate, saturating its surface and typically leaving volatile products. A monolayer of the first precursor covers uniformly the surface. This constitutes the first half-cycle of an ALD reaction (Figure 2.8a).

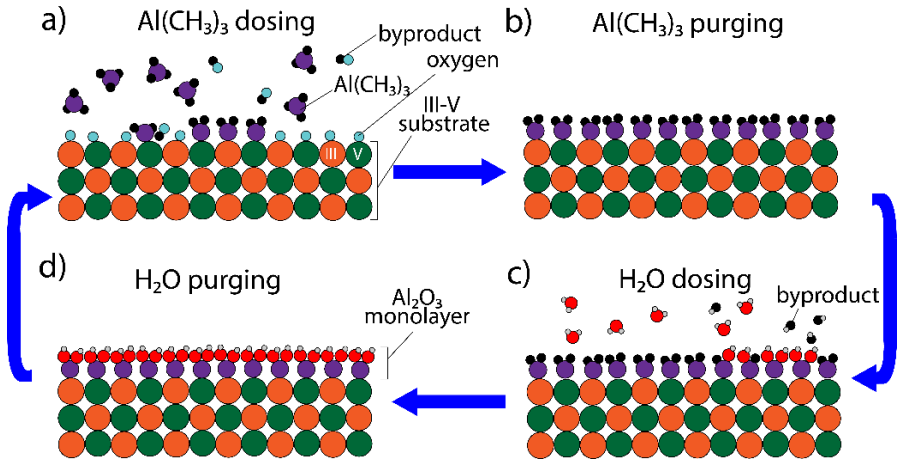

Figure 2.8: Simplified ALD mechanism on a III-V substrate. a) first half cycle of ALD, in which the metalorganic reactant is dosed and it reactively binds with the substrate atom, substituting the native oxide, in the so called self-cleaning effect. b) purge of the metalorganic reactant to prepare the system for the second half cycle. c) Dosing of the oxidant reactant (in this case, water): splitting of the remaining ligand groups and formation of a stable oxide. d) purging of the oxidant; the surface is now ready for another ALD cycle.

Between the first and the second half-cycle, a purge is carried out (Figure 2.8b), meaning that the gas phase with the first reactant is expelled. The purge step is done to avoid undesired reactions in gas phase between the two precursors.

In the second half-cycle, water is dosed in the reactor in gas phase (Figure 2.8c). This oxidizer reacts with the metalorganic precursor covering the surface, providing a homogeneous stable oxide layer (e.g. Al_2O_3 or HfO_2) and organic volatile byproducts. After the second half-cycle another purge step is done (Figure 2.8d), the process can be repeated and the thickness can be controlled by tailoring the number of cycles.

A more detailed description of the process can be found in the references[74, 87-89].

In case of III-V surfaces, the first ALD cycle is crucial for the removal of the native oxides, which is known as "*self-cleaning effect*"[90-92]: the precursor dissociates exchanging one or more ligands with oxygen of the native oxide ("*ligand exchange reaction*"), and the driving force is the increased stability (reduction of the Gibbs free energy) of the ALD oxide compared to the native oxides.

It is worth mentioning that the above mentioned reaction scheme for ALD is a simplification and idealization of the process, which reaction mechanisms are not yet fully understood: incomplete layer growth[93] and/or oxide removal[94], impurities incorporation and diffusion[95], and surface defects are actually possible issues. In Chapter 4.3 and in **Paper III** the surface chemistry modifications during an ALD

reaction are studied in detail, highlighting previously unknown reaction steps and investigating parameters potentially undermining the good quality of an ALD layer.

2.4.3. Thermal oxidation prior to ALD: a novel approach

In this dissertation an alternative passivation method involving an interfacial oxide grown in controlled conditions has been studied (**Paper II**). This passivation method consists in a first step ("cleaning", Figure 2.9) where the native oxides are removed, followed by a controlled growth of an oxide layer (which we call "thermal oxide").

This passivation approach has been shown by different groups[96-97] to improve gate stack performances and to reduce interface defects. The main idea is therefore to replace the native oxide and the defect-rich semiconductor/high-κ interface with a higher quality interface provided by the thermal oxide. The removal of native oxides is in our case done in UHV by annealing the substrate under a flux of atomic hydrogen, as described before.

In this passivation approach, the cleaning is followed by a controlled III-V oxide growth under UHV conditions (thermal oxide, Figure 2.9) by exposing the cleaned surface to a controlled flux of molecular oxygen, with a proper heating of the substrate. The resulting thermal oxide layer has a stoichiometry different than the native oxide, with the presence of only certain oxidation states (that we attributed to In_2O_3 and As_2O_3). The passivation is then complemented with the deposition of an ALD layer, out of UHV conditions.

Paper II aims to bridge the gap between this passivation approach and the observed improved performances by studying the interface chemistry of the III-V oxide with high resolution XPS.

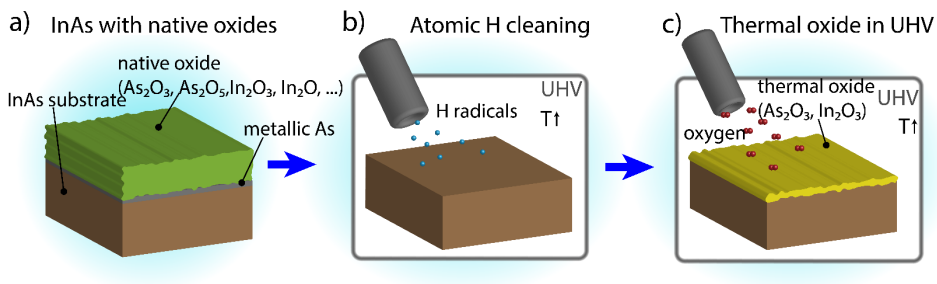

Figure 2.9: Thermal oxidation process: a) Untreated InAs sample, with native oxide with multiple stoichiometry and metallic As. b) Annealing in UHV conditions under a flux of atomic H atoms removes the oxides. c) Deposition of a thermal oxide with controlled composition in UHV by fluxing a controlled O_2 flow at 380 °C.

3. X-rays: a suitable probe for surface and nanostructure characterization

This thesis has the aim to contribute in filling the knowledge gap between device processing and performance by characterizing the relevant III-V model systems. More specifically, the goals are: i) to study the III-V surface chemistry and the influence of device processing, also when in operation; ii) to map and quantify the doping in III-V nanostructures; iii) to measure the strain in III-V nanostructures.

It is clear that, given the heterogeneity of the scientific open issues stated above, a unique technique cannot answer all of them, and that a combination of complementary characterization techniques is needed. X-rays can be used as a powerful tool for these different tasks, by exploiting their different possible interactions with the sample.

3.1. Interaction of X-rays with matter

All analytical techniques rely on the observation of a signal resulting from the interaction between a probe and a sample (Figure 3.1a). The probe which has been mostly used in this thesis consists in X-ray photons. Since they were accidentally discovered by Röntgen in 1895, they appeared as a valuable source for studying matter properties[98]. X-rays are electromagnetic waves with a wavelength in the range between ca. 1 nm and 0.1 Å, which corresponds to an energy range between ca. 100 eV and 100 keV. There are two main possible interactions between the photon electric field[IV] and the matter at the atomic level[99-100], and they are photoabsorption and scattering.

Photoabsorption consists in the absorption of the energy of an X-ray photon by an electron. If we consider an electron of a core level shell (let's assume it is the K shell) and a sufficiently energetic X-ray photon which is absorbed, the electron is ejected from the atom with a given kinetic energy, in order to fulfill the energy balance (Figure 3.1b). The study of the photoelectron characteristics is fundamental

[IV] The X-ray electromagnetic wave has also a magnetic field component. However, since the magnetic scattering is much weaker than the charge scattering it can be neglected here.

in X-ray photoemission spectroscopy, which will be discussed in the next chapter. The core level hole in the K shell left by the electron is an excited state which is not stable, and the system relaxes by filling the core level hole with an electron of an outer shell (for instance, L2), releasing a photon with energy equal to the energy difference between the two shells involved. This process is called X-ray fluorescence (XRF) and the energies of the emitted photons are characteristic and can be used as a chemical fingerprint of the sample, as discussed in Chapter 5. Another relaxation process is the emission of a secondary Auger electron which, conversely to the photoemitted electrons, has a fixed kinetic energy, not depending on the photon energy of the original X-ray probe, but can also be used as elemental fingerprint.

X-ray photons can also get scattered by the electrons of an atom (Figure 3.1c): in the classical description, an X-ray wave exerts a force on an electron, which gets accelerated and consequently re-emits the wave, like in an antenna. In the scope of this thesis only elastic (or Rayleigh) scattering, in which the energy of the incoming and emitted photon is conserved, had a practical use in X-ray diffraction.

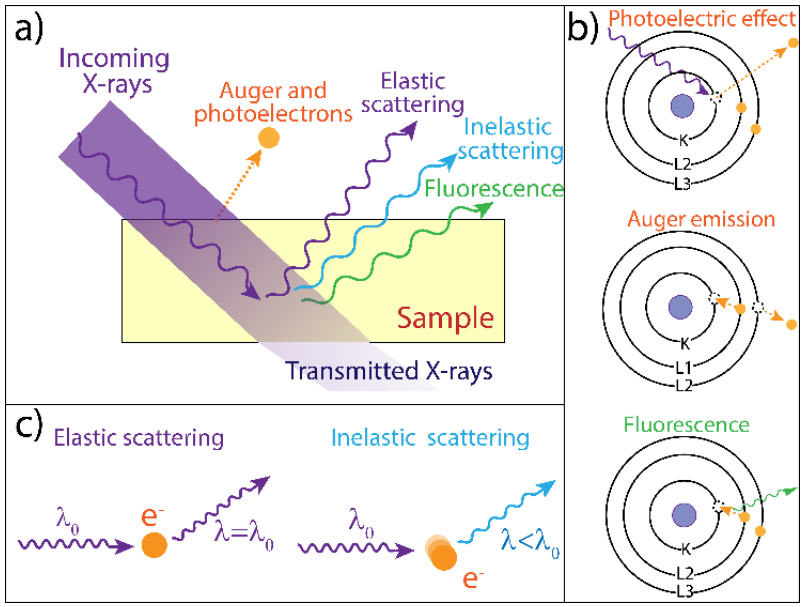

Figure 3.1: a) Interactions of X-rays with matter. Auger and photoelectrons are emitted from the surface, scattering and fluorescence are bulk effects. A fraction of X-rays does not interact and it is transmitted. b) Absorption related effects involving the core level atomic orbitals are sketched. Photoelectric effect: a photon is absorbed and an electron is emitted. Relaxation processes for the inner core hole are Auger electron emission or fluorescence (emission of X-rays). c) Scattering processes: in elastic scattering the electron re-emits the X-ray wave with the same wavelength λ_0, in the inelastic scattering part of the X-ray energy is transferred to the electron as kinetic energy.

If we consider the electrons in atoms belonging to a perfect crystal, the scattered electromagnetic waves can interfere and by that generate a diffraction pattern. This is possible due to the fact that the interatomic distances in a crystalline lattice have a comparable size with the X-ray wavelengths. X-ray diffraction - which will be treated more in detail in Chapter 6 – is therefore sensitive to the spacing of atomic planes, which makes this technique a powerful tool for studying lattice strain.

3.2. X-rays from synchrotron radiation sources

Synchrotron radiation is a high brilliance radiation ranging from infrared to hard-X ray range[101] which can be opportunely manipulated to gain necessary spatial and energetic resolution with a high photon flux.

Synchrotron radiation is produced by electrons accelerated to quasi relativistic speed, which is usually achieved in storage rings of big scale facilities[102] (for example, at MAX IV (Lund, Sweden) the electrons are accelerated to a kinetic energy of 3 GeV). High photon flux is obtained by insertion devices called undulators, placed along the path of the electrons in the ring. These devices consist in periodic arrays of magnets, which impose regular deviations to the electrons from their trajectory. The radiation released by these oscillations experiences constructive interference for certain energies and it can be properly monochromatized and focused by the beamline optics and used in the experimental end station.

Synchrotron X-ray radiation, which has been used in all the papers collected hereafter, offers multiple advantages compared to a conventional laboratory X-ray source. One of the main advances of synchrotron light is the intrinsically higher brilliance (i.e. flux per solid angle per energy bandwidth) compared to lab sources, even 9 order of magnitude more[101]. In practical terms, this means a higher counting statistics during an experiment, quicker measurements and the possibility of focusing the X-ray probe without losing most of the flux. Focusing below 10 nm has been demonstrated with cutting edge X-ray optics[103-104], even if nano-beam spot sizes between 50 and 150 nm are more common; nano-beams in this size range have been used in **Papers IV and V**.

Other important advantages are the possibility of tuning the X-ray energy, as it will be discussed later, and the absence of a high, undesired, bremsstrahlung background, which is instead present in X-ray lab sources.

Synchrotron radiation is therefore an irreplaceable source viable for characterizing the samples presented in this thesis, due to the high brilliance, the flexibility in tailoring energy and size of the X-ray probe, and the availability of end stations with a variety of *in situ* and *operando* setups.

4. X-ray photoemission spectroscopy

X-ray photoemission is a phenomenon consisting in the emission of electrons from a sample as a result from the photoelectric effect due to the irradiation of photons with sufficient energy, typically in the soft X-rays regime[V] (Figure 4.1). By analyzing the kinetic energy distribution of the emitted photoelectrons one can perform X-ray photoemission spectroscopy (XPS): one can also retrieve the binding energy of the core level photoelectrons, that are element specific. XPS is extensively used for surface characterization, and it is of primary importance in studying III-V semiconductors, whose surface quality has been the main obstacle in their use in mass products electronics[64]. Consequently, one can quantitatively estimate the amount of the chemical species present on the surface, and as a matter of fact, the technique is also known as electron spectroscopy for chemical analysis (ESCA) and it is extensively used and standardized also in industry (see e.g. ISO 16243:2011). More interestingly, the binding energy of core level photoelectrons is also affected by the particular chemical environment of the element, allowing to discern, for instance, different oxidation states. This technique can be implemented in many different variants, which have been extensively used throughout the papers presented in this dissertation.

The first part of this chapter deals with the theoretical grounds of XPS and its standard equipment: this introduction allows to interpret the experiments presented in **Papers I and II**, which core features are mentioned. Then, ambient pressure XPS is introduced and the relevant results of **Paper III** are reported thereafter. Finally, the scanning XPS microscopy variant is explained, which was used for **Paper IV**.

[V] Photoemission is not limited to soft X-rays, but can be performed with hard X-rays, that is useful for studying buried interfaces. Photoemission using ultraviolet light as a source is also possible and widely used for studying molecular orbitals. These two variants are out of the aim of this thesis, which is limited to the case of soft X-rays as a source.

4.1. XPS: theoretical and practical aspects

Most aspects of XPS can be understood by considering the underlying photoelectric effect: the fact that absorption of sufficiently energetic light can liberate electrons from the surface was already observed by Hertz in 1887[105], and a formal explanation was given in 1905 – the Einstein's *annus mirabilis* – by the Swiss scientist[106] for which he was also awarded the Nobel prize in 1921. The energetic balance of the photoelectric effect can be written as follows, by considering energy conservation:

$$h\nu = E_b + E_k + \Phi_s \qquad (4.1)$$

where $h\nu$ is the photon energy (with h being the Planck constant and ν the frequency), E_b is the binding energy of the photoelectron, E_k its kinetic energy in vacuum and Φ_s is the sample work function. A simplified sketch clarifying equation 4.1 is provided in Figure 4.1.

The practical meaning of equation 4.1 is that one can indirectly analyze the binding energy of the core levels of interest by irradiating the sample with a soft X-ray beam and measuring the kinetic energy of the photoelectrons with an electron analyzer.

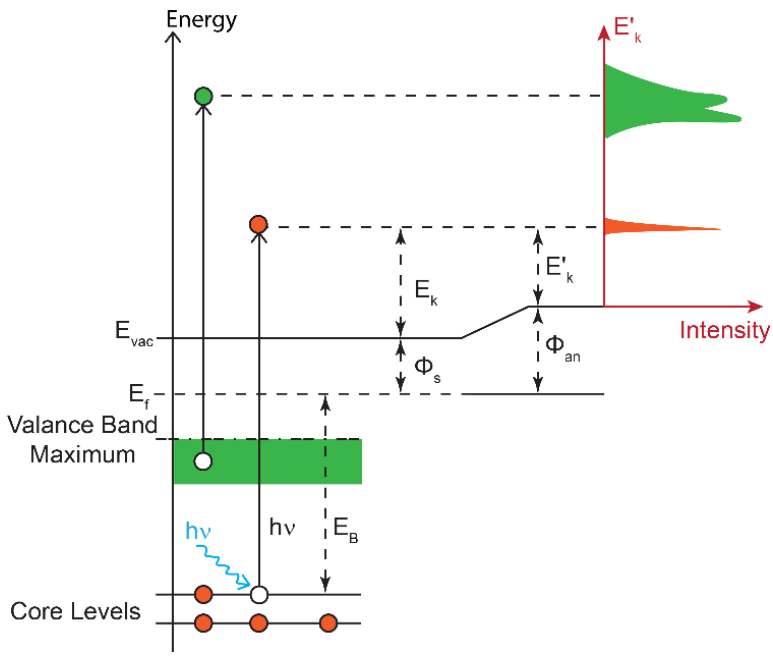

Figure 4.1: Working principle of XPS: an electron of a generic core level (orange) with binding energy (E_b) is photoemitted by a radiation of energy $h\nu$. The kinetic energy of the photoelectron is E_k, whereas E_k' is the kinetic energy measured by the analyzer (right part of the graph). The difference is due to the different work functions of sample (ϕ_s) and analyzer (ϕ_{an}). In green, it is shown a photoelectron emitted from the valence band. [Adapted from ref. [107]]

Strictly speaking, the electron analyzer has an unknown work function Φ_{an}, which is in general different from Φ_s, and determines the measured kinetic energy (E'_k). Therefore, a proper calibration procedure is needed to determine the binding energy E_b. It is worth noting that E_b is referred to the Fermi level E_f of the sample, which is the same also for the analyzer, and a calibration can be done by setting to zero the kinetic energy at the E_f edge. This edge can be easily determined only if the sample is a metal, which is not the case in the research presented in this dissertation, where we considered mainly semiconductors. For semiconductors, in general E_f is in the band gap, where no allowed electronic states are present, its position varies with doping and therefore it is not possible to directly determine it in XPS experiments. Therefore, the binding energies in XPS spectra of semiconductors are calibrated with external standards, typically using the $4f_{7/2}$ peak[VI] of Au, which has a well-known position. Nevertheless, the knowledge of the absolute value of the binding energy is usually not of major interest in this thesis, since it is often sufficient to only consider relative binding energy shifts between two different core levels or between different components of the same core level.

Equation 4.1 describes the energy balance, but not the mechanism or the probability of the photoemission process, which are other crucial aspects when performing a quantitative analysis. The intensity I_i^j of a photoemission peak for the core level *j* of a given species *i* can in fact be qualitatively idealized[108] as:

$$I_i^j \propto \Phi_{(X-ray)} \cdot n_i \cdot \sigma_i^j \cdot P(\lambda) \cdot D \qquad (4.2)$$

where $\Phi_{(X-ray)}$ is the X-ray photon flux, n_i is the number of atoms of the species *i*, σ_i^j is the cross section of the photoelectric process for the core level *j*, $P(\lambda)$ represents the probability of no-loss escape of the electron (depending on the inelastic mean free path λ, discussed afterwards) and *D* is a function which considers the angular acceptance of the detector and its efficiency. The next sections are focused on clarifying the terms that are involved in equation 4.2 and therewith determine the XPS peak intensity.

4.1.1. Quantum mechanical description of the photoelectric effect

A fundamental contribution to equation 4.2 is the cross section σ_i^j, which is related to the probability of the photoelectron emission: in order to better understand this quantity, I am providing here a simplified quantum mechanical description of the photoemission process.

[VI] The notation $4f_{7/2}$ uniquely defines the core level of interest: 4 refers to the principal quantum number (*n*), *f* to the orbital quantum number (*l*), and the subscript 7/2 to the spin-orbit splitting, a fine structure feature described afterwards.

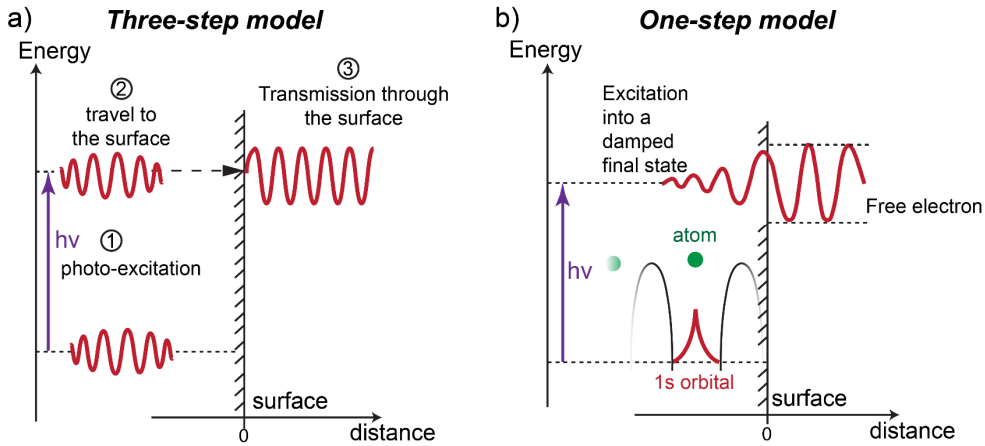

Figure 4.2: a) Three step model: 1) photoexcitation of an electron wave packet from initial to final energy, 2) travel to the surface 3) transmission through the surface. b) One step model: Photoemission happens when the initial and final state wave function overlap. The initial state wave function is a periodic Bloch wave function (the periodic potential of the crystal is sketched with black arcs, and the final state is damped towards the bulk. Damping represents the effects of the electron scattering. [tiles a) and b) are inspired from ref. [109], and ref. [110], respectively]

We can model the whole process in an exquisitely phenomenological way[109, 111] as the result of three distinct steps (Figure 4.2a): i) photo-excitation of the electron ii) travelling of the photo-emitted wave packet through the solid and iii) transmission through the surface as a plane wave, i.e. as a free electron.

A more rigorous description of the photoemission process is given by the so called one-step model[109] (Figure 4.2b), in which we consider directly the transition probability as the overlapping of the wave functions corresponding to an unperturbed initial state of the system, in which the photoelectron is bound to the solid (the initial state Ψ_i) and a final state Ψ_f of the system after the photoemission. This transition can be compactly described by the matrix element,

$$M_{fi} = < \Psi_f \left| H^{int} \right| \Psi_i > \qquad (4.3)$$

where H^{int} is, under the electric dipole approximation, the interaction operator $H^{int} = -e/mc\ [\boldsymbol{A}(r) \cdot \boldsymbol{p}]$, $\boldsymbol{A}(r)$ is the potential of the electromagnetic field and $\boldsymbol{p}$ is the momentum operator.

Now, according to Fermi's Golden rule, one can consider the transition probability per unit time ω, which is proportional to the square of the matrix element:

$$\omega = \frac{2\pi}{\hbar} \left| M_{fi} \right|^2 \delta\left(E_f - E_i - h\nu\right) \qquad (4.4)$$

Where the delta term implies the energy conservation between the final (E_f) and initial states (E_i).

The main problem is now to find an effective expression for Ψ_i and Ψ_f.

A simplified form for the initial and final states of the system with *N* electrons – which in general is not known a priori – can be found by approximating it with the following products:

$$\Psi_i = C\varphi_{i,k}\,\Psi_i(N-1) \tag{4.5}$$

$$\Psi_f = C\varphi_{f,KE}\,\Psi_f(N-1) \tag{4.6}$$

Where $\varphi_{i,k}$ and $\varphi_{f,KE}$ are the wave functions of the electron involved in the photoemission, in the initial (bound) and final (free) states, respectively. $\Psi_i\ (N-1)$ and $\Psi_f\ (N-1)$ are the wave functions of the system with the remaining *N-1* electrons. *C* is an operator which anti-symmetrizes the wave functions properly. If one substitutes equations 4.5 and 4.6 in eq. 4.3, one obtains:

$$M_{fi} = <\varphi_{f,KE}\,|H_{int}|\varphi_{i,k}><\Psi_f\ (N-1)|\Psi_i\ (N-1)> \tag{4.7}$$

This is a useful simplification, since now the matrix element is described with only one-electron wave functions, multiplied with the so called spectral function of the system, or overlapping of wave functions. By assuming $\Psi_f\ (N-1) = \Psi_i\ (N-1)$, which is the *frozen orbital approximation*, the overlapping of wave functions becomes unity.

It is necessary to remark that the frozen orbital approximation does not actually reflect reality, since relaxation processes usually take place, with the system reorganizing the orbital around the core hole in order to minimize the energy. This fact means that the binding energy is in general different from the theoretical E_b expected by equation 4.1 and additional features (out of the aim of this thesis), like satellite peaks can be present.

This brief theoretical *excursus* put in evidence two important aspects: first, the probability of photoemission depends on the magnitude of the relative cross section, which in turn depends on the matrix element of equation 4.7. High cross sections are proportional to a strong overlap between the initial (bound) state $\varphi_{i,k}$ with the final state $\varphi_{f,KE}$ of the photoelectron (Figure 4.2b).

Secondly, E_b is, strictly speaking, not an observable depending only on the photoelectron, as one can argue from a simplistic view of energy balance of equation 4.1. It is actually the energy difference between a final state with *N-1* electrons and an initial state, with N electrons, and therefore it depends on the whole system[112].

4.1.2. Line shape and other features of the XPS spectra

According to equation 4.1 the photoionization is set at a precise energy, therefore in a typical XPS spectrum, where the photoelectron intensity is plotted against the

binding energy, one can expect a sharp peak at the binding energy of the core electron. This peak is actually not a Dirac delta, but the convolution of different broadening functions has to be considered[113].

A fundamental, but minor, broadening is due to the finite lifetime Δt of the hole state[114]: according to Heisenberg uncertainty principle, which states that $\Delta E \Delta t \geq \hbar$, the energy must present a certain uncertainty ΔE.

Another source of broadening is related to instrumental effects (e.g. energy resolution of the analyzer, linewidth of the incoming radiation, etc.) and it is well described by convoluting the line width with a Gaussian function[115]. The good monochromaticity achievable with synchrotron radiation can actually significantly reduce this instrumental broadening compared to lab sources. Several phenomena acting on the XPS process (e.g. temperature of the system[116]) contribute to the Gaussian peak broadening.

An important broadening source is due to the fact that the E_b position may not be exact, but can have a spread, depending on the local chemical environment and its inhomogeneity[117]. This is the case of compounds with mixed stoichiometry, or not well defined stoichiometry, for instance the so called sub-oxides, like HfO_x, where $1 \leq x \leq 2$. This broadening related to the local chemical state is important in **Paper II**, in which III-V oxide peaks showed a larger broadening than their bulk peak counterpart.

Considering these sources of broadening, a practical way to model the photoemission line is to use a Voigt function, which is a convolution of a Lorentzian and a Gaussian. More accurate models, like the Donjac-Sunjic line shape[118], take into account also peak asymmetry, which is peculiar of metallic systems.

In most XPS core level spectra analyzed in this dissertation a fine structure can be observed, consisting in the splitting of certain photoemission lines in two components. This splitting is related to the spin-orbit coupling[109], which is a final state effect typical for core levels having a non-zero orbital quantum number l (i.e. the p, d, and f orbitals). After the photoionization, there is an unpaired electron in the orbital, which spin can be $m_s \pm 1/2$, and the interaction of the spin with the orbital number l can lead to two possible states, characterized by the total angular momentum number $j_\pm = l \pm 1/2$.

For example, in Figure 4.3, a typical As 3d core level spectrum is shown. The splitting of all chemical components into doublets is related to the coupling of l (l=2) with the unpaired electron spin, which results in j=5/2 and j=3/2. The intensity ratio between the $3d_{5/2}$ and $3d_{3/2}$ components is related to the probability of the transition in one of the two states, which in this case is 3:2.

4.1.3. Core level shifts

One of the most appreciable features of XPS is the ability to distinguish different chemical environments for a certain element, which is possible due to core level energy shifts.

The core level binding energy can be shifted depending on the electronic environment in which the photoelectron was embodied[109]. Let's consider for instance an As site bound to In sites, which is the typical case in bulk InAs; the bond has a high covalent nature and one can assume that the valence electrons of the As 4s and 4p shells are evenly shared with the 5s and 5p shells of In (actually, the orbitals are hybridized into $4sp^3$ and $5sp^3$). If now we considered an arsenic oxide like As_2O_3, one can notice that the bonds between As^{+3} and O^{-2} have a high ionic character, i.e. the valence electrons of the As 4p shell will reside mainly at the oxygen sites, meaning that the probability density of their wave function will be low at the positions of the As cores. Consequently, the electrons of the As 3d orbital are not screened by the 4p orbital electrons and they will experience a stronger Coulomb potential from the nucleus. The 3d core level electrons are therefore more tightly bound to the nucleus and their binding energy will be shifted by ca. +3.2 eV compared to the As-In bonds[119]. The situation is even more pronounced when we consider As_2O_5, where As is in the 5+ state, with a binding energy shift of ca. +4.4 eV compared to the As-In bonds[119].

A chemical shift can also be due to a different coordination number of an atomic site. This is the typical case of atoms positioned at the surface, where the coordination number is lower and therefore a shift towards lower binding energies may be observed.

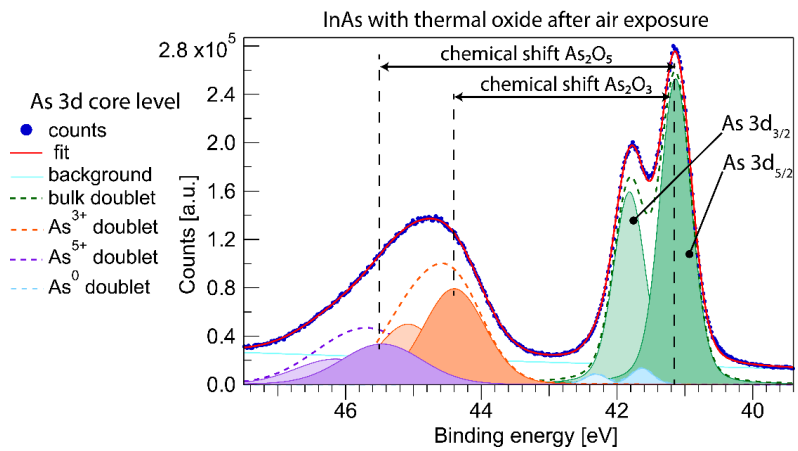

Figure 4.3: XPS spectrum for the As 3d core level of an InAs sample with thermal oxide exposed to air. The chemical shifts of oxides and the doublet components due to the spin orbit splitting are put in evidence. Dashed lines show the sum of the components of each doublet. [Adapted from Paper II]

Chemical shifts have been exploited in **Paper II** to identify the nature of the thermal oxide used for passivating the InAs surface (Figure 4.3).

The suppression of oxides induced by high Zn doping levels in GaAs NWs (**Paper I**) has been deduced by studying the ratio of the different oxide components compared to the Ga 3d and As 3d "bulk" core level peaks.

Rigid shifts involving all core levels, distinguishable from the chemical shifts, are also possible. Rigid core level shifts are due to changes in the position of the surface potential, i.e. of the Fermi level of the surface. A cause can be sample charging, which is a problem for non-conductive samples that are not able to resupply the electrons lost via photoemission. Another more interesting cause can be due to band bending occurring at the surface, which can be caused for instance by surface states, adsorption of species, or Schottky barriers[120].

Surface passivation can also act on the Fermi level position of the surface, and rigid shifts may be observed due to Fermi level pinning/unpinning[121] or more in general, modifications in band banding after the oxide removal. This effect has been observed in **Paper II and III**.

Another factor which influences the band (and core level) positions is doping. Local maps of surface dopant distribution across a semiconductor *pn* junction NW have been obtained in **Paper IV** exploiting this effect.

4.1.4. Probing depth of XPS

We have seen from equation 4.2 that an important contribution to the XPS signal intensity (that was described with the term $P(\lambda)$) is related to the transport of the photoelectron towards the surface. Electrons have in general a very short escape depth due to the high cross section of electron-electron scattering (and phonon-electron scattering, at low energy). This results in a very high frequency of inelastic scattering events, or seen from a distance point of view, a very short average distance between two inelastic scattering events, which is usually called inelastic mean free path (IMFP). The IMFP is similar for all materials and it depends mainly on the kinetic energy of the electrons (Figure 4.4), with a minimum IMFP about 2-5 Å for kinetic energies in the range of 20-100 eV[122].

The probing depth of XPS is therefore conditioned by the IMFP: in fact, the current dI generated by photoelectrons from a layer of thickness dz at depth z can be modelled with an exponential decay[109] $dI \propto \exp\left(-\frac{z}{\lambda\, cos\theta}\right) dz$, where λ is the IMFP and θ is the detection angle measured from the normal to the surface. The probing (or escape) depth can be defined[123] as the depth z_0 (normal to the surface) where the photoelectron flux has a probability of 1/e (ca. 37%) of escaping without major energy losses due to inelastic scattering. The probing depth is proportional to the IMFP and of the same order of magnitude: the XPS signal is therefore usually

limited to the outermost atomic layers of the solid[124]. Interestingly, if we consider equation 4.1, by modifying the X-ray beam energy, the kinetic energy of the photoelectrons is changed accordingly, and consequently also the IMFP and the probed sample thickness: this is a very efficient strategy to perform depth profile analysis of interfacial species on a sample, as it has been done in **Paper II**.

From these considerations one can therefore appreciate the intrinsic surface sensitivity of XPS, and the reason why it is a suitable technique for assessment of interfacial oxide species in III-V semiconductors. On the other hand, the extreme XPS surface sensitivity requires a strict control on contaminants on the surface of the samples, such as adsorbates and native oxides which can occur in atmospheric conditions. For this reason[VII], XPS is typically performed in UHV conditions, i.e. in a pressure range $\leq 10^{-9}$ mbar.

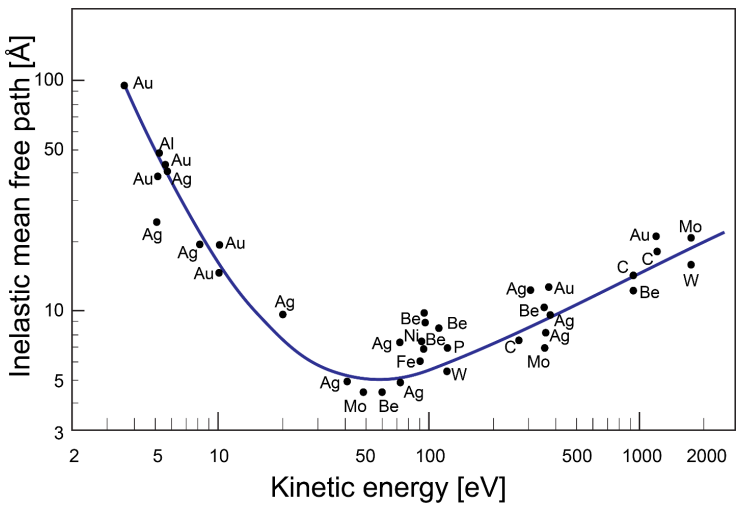

Figure 4.4: IMFP in function of the kinetic energy. The behavior is similar for all the materials. [Adapted from [125]]

[VII] The XPS setup does not require *per se* UHV conditions, but only high vacuum: the inelastic mean free path depends on the probability of the scattering events, which in turn depends on the mean distance of the gas molecules, and the detection of photoelectrons becomes problematic in the 10^{-4} mbar range. A similar argument holds also for the scanning tunnelling microscope setup discussed later.

4.1.5. XPS experimental setup

According to equation 4.2, X-ray beam characteristics and the detection of the emitted photoelectrons play an important role in the feasibility of an XPS experiment.

The photon flux is crucial to ensure a sufficient signal to noise ratio on the detector. Traditionally, in lab equipment X-rays are supplied by X-ray tubes, where the characteristic X-rays are emitted from an anode (typically the Al Kα emission line, which has a photon energy of 1486.7 eV), and an undesired continuous bremsstrahlung is also produced. This source type has two other disadvantages: the photon flux is intrinsically limited and the energy of the beam cannot be changed, since it is determined by the material of the anode.

Synchrotron X-ray radiation generated by undulator sources - which is the case for all the XPS research of this dissertation - can improve these aspects[101], relying on higher brilliance and the possibility of tuning the photon energy[108]. As mentioned before, the possibility of changing photon energy is useful to perform depth profile analyses of the sample.

Regarding the detection apparatus, the photoelectrons are focused on the entrance slit of the hemispherical electron energy analyzer (EEA) and they are accelerated or retarded by electrostatic lenses. This is done so that only the electrons with the right kinetic energy matching the pass energy (E_{pass}) of the EEA can pass through it. The EEA goal is to filter the electrons depending on their kinetic energy, and in combination with the electrostatic lenses the entire kinetic energy range of interest can be scanned. The EEA is composed by two opportunely spaced concentric half-spheres (Figure 4.5) and a certain potential difference is applied to them. The electrons are deviated by the electric field, and only the ones with a certain kinetic energy range have the proper trajectory to reach the micro channel plate (MCP) at the end of the EEA. The MCP consists of several channels which are calibrated to a certain kinetic energy and can be read out simultaneously. At the MCP, the photoelectrons are multiplied and they generate a current signal that is then recorded by a detector.

Only electrons with a certain kinetic energy interval, are allowed to pass through the EEA, and this interval can be expressed as $E_{pass} \pm \Delta E_a$. The uncertainty ΔE_a is important, since it gives the resolution of the EEA. ΔE_a affects also the spectra resolution, since this energy width is distributed over the number of channels of the MCP. The value of ΔE_a is proportional to the pass energy and it depends on the radii of the hemispheres, on the acceptance angle of the electrons and on the entrance and exit slit widths. The photoelectrons with kinetic energies outside this interval collide instead on the hemispheres of the EEA. During a typical experiment, the pass energy has to be optimized so that enough photoelectron flux is allowed through the EEA to give enough counting statistics, while avoiding on the other

hand loss of resolution or saturation effects on the detector. In this dissertation, the spectra were acquired in the so called fixed analyzer transmission (FAT) mode: the potential difference between the EEA hemispheres was kept fixed and the retardation voltage in the electrostatic lens system was swept. This voltage accelerates or decelerates the photoelectrons so that the complete kinetic energy range of interest can be collected, while keeping the same pass energy for the whole spectrum.

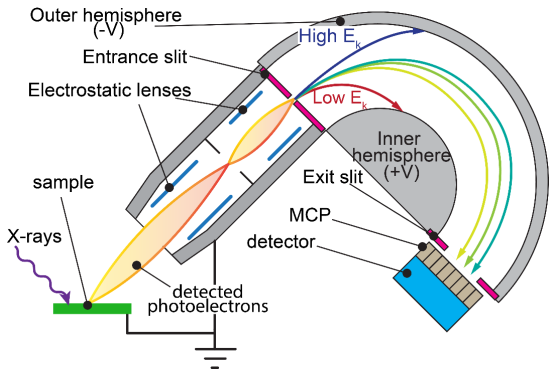

Figure 4.5: XPS setup: the photoelectrons are collected and focused by the electrostatic lenses, whereas the hemispherical EEA selects only those photoelectrons with the proper kinetic energy range (represented with arrows), which are multiplied by an energy dispersive MCP and then detected. [Adapted from ref. [107]].

4.2. Synchrotron based XPS as a tool for investigating technologically relevant III-V surfaces

The tunability of photon energy and the high brilliance of synchrotron radiation X-ray sources allow flexible, faster XPS measurements with a higher statistical quality compared to a laboratory X-ray source. In other terms, the use of a synchrotron source turns a classical surface science technique like XPS into a cutting edge technique to characterize complex material systems. Hereafter, it is shown that synchrotron based XPS was an excellent tool to characterize the challenging materials system studied in **Paper I and II**.

4.2.1. XPS study of effects of Zn doping on the surface of GaAs aerotaxy NWs

It is known that dopants not only determine the functionality, but can also influence the morphology of III-V NWs[46], comprising also GaAs NWs produced via

aerotaxy[42], that are promising templates for low cost NW based solar cells. The incorporation and diffusion of *p* type dopants like Zn in aerotaxy GaAs NWs is different from what happens in epitaxial growth, and higher dopant concentrations (up to 10^{20} cm^{-3}) are possible[44]. The effect of such potentially high Zn dopant concentrations on the surface of aerotaxy GaAs NWs is still not fully understood as well as the characterization of the native oxides at their surface. The study of the surface of these samples is indeed very important, since a poor passivation of the surface can lower the recombination times of the charge carriers hampering the performances of the solar cell.

NWs are a challenging sample for a laboratory XPS setup, due to the intrinsic low signal, that depends on the coverage of the NWs on the substrate, that cannot be easily controlled (Figure 4.6a), and the detection of Zn would require even more unrealistically long acquisition times, due to the low concentration of the dopants in the NWs. Synchrotron radiation XPS can overcome these shortcomings thanks to the high brilliance of the source.

For this reason, in **Paper I** synchrotron based XPS has been used to characterize three batches of GaAs aerotaxy NWs produced under increasing molar fractions of the Zn doping precursor. It has been demonstrated that Zn can be detected (Figure 4.6b) for the NWs grown under high doping conditions (i.e. with a unitary Zn/Ga precursor ratio).

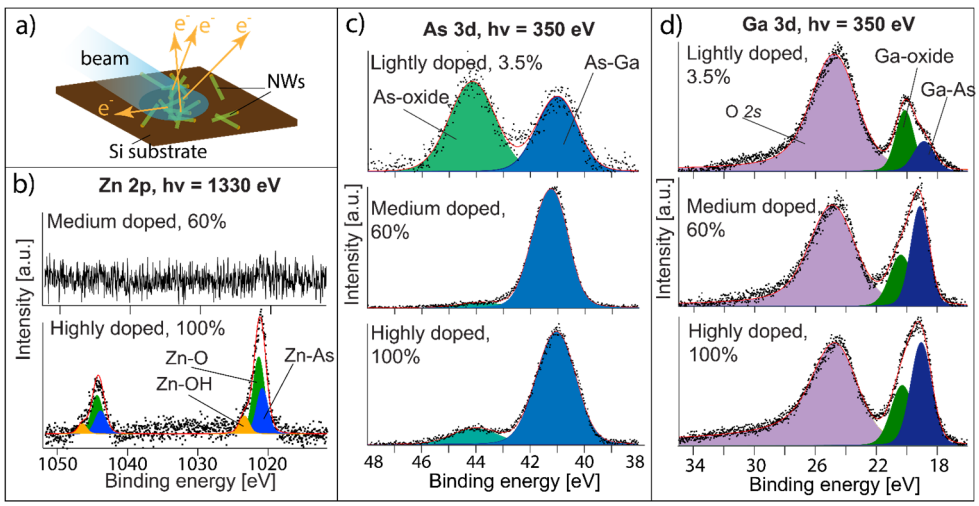

Figure 4.6: XPS on GaAs NWs with different levels of doping. a) Experimental setup: the NWs are randomly distributed on a Si substrate and probed with the beam. The photoelectrons are represented with arrows. b) Zn 2p core level spectra: Zn is not detectable for low and medium doped samples, but it is detectable in the highly doped sample. c) As 3d core level spectra: the increase in dopant concentration (from top to bottom) suppresses the As-oxides. The percentage value represents the ratio of Ga/Zn precursor molar fractions. d) Ga 3d core level spectra: the Ga-oxides are also partially suppressed for higher Zn precursor molar fractions. [Adapted from Paper I]

The most interesting and surprising result of this study is that the presence of Zn on the surface seems to suppress the formation of native oxides when the NWs are removed from the reactor. In fact, the oxide components of the As 3d and Ga 3d core level spectra (Figure 4.6c,d) are suppressed or strongly decreased for medium and high Zn doping levels. It is supposed that a Zn layer is formed at the surface protecting the NW from oxidation; considering that native oxides are in general a reason of poor passivation for III-V surfaces, this discovery may have a big impact for future passivation of highly doped aerotaxy NWs.

4.2.2. XPS surface study after subsequent processing steps: a new passivation treatment on InAs

XPS can be used in conjunction with surface treatments performed *in situ* in the UHV environment, so that the effect on surface chemistry of each processing step can be readily monitored with XPS. This approach, combining processing and analysis in the same setup, is widely used in surface science and it fits well also for the case of III-V semiconductor passivation, where improvements of device performance are observed but the effect of each processing step on the surface are often not fully clear.

This knowledge gap exists also for the novel passivation process for InAs substrates (Section 2.4.3), consisting in the removal of the native oxide by annealing the substrate under atomic hydrogen and then growing of a thermal oxide prior to the ALD. Ko and coauthors showed that the thermal oxide provides better MOS performance[96], but a thorough surface characterization is missing.

XPS fulfills this task, since it is surface and chemical sensitive. The relevant steps of this passivation routine can be identified and each of them can be characterized with XPS: i) reference substrate (untreated InAs sample with the native oxide); ii) atomic hydrogen cleaning of the sample; iii) thermal oxidation in UHV; iv) exposure of the sample with the thermal oxide to air; v) Al_2O_3 deposition via ALD on the sample of step iv).

The motivation of exposing the thermal oxide to air prior to the ALD is dictated by the need of breaking the UHV conditions when transferring the sample to the ALD machine, which is the case for many experimental setups.

The XPS experiment (**Paper II**) performed with a synchrotron X-ray source, allowed to evaluate the content of the different species at the surface, since their peaks show a well-defined chemical shift compared to the "bulk" peak (i.e. As-In bonds for the As 3d core level and In-As bonds for the In 4d and 3d core levels).

One of the most important observations is that the stoichiometry of the thermal oxide grown in UHV conditions is completely different from the composition of the native oxide (Figure 4.7). The latter is characterized by a combination of As^{3+}, As^{5+}

and In^{1+} and In^{3+} components, whereas the thermal oxide shows a well-defined stoichiometry (Figure 4.7e,f), mainly composed by As^{3+} and In^{1+} oxides. The different stoichiometry of the thermal oxides arises from the controlled oxidation conditions in UHV (substrate temperature, oxygen partial pressure and time of oxidation), favoring the metastable[69] As^{3+} oxidation state. The thermal oxidation reduces also the intensity of the metallic As peak (As^0), representing the As-As bound. This can play an important role in defect passivation, since it is known that As in its metallic state is detrimental for MOS performance[67].

The thermal oxide is not stable under exposure to atmospheric pressure, but instead tends to revert to the composition of the native oxide.

Regarding the oxide composition, it should also be kept in mind that the representation of a native oxide as a combination of stoichiometric compounds with well-defined oxidation numbers (e.g. As^{3+} and As^{5+}) is a simplification. Real native oxides are usually not stoichiometric and are given by a combination of sub-oxides, with different local chemical environment and oxidation states[70].

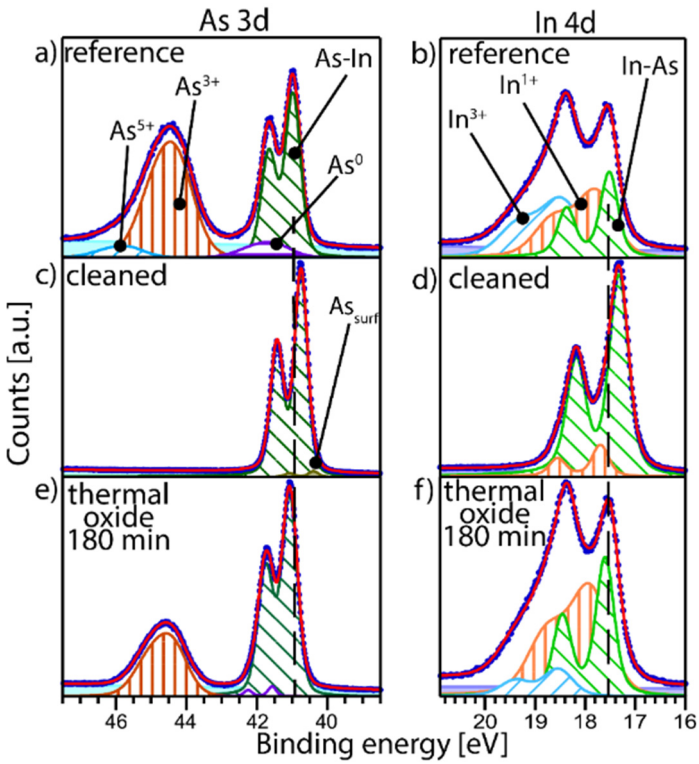

Figure 4.7: Passivation process studied with XPS: reference, hydrogen cleaned and thermal oxide in UHV for As 3d (a,c,e) and In 4d core levels (b,d,f). The relevant spectra components are put in evidence: As^{5+} is not present in the thermal oxide and In^{3+} is reduced. [Adapted from Paper II]

The photon energy can be modified in a synchrotron XPS beamline, and this parameter was actually changed in the study of **Paper II** to obtain similar kinetic energies for the photoelectrons of the As 3d and In 3d core levels, so that the probed depths are comparable.

Moreover, by increasing the photon energy for both core levels, the kinetic energy of the photoelectrons increases, according to equation 4.1. If that is the case, also the IMFP of the photoelectrons increases, which means that different probing depths can be explored. This strategy was used to study the composition of the oxide at different probing depths and it can be observed that the oxide peaks are dominant compared to the bulk peaks (Figure 4.8a, b) when the kinetic energy is low, i.e. when the signal is surface sensitive. One can therefore study the ratio of different oxide components in function of the kinetic energy, and thus of the probed depths. Such a depth profile analysis has been performed after the sample with thermal oxide has been exposed to air (Figure 4.8c). This analysis put in evidence an interesting fact: the InAs thermal oxide not only is not stable when exposed to air, but it shows also a gradient in composition in its thickness. Surprisingly, the As^{5+} oxidation state was found more preponderant towards the bulk (Figure 4.8c, yellow curve). This fact suggests that the thermal oxide is porous, since the oxygen can permeate it in depth and oxidize the material at the semiconductor-bulk interface.

The results highlighted here are significant since the specific stoichiometry found for the thermal oxide can be the main cause for the improvements observed in the electrical measurements on the same samples (even if the thermal oxide was partially degraded by air).

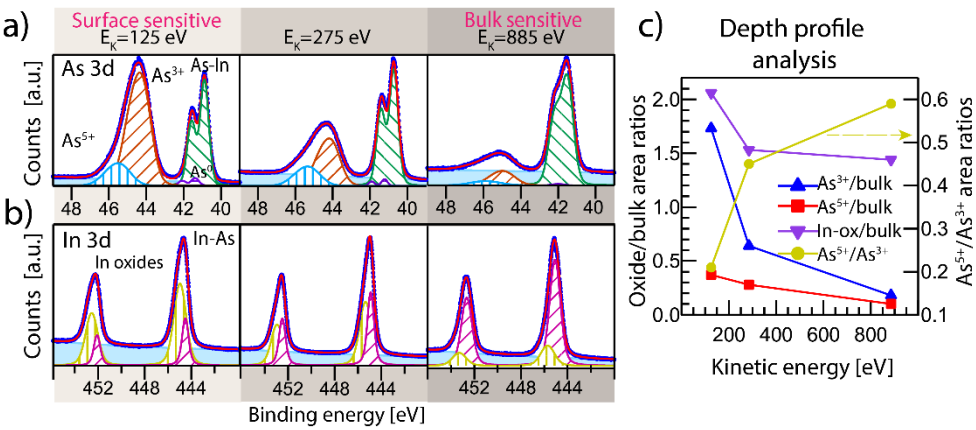

Figure 4.8: As 3d (a) and In 3d (b) spectra for thermal oxide in air for increasing kinetic energies (left to right). The quantitative results are reported in c). Higher kinetic energy means more bulk sensitive signal. [Adapted from Paper II]

The vulnerability of the thermal oxide at atmospheric pressure is an important observation obtained with XPS, suggesting therefore that performing ALD without breaking the vacuum could be a significant improvement in the processing. A final consideration has to be done about the ALD step, for which a partial self-cleaning effect on the thermal oxides was observed. However, the exact dynamics governing the complex ALD reaction cannot be fully described by this experiment, performed after the ALD, since an *in situ* XPS study during the reaction would be needed, which is the topic of the next chapter.

4.3. Ambient pressure XPS

XPS is traditionally operated in UHV conditions. Whereas this controlled environment guarantees *clean* surfaces that can be used as model systems in surface science, on the other hand it cannot reproduce phenomena of technological interest taking place at higher pressures. The lack of XPS information in the pressure interval ranging from high vacuum to atmospheric pressure is usually called *pressure gap*[126], and it is highly detrimental for applied science for mainly two reasons. First, real devices are reasonably produced and used in atmospheric conditions, or in mild vacuum conditions at most and it is important to study adequate model systems in these conditions. Secondly, several processing reactions occurring in gas phase, like for instance ALD, are performed and can only be studied in this pressure range.

The aim to overcome these shortcomings is to carry out XPS in a near atmospheric pressure range. This cannot be easily accomplished due to the high cross section of electrons-matter interaction, which results in very short IMFPs. While the extremely short IMFP in solids ensures surface sensitivity of XPS, on the other hand it implies that interaction of electrons with gas molecules outside the sample cause a severe loss of the detected intensity. To have an idea of the order of magnitude, in average, an electron travelling with an E_k of 400 eV in oxygen gas with a pressure of 1 mbar gets inelastically scattered after approximately 4 mm, which is sensibly less than the distance needed to pass through the electrostatic lenses and the EEA[127]. This limitation translates in the need of a base pressure of at least 10^{-6} mbar for soft X-rays in order to perform standard XPS, or in other terms, this technique cannot be operated in the aforementioned pressure gap.

A particular version of XPS, known as ambient pressure XPS (AP-XPS)[VIII], can circumvent this disadvantage, by using differential pumping stages up to the

[VIII] A common nomenclature for this technique is also high pressure XPS (HP-XPS). Since "high" could be interpreted differently in different contexts (e.g. high pressure powder X-ray diffraction, in which pressures in play can go up to the GPa range), I preferred to use the "AP-XPS" term.

analyzer[128], in order to allow a local high pressure environment close to the sample while minimizing the photoelectron scattering losses[127, 129]. Local pressures of 100 mbar have been reported[130], however operating pressures in the range of up to 20 mbar are more common in flexible setups[126, 131]. The stages are connected through pinhole apertures, and usually a difference in pressure of eight orders of magnitude is maintained between the sample and the analyzer[132]. The high pressure length that the photoelectrons travel through is confined close to the sample and it is usually less than 1 mm (in the same size range as the nozzle diameter d) [127, 131, 133]. Actually, the optimization of the distance l between the sample and the nozzle of the first pumping stage is an important design parameter: if it is too long ($l \gg d$), the scattering of photoelectrons with gas molecules suppress most of the signal, whereas if it is too short ($l \ll d$), the gas pressure distribution around the sample is inhomogeneous.

The pioneering work of the Siegbahns[134] in the 1970s put the basis for the AP-XPS approach; however this and similar instruments[135-136] were equipped with a traditional X-ray lamp, characterized by low brilliance. A substantial improvement was introduced by the use of synchrotron light sources[137], which allowed to increase the count rate dramatically.

Another arrangement which contributed to reduce the loss of photoelectrons was the introduction of electrostatic lenses for each differential pumping stage[138]. The isotropic spread of the photoelectrons from the sample and the low acceptance solid angle of the pinholes is a major cause of loss of signal, since the photoelectrons get blocked by the walls of the pumping stages. A pertinent focusing by electrostatic lenses can overcome this issue (Figure 4.9).

A characteristic feature (Figure 4.9) of the HIPPIE beamline (MAX IV Laboratory, Sweden) at which the experiment of **Paper III** was done, is the use of a dedicated ambient pressure cell[126].

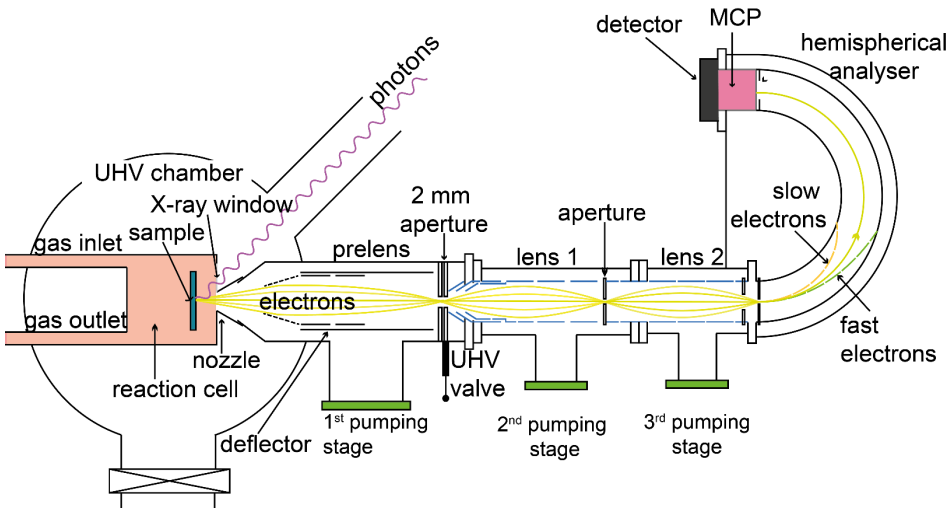

Figure 4.9: Experimental setup of the AP-XPS HIPPIE beamline. The reaction cell is placed inside the analysis chamber and is connected to the gas lines. It can be removed, allowing experimental flexibility between near ambient pressure and UHV. Three pumping stages separated by pinhole apertures give a differential pumping between the sample area and the analyzer (on the right). Electrostatic lenses focus photoelectrons at the aperture, to avoid intensity losses. [Adapted from ref. [110]]

The idea is to encapsulate the sample into a small reaction cell (ca. 0.5 l volume) connected with inlet and outlet gas manifolds, separating it from the rest of the chamber, which remains in high vacuum conditions (ca. 10^{-6} mbar when operating 1 mbar inside the cell). The X-rays can enter the cell through proper X-ray transparent windows (typically Si_3N_4 or Al). One of the advantages of this cell setup is the possibility of quickly controlling and changing the gas environment inside the cell, reducing contamination risks. The setup also maintains UHV capabilities after the ambient pressure experiment. The design with a reaction cell inside the analysis chamber docking to the aperture of the pumping stage is innovative for AP-XPS and it is known in the field as the "Lund approach"[126] and offers unprecedented experimental flexibility. The possibility of interchanging quickly the gas phase reactants supply is ideal for our scope of mimicking the ALD process, where the two precursors are alternatively pulsed.

4.3.1. AP-XPS for studying *in situ* ALD on InAs

Standard XPS is a powerful tool to characterize III-V new semiconductor passivation approaches[16, 86, 90, 139] as it has been demonstrated in **Papers I and II**. However, these studies can be regarded as a *post mortem* analysis, since all the measurements are performed after and not during each processing step, which usually require environments falling in the aforementioned pressure gap.

AP-XPS opens up new horizons for an improved understanding of surface reactions relevant in the processing of III-V surfaces for electronic devices. This approach has in fact been used in **Paper III**: in this study a typical ALD reaction has been reproduced and characterized *in situ* in the AP-XPS setup, and it revealed that an ALD reaction model that was widely accepted in semiconductor research needs to be modified.

The study focuses on the chemical reactions occurring during the first ALD cycles. These first steps and especially the first half-cycle, are very important to determine the self-cleaning effect, and more in general, the quality of the high-κ layer[91, 140] and the amount of interface defects[141]. The AP-XPS setup was arranged to mimic the ALD process in order to shed light on the time evolution of surface chemistry: the substrate, precursors, dosing mode and operative conditions (temperature and pressure) are comparable with the ones used in commercial ALD machines, which makes the study of remarkable industrial interest. More specifically, an ALD reaction of HfO_2 on InAs substrates has been reproduced in the AP-XPS setup, with Hf-TDMA as precursor and water as oxidizer. The choice of HfO_2 is related to the high interest in the community because of its high permittivity and high thermal stability[141]. The relevant core level lines can be monitored in real time before, during, and after the sequential dosing of the two reactants. Moreover, the flexibility of the reaction cell setup allows also to operate XPS in UHV, with improved flux and resolution to evaluate the surface chemistry after the reaction. This operation mode proved also that the final stoichiometry of the sample studied here is fully comparable with analogous samples obtained with commercial ALD[16, 94].

The time resolved investigation of the As 3d core level showed the As-oxides removal from the surface during the first half cycle due to the self-cleaning effect (Figure 4.10a,b). The simultaneous study of As 3d with the In 4d/Hf 4f energy spectral range showed also the formation of a Hf oxide layer on the surface (Figure 4.10c). Interestingly, the oxide removal was neither homogeneous nor instantaneous, since As_2O_5 oxides were removed first, followed by As_2O_3 and, partially, In-oxides.

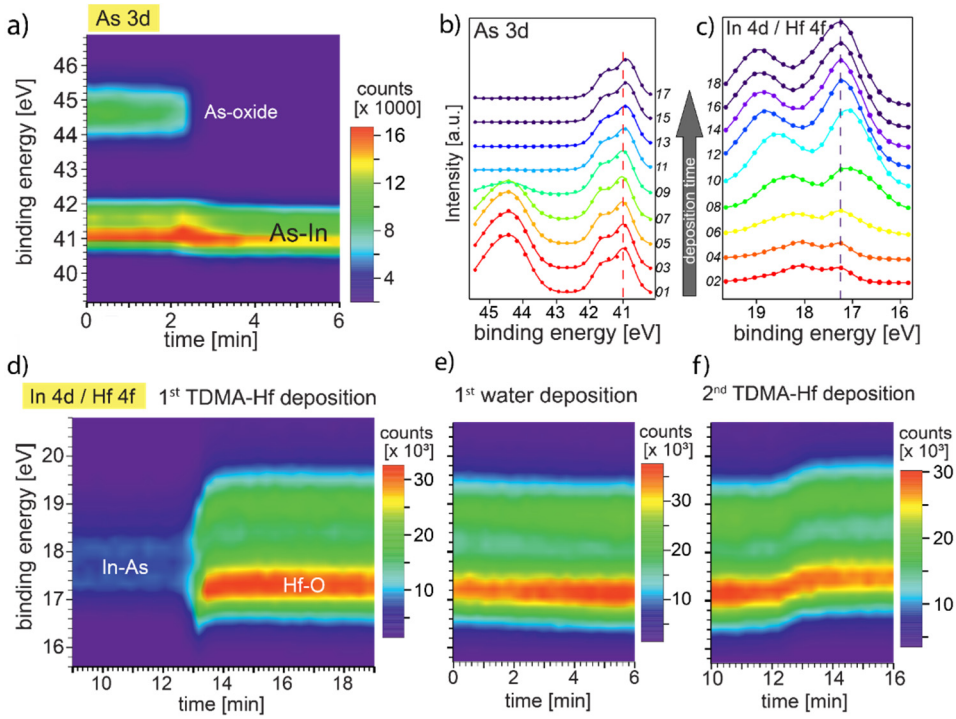

Figure 4.10: a) Time resolved XPS spectra for As 3d: the self-cleaning effect is visible (suppression of oxide peaks). The first half-cycle spectra for As 3d (b) and In 4d/Hf 4f (c) during the reaction have been extracted and analyzed. Hf 4f/In 4d (d,e,f), during the first (d) and second (e) ALD half-cycles. f) shows the TDMA-Hf deposition after the first cycle. The binding energy shift is visible, as well as the changes in intensity. [Adapted from Paper III]

Additional information can be extracted by studying shifts in binding energy. In the first half cycle, at the inset of the Hf peak appearance (Figure 4.10d) an abrupt shift towards lower binding energies was noticed. This observation was attributed to a chemisorption step prior to the ligand exchange reaction. As supported by density functional theory calculations[142], a nucleophilic attack of the amide group to the native oxide surface has been hypothesized, with the result of increasing the electron density at the Hf site and lowering the binding energy due to a shielding effect (more details can be found in **Paper III**).

An interesting aspect emerging by comparing the time sequence of As 3d and In 4d/Hf 4f spectra is that the Hf-oxide forms after and not during the native oxide removal (as in the standard ligand exchange model), and therefore the self-cleaning can rather be attributed to the chemisorbed precursor molecules.

By comparing the first and second half cycles (Figure 4.10d,e,f) it was observed that Hf switches between two conformations, depending on the bonding of Hf: to In-O

groups after the first half cycle and with –OH groups after the second half cycle, giving an experimental evidence of the theoretically postulated hydroxylation step[87].

The most important outcome of this study is that the simplified ideal ALD mechanism of ligand exchange reaction followed by hydroxylation must be revised. The chemisorption step of the precursor, experimentally discovered in this work, is supposed to control the self-cleaning effect, and therefore is important to ensure an homogeneous thin film of HfO_2.

Additionally, by performing the ALD reaction at different temperatures, it was found that the oxide removal was incomplete (Figure 4.11a) for substrate temperatures below 200°C. Moreover, amines impurities were detected in the N 1s spectra of the sample treated at low temperatures (Figure 4.11b) which should therefore be avoided in this process to avoid poor passivation and organic contamination.

Summarizing, this study provided information of both fundamental and practical interest, since it can help in understanding the ALD process and improve the film quality. In fact, the native oxide self-cleaning is neither homogeneous nor abrupt, and therefore longer precursor pulses can help in full oxide removal. Moreover, the chemisorption of the precursor, neglected in previous models, indicates that this step can be crucial in determining the completeness of the ALD layer.

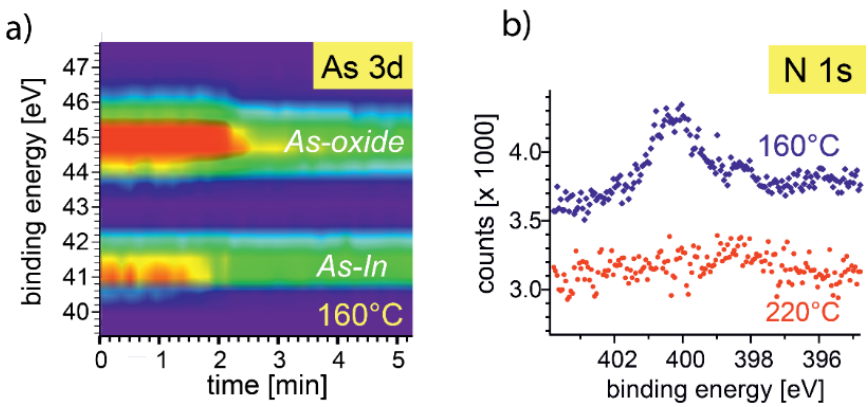

Figure 4.11: ALD dependence on temperature: a) Incomplete native oxide removal at low temperatures (160 °C). b) N 1s core level peak indicates an incorporation of organic compounds at low temperatures, which is absent at 220 °C. [Adapted from Paper III]

4.4. Scanning Photoelectron Microscopy

We have discussed how XPS can provide valuable surface chemistry information about the sample area irradiated by the X-rays, which usually has a size in the submillimeter range. This means that in a standard XPS equipment it is not possible to distinguish with precision the position from which the photoelectrons where emitted. This is in general not a drawback for samples that are laterally homogeneous at a macroscopic scale, but it can be a shortcoming when investigating nanostructures like NWs, where the beam spot is typically much larger than the size of the features of interest. Nevertheless, one can still use XPS and obtain valuable information on average surface chemistry, but one is restricted to large ensembles of nanostructures.

The idea of combining high lateral spatial resolution with spectroscopy (i.e. spectromicroscopy) is therefore very tempting and not new, since the first attempts date back to the 1930s[143].

Nowadays, a wide number of possible designs and concepts are available[144-147] to combine photoelectron spectroscopy with microscopy. Two main approaches are used, depending how the spatial resolution is achieved. In the family of the so called *imaging microscopes*[144], like the photoemission electron microscope (PEEM), a magnified image of the sample is obtained by focusing the photoemitted electrons with proper electromagnetic optical elements. Another less common option - which has been used in this dissertation - is given by *scanning microscopes*, where the concept consists in illuminating and scanning the sample with a focused X-ray probe, and acquiring the local photoelectron signal.

4.4.1. Equipment and operation modes

The equipment of the scanning photoelectron microscope (SPEM) used in **Paper IV** is presented. Even if the layout of a SPEM can differ substantially from this one, there is no loss of generalization, given that the main elements discussed here are always present.

Figure 4.12a shows a sketch of the SPEM that we used at the ESCAMicroscopy beamline at the ELETTRA synchrotron facility (Trieste, Italy)[148-149]. The X-ray beam is demagnified by a proper X-ray optic device and it is scanned on the sample surface (in practice, it is the sample, mounted on a piezoelectric motors stage, which moves with respect to the beam); the signal is then filtered by an EEA and acquired with an energy sensitive MCP.

The light source for SPEM is provided by a third generation synchrotron. In fact, one of the main drawbacks which historically hindered the development of such instruments[150-152] was the lack of a sufficiently bright X-ray source, resulting in

insufficient photoelectron signal and/or very long acquisition times. The low-emittance characteristics of synchrotron sources is also crucial for achieving a good focusing due to the low beam divergence.

The focusing element is a Fresnel Zone Plate (FZP), which is a diffractive lens routinely used in many other facilities around the world since it gives an optimal compromise between flux and resolution[145]. It consists of concentric rings, whose spatial density increases radially (Figure 4.12a), and this geometry works as a diffraction grating that focuses the beam at a certain focal length. A central stop and an order sorting aperture put between the FZP and the sample cut the transmitted beam and the higher diffraction orders.

The focusing is dependent on the geometry of the FZP and on the X-ray wavelength. Therefore, when changing photon energy, the focal distance changes and the setup has to be realigned. Other practical consequences are geometrical constrains, i.e. that the beam impinges only normally to the surface and that the sample-optics working distance is limited by the focal distance, typically in the range of 3-8 mm [144]. Even if spatial resolutions below 15 nm have been reported[153-156] in specific soft X-ray range and setups, a more realistic value is between 30 nm [157] and 150 nm[158]. The spatial resolution is limited by the intrinsic diffraction limit δ_i ($\delta_i = 1.22\Delta r$, where Δr is the radial distance between the two outermost rings), but also by size, divergence and monochromaticity of the X-ray source. When scanning the sample, the step size and the vibrations of the setup influence the maximum obtainable resolution.

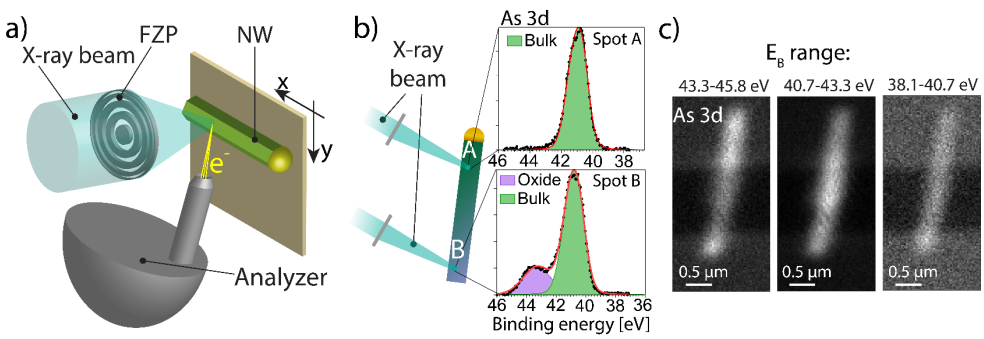

Figure 4.12: a) SPEM setup: the X-ray beam is focused on the sample by the FZP. The local signal is acquired by an EEA and the sample can be moved under the beam in the x and y directions b) micro-XPS mode of an InAs NW: the beam is positioned on a spot of interest and a local high resolution XPS spectrum is acquired. c) Imaging mode of the same InAs NW: the sample is scanned under the beam and a low resolution XPS spectrum is acquired. The dataset is 3D (x,y,E_k) and by summing the intensity of a certain analyzer channel interval, different features can be put in evidence. The oxide location is visible in the first tile, at higher binding energies.

Energy filtering of photoelectrons is fundamental in defining the image contrast in SPEM. In our experiments, we operated the SPEM using a EEA equipped with a MCP with 48 channels[159]. The SPEM can actually be operated in two distinct modes, i.e. in *micro-XPS mode* and in *imaging mode*[144].

The first mode, i.e. the *micro-XPS mode,* is basically a local XPS investigation (Figure 4.12b), in which the X-ray probe is addressed on the feature of interest and a high resolution XPS spectrum is acquired.

The second mode, i.e. the *imaging mode*, records maps of an area of interest, where the contrast is given by the local chemical and electronic states. This is achieved by scanning the X-ray probe on the sample and quickly collecting at each position the photoelectrons within the energy window covered by the multichannel detector[145]. In this way, a 2D map is simultaneously acquired for each channel, i.e. for different kinetic energies. In other terms, the imaging mode provides a 3D dataset, in which each pixel of the image embeds an entire XPS spectrum. An elemental contrast can be easily obtained by centering the energy window around the energy of a core level of interest and summing the intensity of all the channels, with the bright areas identifying a high content for a given element. More interestingly, by summing the intensity of specific channels, one can obtain maps of specific chemical states for the given core level (Figure 4.12c). This mode can also be exploited to detect local changes in the surface potential, e.g. due to an applied external voltage or to a certain doping level. In fact, a rigid shift of the core level lines would cause part of the peak to fall outside the energy window covered by the channels, with a lower total intensity being recorded by the detector. From an operational point of view, the imaging mode is useful also to roughly detect local features of interest which can then be thoroughly studied in high energy resolution with the micro-XPS mode.

Finally, it is important to remark that SPEM, whereas it has a lower spatial resolution than PEEM (in order of 10-20 nm[144, 160]), has the advantage that *operando* measurements can easily be carried out. In fact, in SPEM the sample potential can be modified with a small external voltage supply and is not required to be kept fixed at high voltages, like in PEEM (about 20 kV).

4.4.2. SPEM as a tool for *operando* surface potential measurements of solar cell NWs

SPEM has the capability of mapping the surface potential and chemistry at a local level and therefore can be used to characterize nano-devices under *operando* conditions. In **Paper IV**, the surface potential drop across InP NWs with an axial *pn* junction in dependence of an external bias has been monitored with SPEM. The InP NWs investigated here are part of a research project building on NWs solar cells with world-record efficiency[58, 161]. One of the most critical loss mechanisms for NW solar cells is recombination of charge carriers at surface defects[162]: the measurement

of doping at the surface and especially of the surface built-in potential at the junction measured with SPEM is therefore an important quantity to understand - and further improve - the efficiency of a solar cell. More interestingly, the surface potential drop and the depletion zone width can be monitored during the application of forward and backwards biases.

Rigid shifts in XPS core levels can be due to the presence of a potential at the surface (Section 4.1.2). In general, neglecting for now surface effects, doping raises a potential equal to $E_f - E_i$, where E_f is the Fermi level of the doped semiconductor and E_i is the Fermi level of the corresponding intrinsic (i.e. undoped) semiconductor. If one considers a *pn* junction, the Fermi levels E_f of p and n are aligned at equilibrium (Figure 4.13a), causing the potential to vary across the junction and bending the band edges and the core levels. One should therefore expect a rigid shift of the core level peaks from lower to higher binding energies when probing, respectively, the p and n doped parts (Figure 4.13c).

However, XPS has a limited penetration depth, and only the core level rigid shifts at the surface are probed. The potential at the surface can actually differ substantially from the bulk due to surface states[163-164] and defects causing band bending (Figure 4.13b). In nanostructures with large surface/bulk ratios such as NWs, even the entire device performance can be affected by surface band bending[165-166].

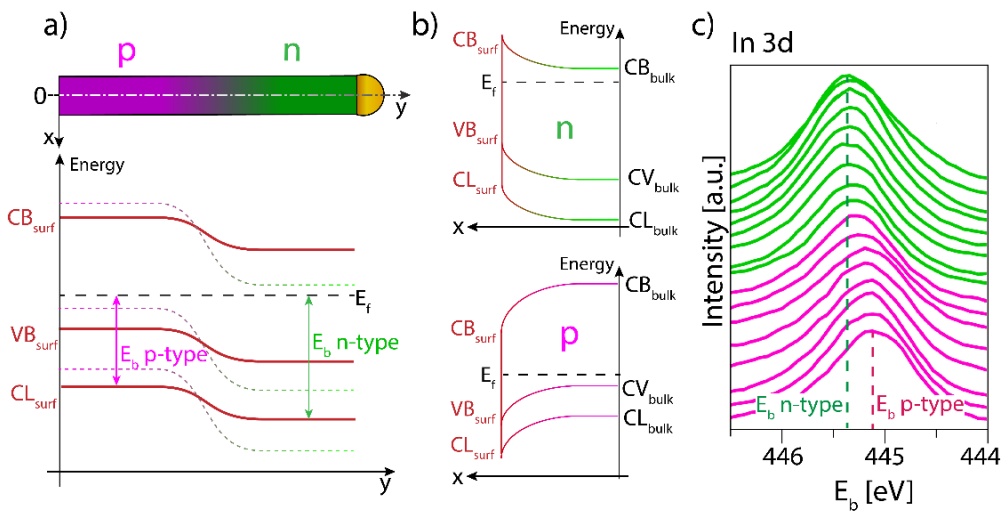

Figure 4.13: a) Axial *pn* junction NW: axial band bending and built-in potential at the surface (red full lines) is less compared to the bulk (dashed lines). b) Radial band bending at *p* and *n* type surfaces caused by surface states. c) Exemplification of XPS core level shift due to surface potential and doping. [tile *c* is adapted from Paper IV]

It is important to point out that also the exposure to X-rays can affect the band bending of semiconductors[167]. Soft X-rays can induce a surface photovoltaic effect, increasing the number of excess carriers by exciting electrons across the band gap. This excess of electron-hole pairs is redistributed in the space charge region of the surface, generally reducing the band bending.

This phenomenon (that may also induce a photocurrent when exciting the depletion region of the *pn* junction) is called surface photovoltage (SPV) and its entity depends also on the X-ray flux[168]. These considerations explain why in general one can expect a different built-in surface potential across the *pn* junction, compared to electric measurements in the dark or in the bulk (Figure 4.13a).

The experimental setup is arranged to perform *operando* measurements: the two ends of the InP NW are in contact with two Au pads separated by a trench[169], so that an external voltage bias can be supplied across the NW (Figure 4.14a). This setup enables to assess not only the *pn* junction potential drop, but also its response to an external electric field by applying a bias to one of the metallic pads, while the other is grounded.

Images of the NW with chemical contrast were obtained by defining a proper energy range around the core levels of interest (Figure 4.14b). The Au 4f map highlights the pads, and the shadow effect of the NW is visible.

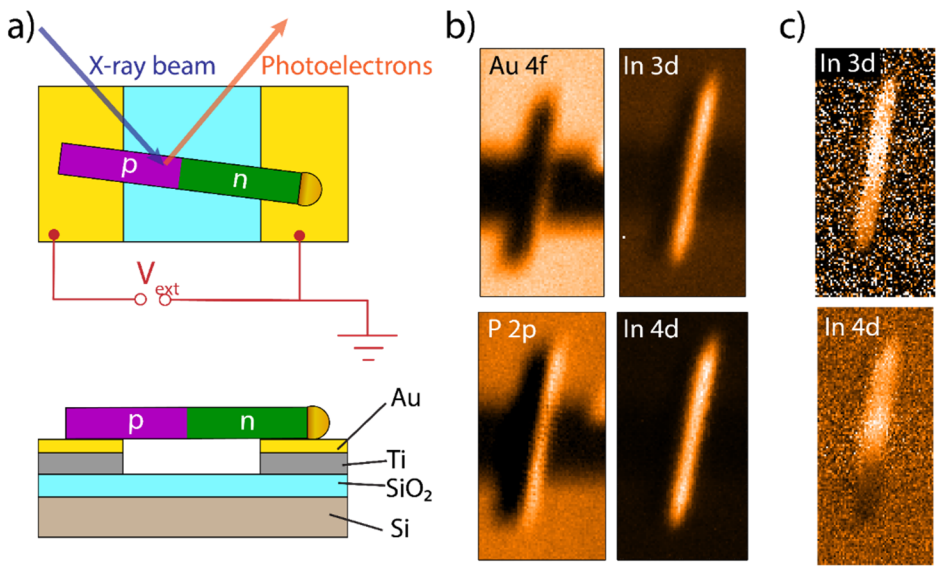

Figure 4.14: a) Experimental setup for the *operando* SPEM experiment. The Au pads contact the NW only at the two ends. b) SPEM images of Au 4f, P 2p, In 3d, and In 4d core levels. The Au 4f core levels put in evidence the pads, the P 2p, In 3d and In 4d show the NW. The image sizes are 2x4 μm^2. c) In 3d and In 4d maps after subtraction of the background and selection of proper binding energy range: the surface potential drop due to the *pn* junction is visible. [Adapted from Paper IV]

The P 2p, In 3d, and In 4d core levels put in evidence the NW. The shadow on the left of the NW is due to the NW itself and to the shallow angle (30°) of the EEA in respect to the surface. The Au pad is visible in the P 2p and In 3d maps and this is because the Au 4f electrons are included in the background, which is not the case for the In 4d map, which binding energy is below the Au 4f edge.

By selecting and summing the signal intensity only for specific channel subranges, one can also define the highest image contrast to the binding energy of either the *p* or the *n* doped segment and thereby map the local position of the *pn* junction (Fig. 4.14c).

SPEM images give an overview on the sample but the low energy resolution and low counting statistics make quantitative estimation of the binding energy shift challenging. This information can be better retrieved by operating SPEM in micro-XPS mode and taking a set of core level spectra along the NW (Figure 4.15a) to map the binding energy positions of the peaks.

When an external voltage V_{ext} is introduced to the *p* doped end of the NW, the Fermi level E_{fp} and the whole band structure of the *p* side is rigidly shifted by the quantity eV_{ext}, where e is the electron charge (Figure 4.15b). The analyzer is grounded together with the *n* side of the NW, and consequently they have the same Fermi level (E_{fn}), which does not change in position. According to equation 4.1, the binding energy is calculated in respect to the Fermi level of sample and analyzer, therefore the binding energy of the *p* doped segment is reduced/increased by the amount $eV_{ext} = E_{fp}\text{-}E_{fn}$; as a consequence, the binding energy difference ΔE between the *p* and *n* doped segments will be given by the sum of the built-in potential and eV_{ext}; this quantity can be retrieved after fitting the positions of the In 3d peaks along the NW (Figure 4.15c). It is necessary to remark that part of the voltage drop takes place at the contacts of the NW: this is the reason why the positions of the peaks for the whole NW are also rigidly shifted when a bias is applied (Figure 4.15c), but this effect does not affect the value of ΔE (Figure 4.15d).

One of the major outcomes from this experiment is the mapping of the surface potential drop along the NW under different operative conditions (Figure 4.15d). The contribution to the potential drop ΔE due to the built-in potential can be distinguished from the one due to the external bias. Moreover, one can measure how the width of the space charge region, i.e. the transition region between *p* and *n* doped segments, changes under the applied bias, which is important for optimizing charge collection in solar cells.

It was mentioned that the exposure to X-rays can induce a SPV that reduces the band bending at the surface. While the entity of this effect on the respectively *n* and *p* doped sections remains unknown in this experimental configuration, its contribution is considered to be the same when performing the micro-XPS measurements at different voltages. Thus, it is supposed to affect the entity of the surface built-in potential, but not its change upon forward or backward bias. In fact,

the X-ray flux and the probed positions on the NW are the same for all three cases (Figure 4.15a), which makes the *operando* measurements still robust and comparable between each other.

Another interesting result is that a surface potential drop is observed not only across the *pn* junction, but unexpectedly also along the *p* doped region (Figure 4.15d), even if no bias is applied: this trend has been attributed to a gradient in the distribution of *p* type dopants (Zn) at the surface, which could be due to diffusion or inefficient incorporation of Zn.

The SPEM results of **Paper IV** show that the NW pn junction characteristics at the surface can differ quite substantially from the bulk and this difference can be quantified, which can be potentially useful in assessing the density of surface defects and the effectiveness of passivation. Furthermore, the results are also relevant because for the first time the surface potential drop across a NW has been studied in operando conditions with SPEM, demonstrating the viability of a novel characterization method. The method and the results are robust, since they are also comparable with other well-assessed techniques used in **Paper IV**, i.e. Kelvin probe force microscopy[170] and scanning tunneling spectroscopy.

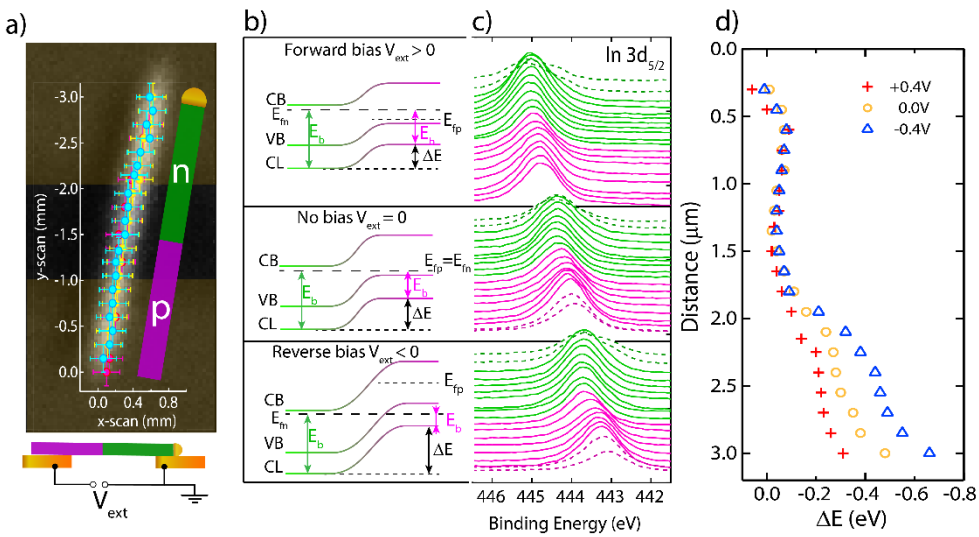

Figure 4.15: a) Position of micro-XPS spectra (yellow: V_{ext}=0, blue: V_{ext}>0, pink: V_{ext}<0) on the NW (SPEM image of the In 3d core level). The bars indicate the size of the X-ray probe (ca. 150x150 nm^2). The *n* part is grounded and V_{ext} is applied to the *p* part. b) Band diagram sketch for the different operating conditions. VB and CB are the valence and conduction band edges, respectively, and CL is a generic core level. E_{fn} and E_{fp} are the Fermi levels for the *n* and *p* parts, respectively and V_{ext} shifts E_{fp}. ΔE is the energy difference between the binding energies (E_b) of the *p* and *n* parts. c) In 3d core level peaks along the NW. d) Potential drop along the NW for different V_{ext} applied to the NW. [Adapted from Paper IV]

5. Nanofocused X-ray fluorescence

It has been mentioned that InP and $Ga_xIn_{1-x}P$ NWs are relevant materials for photovoltaic applications[29, 171], for which doping evaluation is of primary importance. Here, a different and novel approach to assess doping in these nanostructures is presented, that is nanofocused X-ray fluorescence microscopy.

A precise chemical mapping which includes also dopant detection is important not only to fulfil doping specifications for the *pn* junction (or *p-i-n*, where *i* indicates a non-intentionally doped segment), but also because *in situ* addition of dopants can influence the whole NW growth, and the dopants incorporation in the NW itself is not trivial[172].

The study, which is reported in detail in **Paper V**, is focused on Zn as a *p* type dopant, since this material is typically used for InP solar cells[161], and it has been shown that it can strongly affect $Ga_xIn_{1-x}P$ NWs growth dynamics[173] and even the crystal structure[46], influencing therefore the final device performance.

A complete discussion of X-ray fluorescence (XRF) is beyond the aim of this dissertation and the interested reader can be readdressed to more detailed literature, e.g. reference[174] and following. Here I introduce with a phenomenological approach the most relevant concepts in XRF that are needed to interpret the data presented in **Paper V**.

5.1. Quantification in X-ray fluorescence

X-ray fluorescence indicates both the physical process studied as well as the technique (that technically is called X-ray fluorescence spectrometry). The energy of a XRF peak (E_{XRF}) is characteristic of a given transition of a given atomic species (see chapter 3) and the goal of XRF spectrometry is therefore to do a quantitative elemental analysis. The quantification can be done by calibration with proper standards or by fitting the XRF spectra via fundamental parameters[175]. A neat separation between the two methods does not exist, since often *a priori* information from the sample (like in case of **Paper V**) and from the experimental setup is needed to obtain a successful quantification. Hereby, an analytical simplified explanation of quantification in XRF is presented. The theoretical details for quantification methods can be found in references [174, 176-177].

The discussion is limited to the case in which the XRF excitation source is a photon[IX]. X-ray fluorescence is a relaxation process following the absorption of an X-ray photon by a core level electron: the necessary condition for XRF is therefore a photon absorption event and the ionization of an inner shell.

Thereby, the X-ray absorption cross section depends on the excitation energy E_0 and in general decreases[99] as E_0^{-3}. However, abrupt increases in absorption cross sections are present at specific energy *edges*, corresponding to the photoionization energies for a given atomic shell of a given element. During an experiment, it is important to choose an X-ray energy higher than the absorption edge involving the transition of the element of interest.

X-ray fluorescence is a radiative transition involving an electron from one of the outer shells filling the available state in the inner ionized shell. For example, if we consider that a photon is absorbed by an electron in the K-shell, the relaxation process involves an electron from one of the outer shells (L, M, N,… shells). Consequently, the fluorescence spectrum of a K shell is generally composed of multiple lines[X] (Figure 5.1a). However, the transition probability is not the same for all the lines of the K series: for example, the transition from L to K is more probable than the transition from M to K. It is also important to remember that XRF is in competition with the non-radiative Auger transition (see Chapter 3.1): the probability that a vacancy in a shell is filled by a fluorescence transition rather than an Auger process is called fluorescence yield (Figure 5.1b). For example, given a certain element *i*, the K shell fluorescence yield[178] is defined as the ratio of the characteristic X-ray photons ($I_{i,K}$) over the number of vacancies ($n_{i,K}$) in the K cell: $\omega_{i,K} = \frac{I_{i,K}}{n_{i,K}}$. The definition holds strictly for a K-shell, whereas the higher principal energy levels (L, M,…) are split in multiple sub-shells and an average value for the yield is usually provided[179].

[IX] The excitation source for ionization of an inner core shell can also be an electron beam, as it happens for energy dispersive X-ray spectroscopy (EDS), mentioned also later.

[X] in Figure 5.1 it is used the Siegbahn notation. However, even if still widely used in the spectroscopy community, this notation is not systematic and the more intuitive IUPAC notation is sometimes preferred, since it points out directly the shells involved. For example, the $K\alpha_1$ transition in the Siegbahn notation becomes the KL3 transition in the IUPAC notation.

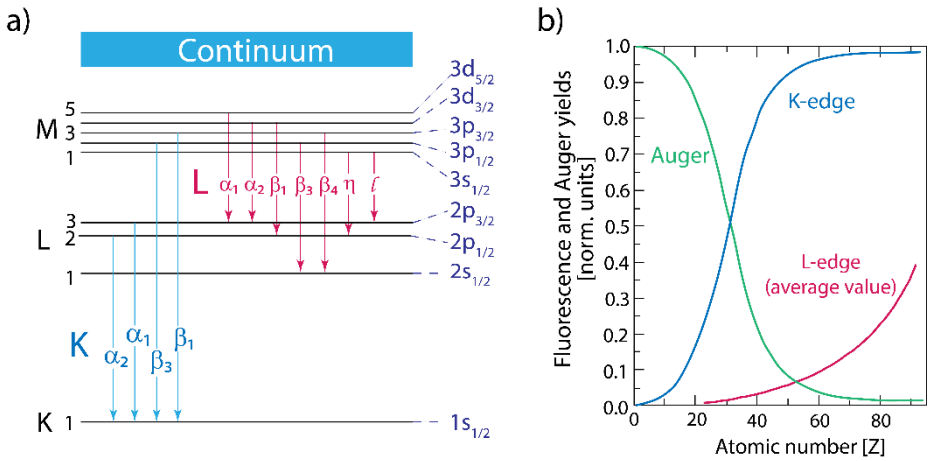

Figure 5.1: a) Allowed X-ray fluorescence transitions involving the K, L, and M shells. The orbital notation is given on the right of the shells. The XRF transitions are represented with arrows and the Siegbahn notation is used. Not all the combinations of subshells allow transitions, due to selection rules. Some transitions, like L-*l*, are very weak. b) Auger and XRF (for the K and L transitions) normalized yields. [partially adapted from [101]]

The goal of an XRF experiment is therefore to relate the intensity of the fluorescence lines of a given *i*-th element to its concentration, or, relatively to the sample, to its mass fraction C_i. The following discussion is dedicated to understand this relationship.

First, one must consider the necessary interaction of X-rays with matter: the deeper the X-ray penetrates into the sample, the higher is the probability of interaction with the electrons: it can be demonstrated that the attenuation of the X-rays in the sample follows a Lambert-Beer law:

$$I_t = I_0 e^{-\mu(E_0)\rho d}$$

where I_t is the transmitted intensity of the beam, I_0 is the initial intensity of the beam, $\mu(E_0)$ is the mass attenuation coefficient which is proportional to the absorption cross section, ρ is the density of the sample and d is the thickness of the sample. In case of a multi-elemental material (as it is in the case of **Paper V**), the mass attenuation coefficient is a weighted average of the individual mass attenuation coefficients of all the elements $\mu_i(E_0)$ over their mass fractions C_i:

$\mu(E_0) = \sum_i C_i \mu_i(E_0)$. One can now find[176, 180] an analytical form for the infinitesimal detected XRF intensity dI at energy E_{XRF}, coming from an infinitesimal thickness dx of the sample at a depth x as a concatenation of five events (Figure 5.2):

$$dI(E_{XRF}) = I_0\, exp\left(-\frac{\mu(E_0)\rho x}{sin\,\psi_1}\right)\cdot\frac{C_i\tau_{i,K}(E_0)\rho}{sin\,\psi_1}dx\cdot\omega_{i,K}R_{i,K}(E_{XRF})\cdot$$
$$\cdot\, exp\left(-\frac{\mu(E_{XRF})\rho x}{sin\,\psi_2}\right)\cdot\frac{d\Omega}{4\pi}\epsilon_D(E_{XRF},\Omega) \qquad (5.1)$$

The first term represents the rate of the photons at the depth x which have not been absorbed in the path $\frac{x}{sin\psi_1}$, with ψ_1 the incidence angle. The second term instead, represents the probability that a vacancy is created ($\tau_{i,K}$ is the photoelectric cross section in the K shell of the i-element) within the infinitesimal thickness dx. The third step represents the probability of the emission of the fluorescence line: $\omega_{i,K}$ is the fluorescence yield and $R_{i,K}(E_{XRF})$ takes into account the ratio of a specific line compared to the others of the K-series. The fourth term[XI] shows the rate of the XRF photons which have not been absorbed in the path $\frac{x}{sin\psi_2}$, with ψ_2 the exit angle defined by the detector position. Finally, a fifth contribution is related to the detection efficiency of the detector ϵ_D in the infinitesimal solid angle $d\Omega$, which depends also on the XRF energy E_{XRF}.

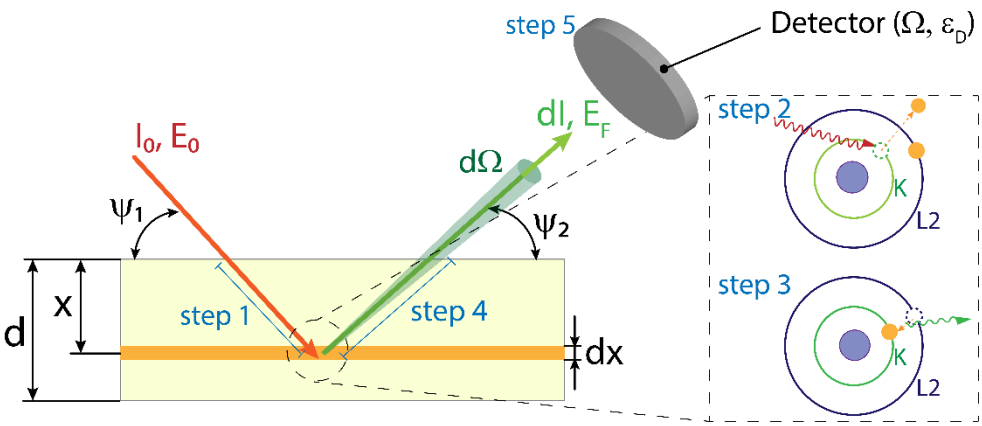

Figure 5.2: Detection of an XRF signal requires a combination of several steps: the incoming beam of energy E_0 and intensity I_0 is partially absorbed before reaching the generic slice of interaction with thickness *dx (step 1)*. The X-ray needs to be absorbed (*step 2*) and the relaxation process needs to be fluorescence (*step 3*) in order to get a XRF signal. The XRF signal of energy E_F and differential intensity *dI* is attenuated when exiting the sample (*step 4*) and is finally detected (*step 5*). [Inspired from [181]]

[XI] Also the path in air between the sample and the detector contributes to the attenuation of the intensity of the XRF beam, not considered here for sake of simplicity.

One can now integrate eq. 5.1 over the sample thickness *d* and the solid angle Ω. By using the parallel beam approximation for the XRF radiation (which is acceptable considering the small size of the beam and the sample-detector distance), ϵ_D is not a function of the solid angle and the relation 5.1 can be integrated and simplified as:

$$I(E_{XRF}) = \frac{I_0 C_i \omega_{i,K} R_{i,K}(E_{XRF}) \tau_{i,K}}{\mu(E_0) + \mu(E_{XRF}) \frac{\sin\psi_1}{\sin\psi_2}} \cdot \left\{1 - \exp\left[-\left(\frac{\mu(E_0)}{\sin\psi_1} + \frac{\mu(E_{XRF})}{\sin\psi_2}\right)\rho d\right]\right\} \frac{\Omega}{4\pi} \epsilon_D(E_{XRF}) \quad (5.2)$$

It is worth noting that the peak intensity for a given transition of a given element does not depend only on the concentration of the element itself but also on the concentration of the other elements in the matrix - which is in general unknown – through the term μ.

These *matrix effects* are related to the absorption and emission of the X-rays by all the species in the sample, and they are less dominant when the thickness of the sample *d* is reduced. For small values of *d*, one can approximate the exponential dependence on *d* in equation 5.2 with a linear one, resulting in:

$$I(E_{XRF}) = \frac{I_0 C_i \omega_{i,K} R_{i,K}(E_{XRF}) \tau_{i,K} \rho d}{\sin\psi_1} \frac{\Omega}{4\pi} \epsilon_D(E_{XRF}) \quad (5.3)$$

where there is no dependence on the mass attenuation coefficient.

This fact is important for the case studied in this thesis, since the thickness of a NW (ca. 180 nm) is negligible compared to the absorption length of the matrix (e.g. for InP, the attenuation length $\mu_l(E) = \mu(E)\rho$ at 10.4 keV is about 14 µm [182]).

From this simplified phenomenological description, one can deduce two important facts, that are generally valid for all XRF experiments: i) the intensity of an XRF peak is not only a function of the concentration of the element and of the cross section of the whole photoelectron process, but depends also on the interaction with the whole experimental ensemble (e.g. matrix effects, air absorption, etc.). ii) some complementary information of the experimental setup and of the sample is generally needed to obtain quantitative information.

Moreover, even if the influence of the matrix is limited like in our case, the problem cannot be solved easily in a closed analytic form. One of the biggest complications arises from secondary excitation: we assumed in equation 5.1 that the vacancy in the K-shell is generated by the absorption of the primary beam I_0 with a probability $\tau_{i,K}$. However, the ionization can also be caused by a sufficiently energetic characteristic XRF photon with energy E_F. As a consequence, the detected intensity $I(E_{XRF})$ can be enhanced or depressed by secondary (or even tertiary) emission. For this reason, an iterative fitting procedure in which the sample matrix is refined is generally needed.

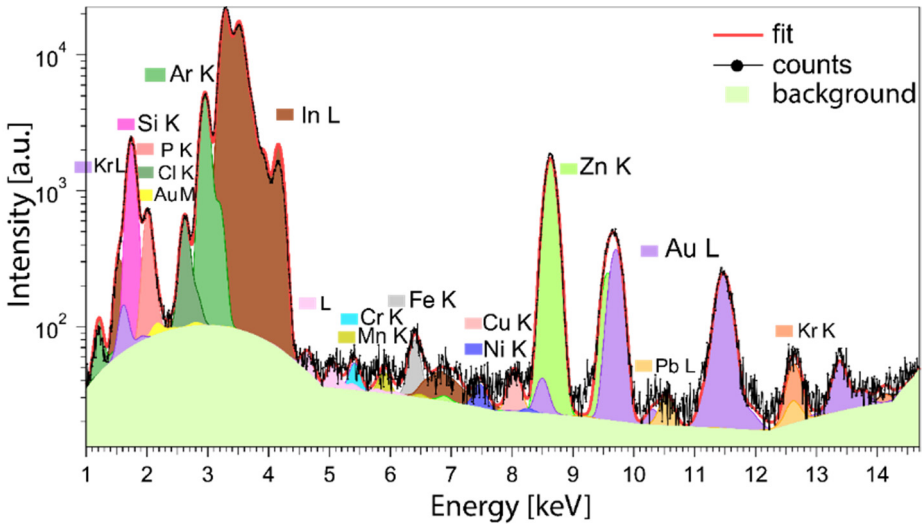

Figure 5.3: XRF spectrum of a Zn doped InP NW, in a spot close to the Au seed. The fluorescence lines for Zn and Au are clearly visible. The low intensity of the K-lines of P is due to the absorption effect of air. The scattering peaks are not within the energy range of this graph.

In this thesis, the PyMCA software[176] has been used for modelling the XRF spectra, taking into account these effects and fitting it to the experimental data. A XRF spectrum acquired close to the Au seed of an InP NW can be observed in Figure 5.3.

The lines are fitted with a Gaussian function and the broadening is mainly due to the instrumental function of the detector. Other effects that are taken into account in the model are the background, the X-ray elastic and inelastic scattering peaks and the detector artefacts (like e.g. escape and pile up peaks[178]).

Nanofocused X-ray fluorescence: instrumentation

It has been shown that XRF can provide a quick and quantitative chemical information, and it has been used routinely in this fashion for over a century by both academia and industry, but with low spatial resolution (usually in the sub-mm range).

A novel approach to XRF useful for nanoscience is to perform X-ray fluorescence microscopy (nano-XRF) using a nanofocused synchrotron X-ray source as a probe. An elemental mapping with high spatial resolution can be obtained by scanning the sample through the nanofocused beam, with the result that for each pixel of the image a full XRF spectrum is collected.

The X-ray fluorescence microscopy study presented in **Paper V** has been performed at the ID16B beamline[183] of the European Synchrotron Radiation Facility (ESRF, Grenoble, France). The use of synchrotron radiation can increase the performance

of XRF microscopy, since the high brilliance compared to a standard laboratory X-ray tube can compensate for the optical losses related to focusing and monochromatization, leaving a photon flux at the sample of 10^9-10^{13} photons/s/μm^2. The low emittance of synchrotron radiation is also advantageous in the focusing of the X-ray probe spot size.

Finally, it is important to point out that local chemical mapping based on characteristic XRF can be routinely done with energy dispersive X-ray spectroscopy (EDS), which is readily available in scanning electron microscopes (SEMs). The EDS working principle is based on probing the sample with the electron beam of a SEM setup, and measuring the characteristic X-rays. In EDS, the inelastic collisions of the electrons used as probe cause bremsstrahlung radiation, which adds to the characteristics X-rays and can prevent the detection of elements with low concentrations. This effect is not present when using synchrotron radiation as primary source (Figure 5.4b).

The focusing of the hard X-ray beam can be done with diffractive, refractive and reflective optical elements. In the case shown here, the source has been focused with a couple of perpendicular hard X-ray mirrors called Kirkpatrik-Baez (K-B) mirrors.

These are placed at a grazing incidence with respect to the X-ray source in order to fulfill the conditions for external total reflection. These optics suffer less optical losses compared to diffractive and refractive optics, but high precision in the surface roughness and in their alignment has to be taken into account. In the case of study of **Paper V**, the focused beam had a spot size of ca. 50 nm^2, but new design solutions have shown[103] the possibility of obtaining spot sizes of 10 nm^2.

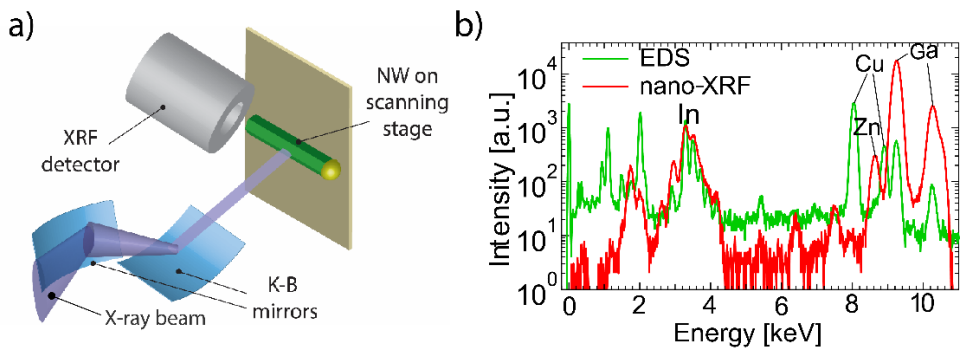

Figure 5.4: a) XRF microscopy setup: The synchrotron beam is focused by the K-B mirrors and the sample (a NW) is scanned under the beam. The signal is acquired with large area detectors. b) Comparison of XRF spectra taken with EDS and XRF on similar positions along a $Ga_xIn_{1-x}P$ NW. The Zn Kα lines (at ca. 8.67 keV) are not visible in the EDS due to the bremsstrahlung. The lines at lower energy are more intense for EDS due to the much lower air absorption (the EDS is done in high vacuum). [Adapted from Paper V].

Similarly to SPEM, the spatial resolution in nano-XRF is therefore determined by the beam spot size and a precise movement of the sample under the beam is accomplished by the piezoelectric motors of the sample stage (Figure 5.4a).

A fast reaction time of the detector is an important requirement in X-ray fluorescence microscopy to obtain chemical mapping in reasonable time, minimizing beam damage and sample drift artefacts. Energy dispersive detectors rely on electron-hole pair generation induced by X-ray photons and can be very fast in performing spectrometry, since they can acquire and discern different photon energies at the same time.

5.2. Nanofocused X-ray fluorescence: a tool for doping assessment in nanowires

Controlled incorporation of dopant atoms is crucial already for the functioning of traditional (bulk) devices, and even more in nanostructures. Dopant characterization in nanowires can be particularly challenging since good sub-µm spatial resolution is required together with a sufficient detection range between 10^{17}-10^{20} atoms/cm^{-3}, which is the doping concentration interval in which most devices work[7]. In **Paper V** it is shown that XRF microscopy is a valuable tool for doping evaluation of III-V NWs, with a spatial resolution of about 50 nm. An important part of this study is the systematic evaluation of the detection limits of the Zn dopant, which were demonstrated to be about 7 parts per million (i.e. 2.8×10^{17} atoms/cm^3). Provided that spatial resolution and detection limits are now known, an interesting question is if these values are satisfactory compared to other viable techniques and if it is worthwhile to use XRF microscopy for NW doping assessment.

Detailed reviews about these methods to evaluate doping in NWs are provided in refs. [9, 184]. Here I mention only two of them, which are easily comparable in resolution and/or detection limits to what can be obtained with XRF microscopy, that are atom probe tomography (APT)[185-186] and EDS. APT relies on the progressive ablation of the sample with a pulsed laser source and the detection of the species with a time of flight detector. A tomographic reconstruction of the sample can then be done with sub-nanometer resolution and parts per billion detection limits. The price to pay for this performance are the difficult sample preparation, the not trivial reconstruction process and the fact that the technique is destructive. When it comes to the EDS, this technique can have spatial resolution in the range of 10 nm, but the detection limits are about 0.1%, which in general are not sufficient to detect dopants. XRF microscopy has therefore a worse spatial resolution compared to EDS and APT but with detection limits in between. A direct comparison between EDS and nano-XRF line scan measurements of an equivalent NW can be found in Figure 5.5.

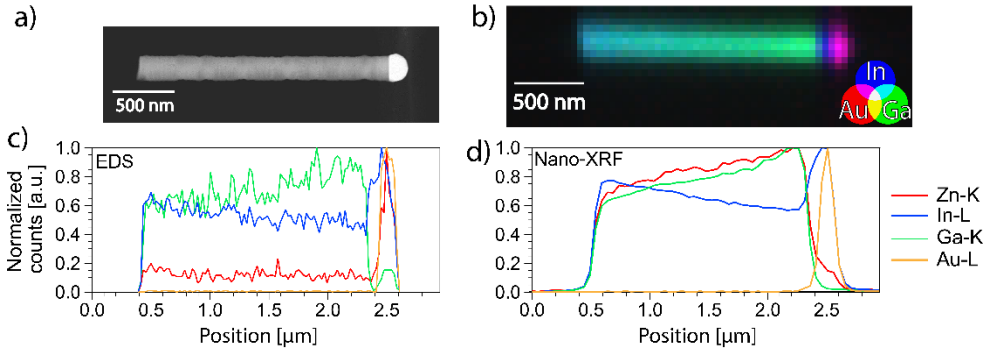

Figure 5.5: a) SEM image of a $Ga_xIn_{1-x}P$ NW equivalent to the one measured with nano-XRF. b) Nano-XRF elemental map of a $Ga_xIn_{1-x}P$ NW. In this false color RGB map, the red channel is proportional to the Au-M line normalized intensity, the blue to the In-L line and the green to the Ga-K line normalized intensities. c) EDS elemental map along the NW (normalized counts). The Zn signal is not visible and there is a remarkable noise. d) Nano-XRF map along the NW (normalized counts): Zn is detectable and the Ga-Zn trend is evident. [Adapted from Paper V]

The advantages of XRF microscopy are therefore related to the detection limits, the flexibility of the operational setup and minimal sample preparation (*operando* measurements on NW devices have been recently demonstrated[187]) and to the robust data analysis consistency, without the influence of the artefacts typically present in APT.

One of the most relevant results obtained in **Paper V** regards the Zn dopant incorporation in a ternary $Ga_xIn_{1-x}P$ NW. This information can be useful in shedding light on the complex mechanisms governing the growth of ternary NWs: even if all the precursor molar fractions are kept constant throughout the growth (like in our case), the resulting stoichiometry of the NW may not be homogeneous e.g. due to different diffusion lengths and paths of the species or to different pyrolysis efficiencies[27].

By using nano-XRF it was possible to detect Zn and to show a direct correlation between the Zn and Ga concentration gradients in a nominally homogeneously Zn doped $Ga_xIn_{1-x}P$ NW (Figure 5.6a). A direct and quantitative measurement of Zn incorporated in this ternary NW was not performed before. In the case of a $Ga_xIn_{1-x}P$ NW, the opposite trends of Ga and In along the NW (Figure 5.5d) can be due to the fact that during growth the species reach the Au droplet mainly through surface diffusion (mainly from the substrate), which becomes more ineffective for In compared to Ga the longer the NW gets[33, 188]. From the correlation of Ga and Zn one can speculate that Zn incorporation takes place only at the Ga atomic sites and it is therefore limited by its content in the NW. The quantitative information can give direct feedback to NW growth, for tailoring the molar fractions of the reactants to compensate this gradient.

The control of dopant incorporation can be problematic even in simpler binary systems, like InP NWs. A sharp transition of dopants is often required to have functional *pn* junctions. XRF microscopy revealed (Figure 5.6b and c) that the transition between *p* doped and nominally intrinsic (*i*) regions is not abrupt, but is characterized by a smooth gradient, whose steepness depends on the concentration of Zn (Figure 5.6c). This fact can be attributed[172, 189] to the reservoir effect, i.e. the fact that a certain amount of dopants is stored in solution in the gold particle, even if the dopant precursor source is shut down and therefore this quota gets gradually incorporated in the solid phase. Conversely, switching on the dopant precursor flow does not mean to incorporate them instantaneously, since pyrolysis and diffusion of these species need to take place. Finally, a result potentially very useful to improve device performance is the detection of Zn in the nominally undoped region of the *p-i-n* junction. This was possible due to the excellent detection limits of the technique. A potential origin of this issue can be found in the carry-over effect, which consists in the undesired incorporation of Zn from precursors adsorbed to the walls of the reaction chamber and is a well-known problem in literature[190]. The quantification of this unwanted dopant contribution in the intrinsic segment can be helpful in designing proper purging during the growth processes.

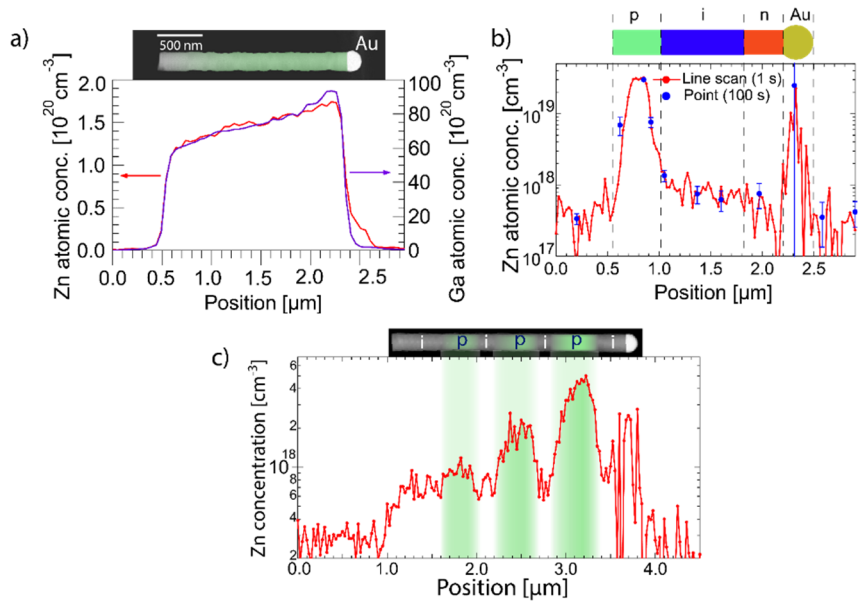

Figure 5.6: a) Zn quantification in a $Ga_xIn_{1-x}P$ NW. There is a constant ratio with the concentration of Ga. A SEM image of the NW is on the top showing its orientation in the nano-XRF line scan. The green overlay on the SEM image suggests the Zn concentration profile along the NW estimated with nano-XRF. b) Zn concentration in a p-i-n InP NW. The blue points show points with long acquisition times (i.e. with better counting statistics), which match the line scan. c) Zn doping in the barcode NW with increasing Zn concentration towards the Au particle (on the right). [Adapted from Paper V].

A final remark about XRF microscopy for doping evaluation: we have seen how SPEM can also provide useful information about doping of similar samples. However, it is important to point out that XRF microscopy and SPEM measure two completely different quantities and can therefore be considered as complementary techniques: SPEM is surface sensitive and measures the electronic effect that the dopants have on the surface potential of the NWs. Conversely, XRF microscopy measures the dopant atomic concentration in the whole NW.

6. Full Field X-ray Diffraction Microscopy

Full field X-ray diffraction microscopy (FFXDM) is a novel technique for studying structural parameters of nanowires. As the name suggests, it combines two different aspects of materials characterization, imaging and X-ray diffraction (XRD), which have been traditionally separated. XRD is a powerful tool to measure periodicities in the range of interatomic distances, and it is therefore sensitive to different crystallographic phases and to lattice strain and tilt. As mentioned in Chapter 2, strain is an important parameter for electronic and optoelectronic devices, since it affects phenomena like charge transport or radiative recombination efficiency in semiconductors. This is even more important in nitride nanostructures, where piezoelectric effects can seriously compromise the device efficiency. FFXDM has been used here (**Papers VI**, **VII**) for studying $In_xGa_{1-x}N$ nano-platelets (or "nano-pyramids"), which are a novel and promising template for LED applications[37].

In order to fully understand capabilities and limits of XRD imaging, it is necessary to introduce some basic concepts of single crystal X-ray diffraction.

6.1. Basics of X-ray diffraction

One possible interaction of matter with X-rays is elastic scattering (see Chapter 3). If the atoms are arranged in a periodic array, the scattered wave will form an interference pattern. A geometrical representation in real space (Figure 6.1a) of XRD can therefore be provided by the well-known Bragg law:

$$n\lambda = 2d_{hkl}sin(\theta_B)$$

where d_{hkl} is the distance between the parallel diffracting planes having the Miller indices (h,k,l), λ is the wavelength, θ_B is the Bragg angle for which the constructive interference condition is fulfilled, and n is a natural number, which takes into account higher diffraction orders.

By defining the reciprocal space lattice, one can find a more general relation considering the symmetry of the crystal, rather than a naïve visualization of atomic

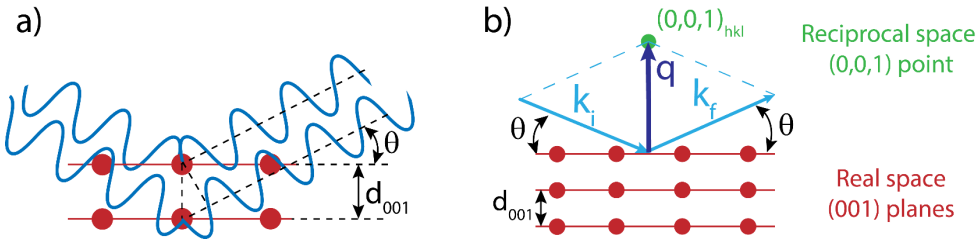

Figure 6.1: a) Graphical demonstration of Bragg's law: given crystal planes with distance d_{001} and a radiation with wavelength λ, constructive interference is possible only for certain angles θ. b) Diffraction conditions in reciprocal space: the scattering vector $\boldsymbol{q}$ matches with a reciprocal space point (top part of the graph). The bottom part of the graph is in real space and it shows the geometrical construction of the $\boldsymbol{q}$ vector as the difference of the scattered wave and incoming wave vectors $\boldsymbol{k_f}$ and $\boldsymbol{k_i}$, respectively.

planes. Let $\boldsymbol{a_1}$, $\boldsymbol{a_2}$, $\boldsymbol{a_3}$ be the unit vectors forming a basis of the unit cell of the crystal in the real space, the unit vectors $\boldsymbol{b_1}$, $\boldsymbol{b_2}$, $\boldsymbol{b_3}$ forming a basis for the reciprocal space are defined as:

$$\boldsymbol{b_m} = 2\pi \frac{\boldsymbol{a_n} \times \boldsymbol{a_p}}{\boldsymbol{a_m} \cdot (\boldsymbol{a_n} \times \boldsymbol{a_p})}$$

With $m, n, p = 1, 2, 3$. The reciprocal space lattice $\boldsymbol{G}$ can be defined: $\boldsymbol{G} = h\boldsymbol{b_1} + k\boldsymbol{b_2} + l\boldsymbol{b_3}$, where h, k, l are integers corresponding to the Miller indices. Each point of the reciprocal space lattice corresponds to a family of planes in the real space.

One can also define a scattering vector $\boldsymbol{q} = \boldsymbol{k_f} - \boldsymbol{k_i}$, where $\boldsymbol{k_i}$ and $\boldsymbol{k_f}$ are, respectively, the wave vectors of the incoming and scattered X-ray wave.

It can be demonstrated[191] that the conditions for constructive interference are fulfilled whenever: $\boldsymbol{G} = \boldsymbol{q}$, i.e. when the diffraction vector $\boldsymbol{q}$ points to a point of the reciprocal space lattice. A diffraction experiment consists in exploring and mapping the reciprocal space by changing length and direction of the diffraction vector. The most common way to accomplish this, is to scan the incidence angle θ defined in Figure 6.1b.

According to the definition of $\boldsymbol{G}$, the Bragg peaks are expected to be geometrical points in the space at fixed positions[XII]. However, this is not the case – especially for nanostructures – since shape and position of Bragg peaks embed information about the finite size of the crystal domains and about the displacements of the real space lattice points, such as e.g. tilt and strain. Tilt is a rigid rotation of the lattice compared to its reference position (Figure 6.2a) and it corresponds to a rigid rotation of the reciprocal space lattice (Figure 6.2b), but does not affect the length of the corresponding $\boldsymbol{G}$ vector, since the relative lattice spacing is the same. Another case

[XII] In general, this is not true also in case of a perfect infinite crystal, since Bragg peaks are not Dirac delta functions, but have a finite broadening, known as Darwin width.

is homogeneous strain (Figure 6.2c), in which the diffracting planes have a constant, different spacing: the diffraction peak is rigidly translated in the reciprocal space, and the module of the reciprocal space vector ***G*** is also changed. An inhomogeneous lattice strain will instead broaden the diffraction peak (Figure 6.2d). This effect can be intuitively explained as a superposition of diffraction peaks caused by a distribution of differently spaced planes.

It is important to highlight that a different lattice spacing is not necessarily caused by strain. A different chemical composition in an alloy changes, in general, the lattice constant. As we will see later, this consideration is important for our experiment, where $In_xGa_{1-x}N$ pyramids grown on GaN substrate were studied: a gradual change in the In fraction x would create a spread in the Bragg reflection similarly to the one showed in Figure 6.2d.

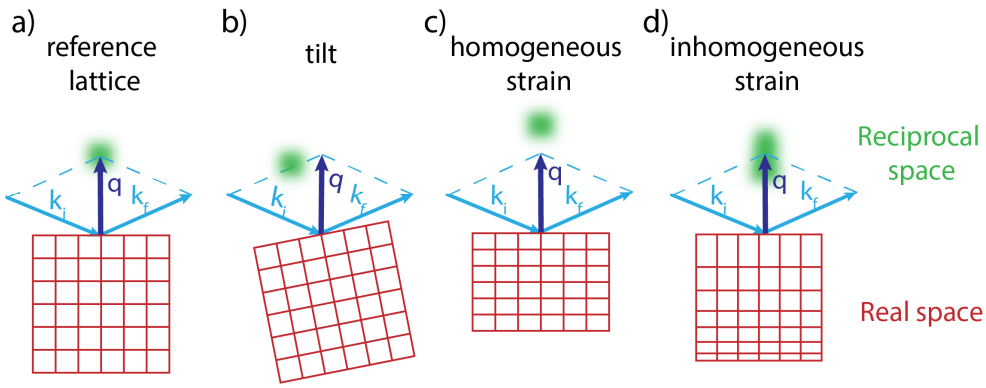

Figure 6.2: a) reference lattice (bottom) and diffracted intensity (top). b) Tilt of lattice causes rotation of diffraction intensity. c) Homogeneous strain causes translation of the diffracted intensity. d) Inhomogeneous strain broadens the diffracted intensity.

6.2. Full field X-ray diffraction microscopy: principle and advantages

In the last years a lot of effort has been put in combining spatial resolution of microscopy with XRD structural information, which can be achieved in different ways. Impressive advances have been obtained with coherent diffraction imaging (CDI)[192], where the sample is irradiated under a coherent X-ray probe and the phase of the diffracted intensity is retrieved to reconstruct the object in real space with sub-nanometer resolution. Another approach is the scanning diffraction microscopy (or "K-mapping"), where the sample is scanned under a nano X-ray probe (similarly to what has been done in this thesis with nano-XRF) and the reciprocal space is locally mapped[193-194], with resolution limited by the beam spot size.

In this dissertation FFXDM has been used, that differs from the previous techniques since it is a full field approach with a large field of view (FoV) of ca. 230×230 μm^2 and short acquisition times (typically few seconds per image).

In FFXDM the X-ray probe is monochromatized and focused on the sample, and then the diffracted intensity is collected by imaging X-ray lenses and projected in far field, where a real space image is acquired by a 2D detector (Figure 6.3).

The magnification of the illuminated area is realized with a set of compound refractive lenses (CRLs), and actually the lack of advanced technology to manufacture CRLs prevented a full development of FFXDM until recent times[195]. This optics consists in an array of concave lenses focusing the X-rays. The shape of the lenses is due to the fact that the refraction index n of X-rays is negative and, according to the Snell's law, focusing can only be obtained with a concave lens surface.

A fundamental limit to the spatial resolution d_l of FFXDM is the numerical aperture (NA) of the objective lenses ($NA \cong 5 \cdot 10^{-4}$), and one can estimate d_l as: $d_l = \frac{0.61\lambda}{NA}$, which is around 100 nm (the actual spatial resolution is in the order of 200 nm, due to aberrations and vibrations of the experimental setup).

Interestingly, a small NA of CRLs is beneficial for the angular resolution of FFXDM, resulting in a better image contrast. The angular resolution is related[196] to the reciprocal space resolution $\Delta d/d$, i.e. the capability of distinguishing a lattice displacement Δd in respect to a spacing d. In our setup it is in the range of 10^{-4} (similar to other XRD imaging techniques[197]). An important feature of FFXDM is therefore the trade-off between real space and reciprocal space resolution.

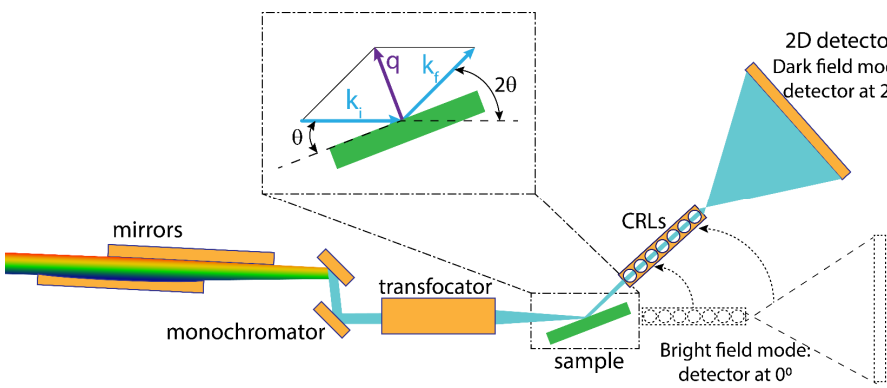

Figure 6.3: Experimental setup for FFXDM. The diffracted intensity is collected by the objective lenses (CRLs) and imaged in far field. Relevant angles are shown in the inset. In the sketch a simplification about the angles notation has been done. The angle between $\boldsymbol{k_f}$ and the sample surface is equal to the Bragg angle θ only if the scattering planes of interest are parallel to the sample surface. In all the other cases, comprising the experiment hereafter, the sample is tilted by an angle ω and the detector by an angle ν. [Inspired from Paper VI]

The detector is placed in far field, at a distance of 6.5 m from the CRL lenses. The magnification of FFXDM is about ×65, as it can be calculated by ray optics, considering that the sample-CRLs distance is 10 cm. Due to the long distance between the sample and the detector, the latter is placed at the end of a vacuum tube (not shown in Figure 6.3) which moves solidly with the detector; this improvement is helpful in reducing absorption of air of the scattering intensity, which may cause rather significant signal losses.

One can notice that the principle of FFXDM is conceptually similar to a dark field transmission electron microscope, a standard technique for studying nanostructures like the $In_xGa_{1-x}N$ pyramids. There are however, several advantages[196, 198]:

- The sample preparation is minimal for FFXDM and thin sample slices are not required. *In situ* and *operando* measurements are also possible.
- By choosing proper Bragg reflections with shallow incidence angle, the signal can be made surface sensitive.
- As mentioned above, the contrast is based on X-ray diffraction and not on absorption and phase contrast, which is advantageous for signal filtering.
- Lattice strain and tilt can be mapped by mapping the reciprocal space.
- The FoV is in the range of hundreds of μm, which is very important to provide statistically relevant information on nanostructured samples. Moreover, a nanoscale contrast mechanism determined by lattice displacement combined to a macroscopic scale FoV is fundamental for studying industrially relevant devices.

Compared to the X-ray diffraction imaging techniques mentioned before, FFXDM cannot compete in terms of spatial resolution, but the acquisition time is much faster in the order of seconds compared to hours needed for CDI or K-mapping[199], and a large number of nano-objects can be simultaneously investigated.

6.3. FFXDM on $In_xGa_{1-x}N$ pyramids for LEDs

6.3.1 $In_xGa_{1-x}N$ LEDs: opportunities and open problems

III-N semiconductors are very promising candidates for LED applications. The light emission efficiency is affected by the amount of defects (e.g. dislocations) and by the quantum confined Stark effect (QCSE), that is intimately related to the strain fields in the material. One of the major sources of unrelaxed strain occurs when interfacing the GaN growth substrates with optically active layers of $In_xGa_{1-x}N$: the latter has a lattice parameter larger than GaN, and the mismatch is worse for larger content of In. Strain and defects arising from strain relaxation are therefore limiting the quality and the width of the $In_xGa_{1-x}N$ active layers.

A novel approach[37] to solve this issue consists in growing GaN nanowires (or "seeds") via SAE, i.e. through the holes of an inert mask placed on the GaN growth substrate. Then, these GaN nanostructures are used as nucleation sites to grow $In_xGa_{1-x}N$ pyramids (Figure 6.4a). There are several advantages by using this approach, which include i) the GaN pyramids have a small footprint and the SAE growth filters out high dislocation densities typical of traditional GaN thin films usually deposited on sapphire or Si substrates. ii) A major content of In can be tolerated compared to bulk $In_xGa_{1-x}N$, since nanostructures can easily relax strain iii) The QCSE is reduced due to the growth of $In_xGa_{1-x}N$ on the inclined semi-polar facets of the GaN seed. The performance of LEDs using this approach is very promising, and light emission in the green and even in the red spectral range has been demonstrated[200].

The $In_xGa_{1-x}N$ pyramids characteristics are strongly dependent on processing parameters, especially the diameter of the openings in the SiN growth mask (O) and the pitch (P), which is the distance between two adjacent openings (Figure 6.4b). The opening size affects mainly the GaN seed shape, that can lead to different pyramid morphologies. Small openings (e.g. 90 nm) favor the formation of complete pyramids (Figure 6.4c), whereas larger openings (e.g. 200 nm) can result in truncated pyramids, depending on the competition of the growth either along the [0001] or the $[10\bar{1}1]$ directions. This is important also from a technological point of view, as confirmed by photoluminescence measurements[37], since these two directions have different In incorporation, and the $(10\bar{1}1)$ facets are more prone to fluctuations in the In content. The pitch instead determines the volume of the nano-pyramids: larger pitches (e.g. 2 μm) mean that the areas around each opening are bigger, or in other terms, that a larger amount of precursor materials can diffuse on the surface of the mask for each nano-pyramid. Also in this case the incorporation of Ga and In can be rather complex, considering their different diffusion lengths.

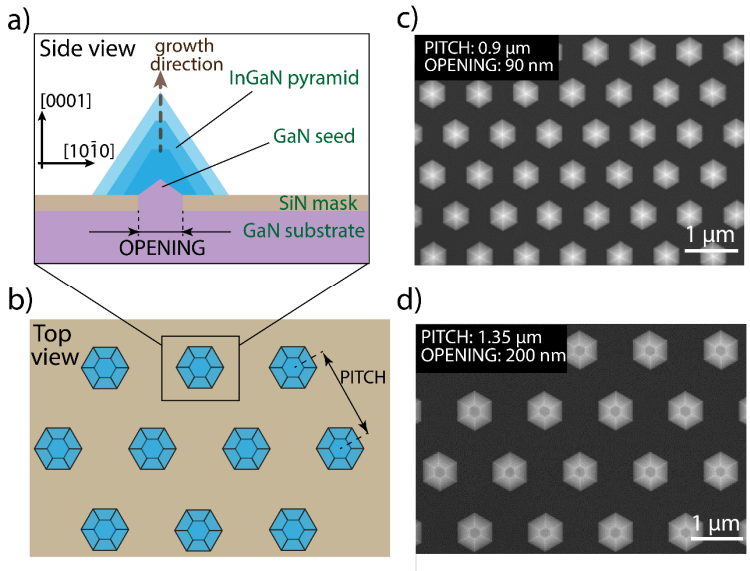

Figure 6.4: Nitride pyramids sample. a)-b): GaN seeds are grown through the openings of the mask and are used as nucleation sites of the for $In_xGa_{1-x}N$ pyramids. Relevant epitaxial crystallographic directions are shown. c)-d): SEM images showing the morphology of the pyramids resulting from different pitch and openings. [Adapted from Paper VII].

These samples have therefore still many open issues: the incorporation of In and Ga species in the nano-pyramids is determined by the interplay of many processing parameters, and the strain relaxation mechanism of these nanostructures is still not completely clear. Different strain relaxation is therefore expected when using different opening and pitch sizes. Moreover, it is also known that SAE overgrowth of GaN can cause tilts above the mask[201]. Another important issue from an industrial point of view is to assess the homogeneity of these characteristics in a nano-pyramids batch produced with the nominal same processing parameters.

6.3.2 FFXDM study of $In_xGa_{1-x}N$ pyramids

FFXDM is an ideal technique to study the lateral distribution of lattice tilt and strain, and the large FoV allows to study a statistically significant number of pyramids in a reasonable time scale and to measure multiple patterned areas at once. Structural information with statistical significance is actually very important from an application point of view, and cannot be easily achieved with CDI, K-mapping or even TEM, since there only a limited number of nanostructures can be characterized.

In a FFXDM experiment the reciprocal space around the Bragg reflection of interest is explored: the length of the scattering vector $\boldsymbol{q}$ is changed by doing a θ-2θ scan, as sketched in Figure 6.5a.

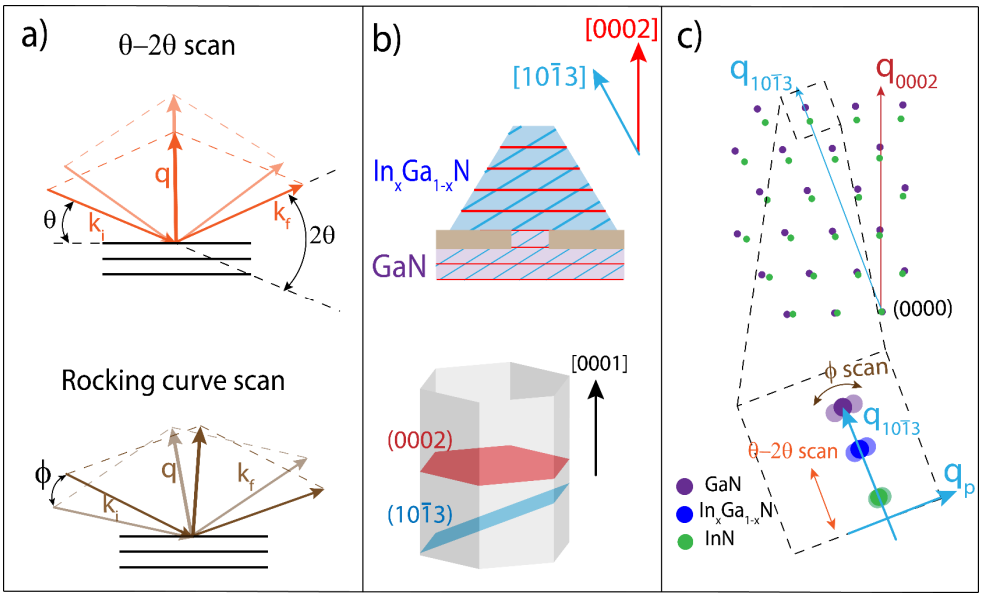

Figure 6.5: a) A θ-2θ scan maps different lattice constants, whereas the rocking curve scan maps mosaicity (i.e. a collection of tilts) of the crystal. b) symmetric (0002) and asymmetric ($10\bar{1}3$) planes. c) Qualitative representation of the probed reciprocal space. Purple dots represent the GaN reciprocal space, green the InN one. In the inset the unstrained positions of the (In,Ga)N reciprocal space lattices are represented. Shadowed areas represent tilt of the unstrained lattice. The inhomogeneous strain case is not represented for sake of simplicity, since depending on its orientation may cause a broadening in both $q_{10\bar{1}3}$ and q_p directions. The labels of the **G** lattice are only indicative, since they are in 3D and not in 2D as represented here. [Adapted from Paper VII]

For each position recorded along the θ-2θ scan, a rocking curve is taken. A rocking curve consists in rotating the reciprocal space around the origin, therefore without changing the length of $\boldsymbol{q}$. From a practical point of view, it consists in tilting the sample by a small angle ϕ (ca. $\pm 0.7°$) in the diffraction plane around a given θ-2θ configuration. For each position of the reciprocal space, a real space image at the detector is taken.

In this experiment the $10\bar{1}3$ diffraction peak has been studied, which is an asymmetric peak. A symmetric peak is instead the 0002, which corresponding planes are parallel to the epitaxial growth direction (Figure 6.5b).

The reason why an asymmetric peak has been chosen is threefold: the geometry of the experiment is advantageous, since these planes require a very shallow incidence angle with the incoming beam (i.e. the angle between the vector $\boldsymbol{k_i}$ and the surface of the sample) of ca. 1.8°, which makes the signal intrinsically surface sensitive, avoiding also depth related artefacts[199]. Conversely, the exit angle is moderately large, avoiding image projection issues at the detector. An important reason to choose a non-symmetric reflection is actually related to the sample structure itself.

The substrate and seed are made of GaN, with a smaller lattice constant (Figure 6.5c) compared to the $In_xGa_{1-x}N$ pyramid on top, and the lattice mismatch may cause strain at the interface. With the symmetric [0002] direction, one would only be able to map the so called in plane strain, i.e. the strain perpendicular to the growth direction, which is supposed to be quite small, considering that most of the strain is radial. The $[10\bar{1}3]$ direction instead, allows to map also the out of plane strain, potentially providing more valuable information.

From the sketch of the reciprocal space map (Figure 6.5c), one can see that it is possible to separate the signal of the $In_xGa_{1-x}N$ pyramids from the GaN: the lattice parameter increases with increasing %In, and the corresponding Bragg peak for the unstrained lattice is supposed to be at intermediate position between the theoretical InN and GaN peaks.

It is important to remember that the diffracted intensity is in general a three dimensional quantity in reciprocal space. With our experiment only a 2D slice of it is explored: the situation presented in (Figure 6.5c) is therefore a simplification and a spread of the signal during a rocking curve scan can therefore be due both to tilt and/or to strain. It is not possible to distinguish quantitatively these two contributions by analyzing only one Bragg reflection and only one tilt direction, but one can still extract valuable information about sample homogeneity.

The spatial configuration determined by the combination of θ-2θ and ϕ angles can be more conveniently expressed with the scattering vector $\boldsymbol{q}$ with the orthogonal components $q_{10\bar{1}3}$ and q_p (Figure 6.5c).

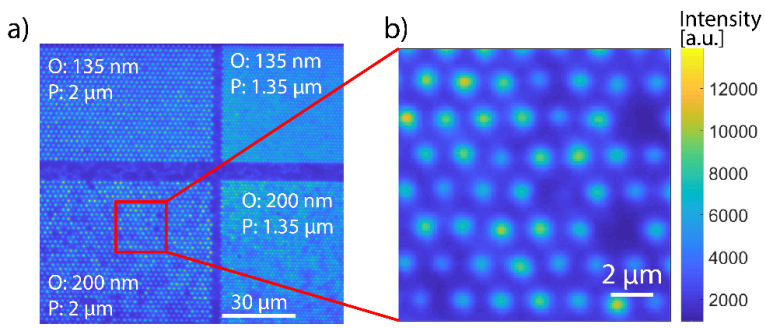

Figure 6.6: a) Real space image of a wide sample area (sum of image frames taken by the detector for all the tested diffraction conditions). The large FoV allows to map four differently patterned areas (i.e. with different openings (O) and pitches (P)) in one run. b) Magnification of a selected area of interest in a). The individual pyramids are visible and can be tracked. [Adapted from Paper VII]

Here $q_{10\bar{1}3}$ corresponds to the positions recorded with the θ-2θ scan and q_p to the ones recorded with the rocking curve. This notation has several advantages, since it can be easily represented in reciprocal space and it is not dependent on the energy of the X-ray beam (which is instead the case for Bragg angles), so that the data can be easily compared with literature.

The detector records a real space image for each value of $\boldsymbol{q}$: the data can be conveniently stored in a four dimensional matrix: $I\left(N_x, N_y, q_{10\bar{1}3}, q_p\right)$, where I is the recorded intensity, N_x and N_y are the number of pixels in the 2D detector, whereas $q_{10\bar{1}3}$ and q_p define the reciprocal space position at which the image was taken. High $q_{10\bar{1}3}$ means sensitivity to the GaN lattice spacing, low $q_{10\bar{1}3}$ means instead mapping the $In_xGa_{1-x}N$ lattice spacing, i.e. the pyramids (Figure 6.5c). The contrast mechanism of each real space image taken at the detector is proportional to the local scattering intensity (Figure 6.6a,b). Each pyramid "shines" when the diffraction conditions are fully fulfilled. By taking the matrix I and fixing a certain $q_{10\bar{1}3}$, one can study the distribution of diffraction intensity out of the $[10\bar{1}3]$ direction by selecting different frames along the rocking curve q_p (Figure 6.7a).

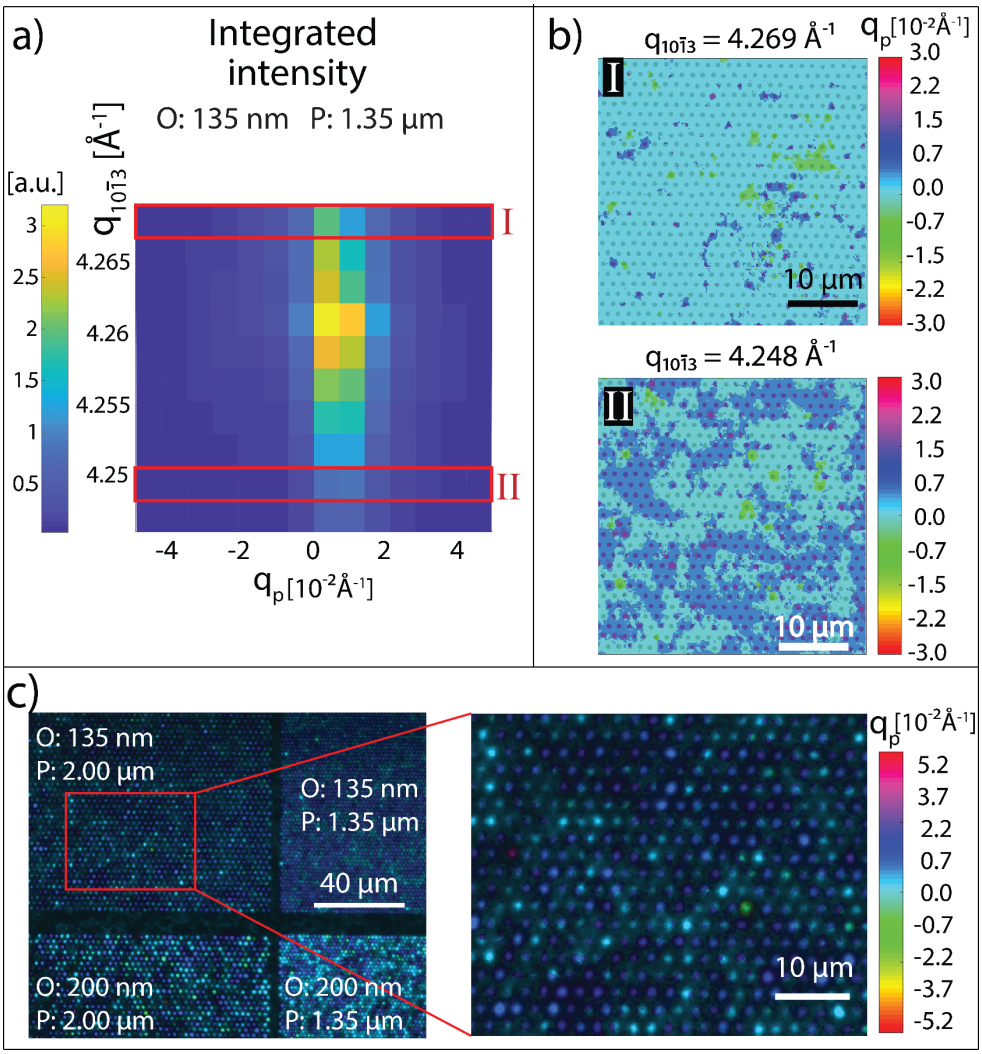

Figure 6.7: a) Reciprocal space map of a large patterned area with opening (O) and pitch (P) as indicated, obtained by summing the intensity for each image and plotting in function of $q_{10\bar{1}3}, q_p$. Higher $q_{10\bar{1}3}$ means that the signal is sensitive to the GaN substrate, lower $q_{10\bar{1}3}$ that is sensitive to the pyramids. The highlighted slices I and II show two rocking curves (I is more sensitive to the lattice spacing of the substrate, II to the one of the pyramids). b) Rotation maps for the rocking curves I and II. The color represents the dominant tilt direction for the selected pixels. The sample area is the same for both tiles and the regular overlay shows the position of the pyramids. c) hue-saturation-brightness (HSB) map: the hue channel is given by the rotation map, the brightness and saturation channel is given by the intensity map: the pyramids and their tilt are put in evidence. [Adapted from Paper VII]

The spread of the signal along the rocking curve q_p is due to inhomogeneity and variations of the lattice spacing that can be actually due to both tilt and strain, that are not separable in the present experiment.

An intuitive way to visualize this lattice variation along the rocking curve is to do a *rotation map* of the sample area of interest: each pixel of the real space image is assigned with the value of q_p for which that pixel showed the maximum intensity along the rocking curve (Figure 6.7b). In other terms, areas with the same color have a similar lattice displacement and show high intensity at the same rocking curve position. It can be noticed how the spread of intensity along the rocking curve is wider for the pyramids (tile II, Figure 6.7b) compared to the substrate (tile I, Figure 6.7b), for which almost a single color is visible.

However, rotation maps give the same intensity weight to all the pixels of the image, and the distinction between mask and pyramids can be challenging. A more realistic visualization of the tilt-strain of the pyramids can be done with a hue-saturation-brightness (HSB) map (Figure 6.7c), in which the hue channel corresponds to the rotation map, the saturation channel is fixed and the brightness one corresponds to the intensity of the images recorded by the detector (Figure 6.6). In this way the pyramids are put in evidence and their color indicates the position along the rocking curve where they showed maximum intensity.

The most interesting result of **Paper VII** is that the distribution of intensity along the rocking curve is strongly dependent on the growth parameters (Figure 6.8), or in other terms that the growth parameters affect the tilt and strain of the individual pyramids.

The best homogeneity of the lattice spacing was obtained for small pitches (0.9 μm) and large openings (200 nm). Smaller pitches should result in higher homogeneity, because short pitch distances compensate for the different diffusion length of In and Ga on the mask. Regarding the openings, if they are large, the corresponding pyramids are characterized by a flat (0001) facet at the top. It is known[202] that the $(10\bar{1}1)$ lateral facets show higher In fluctuations than the (0001) facets. The presence of the more homogeneous (0001) facets in pyramids with larger openings may be a reasonable cause for the higher structural homogeneity (Figure 6.8).

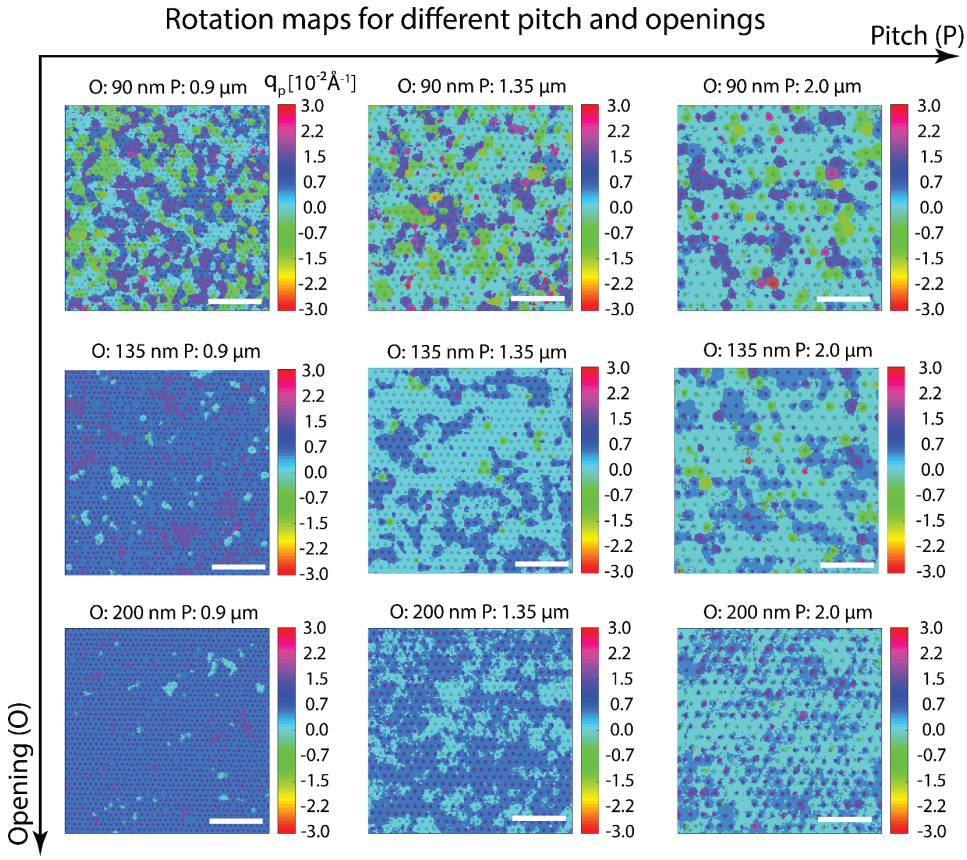

Figure 6.8: Rotation maps for different patterned area (opening and pitch are shown at the top of the tiles). Small pitch and large opening give more homogeneous rotation maps. All the rotation maps are taken at the same $q_{10\bar{1}3}$ for comparison and the scale bar is 10 µm. [adapted from paper VII]

It is worth noting that the information of FFXDM is in line with previous photoluminescence (PL) investigations on the same sample[37]. However, in the case of FFXDM, the information about the quality of the crystal lattice is not given by indirectly measuring optical properties like in PL, but by directly imaging inhomogeneity in crystal lattice spacing. These FFXDM results are also relevant from a practical point of view because they are statistically robust, given the large number of pyramids ($>10^3$) tracked individually. Statistical consistency of the data is of outermost importance when implementing nanostructures from a laboratory device scale into a realistic device. It is necessary to highlight that for getting a complete mapping of tilt and strain, this experiment should be repeated for an additional different Bragg peak (e.g. the 0002).

7. Complementary techniques

Even if powerful and flexible, the synchrotron X-ray approach is not a sufficiently comprehensive tool: its experimental availability is limited and the X-rays themselves determine a certain set of possible probe-sample interactions. Complementary techniques based on specific laboratory equipment are therefore irreplaceable resources. Hereafter I present the lab techniques that I personally performed, i.e. scanning tunneling microscopy and low energy electron diffraction. Other laboratory techniques carried out by collaborators (including e.g. SEM, atomic force microscopy and electrical transport measurements) contributed to the papers presented hereafter, but their explanation is out of the aim of this thesis.

7.1 Scanning Tunneling Microscopy

Scanning tunneling microscopy (STM) is a scanning probe technique which provides atomic resolution and it is based on electron tunneling between a sharp probe (tip) and the sample. Imaging is done by recording the net tunneling current when applying a voltage bias between the sample and the tip and by scanning the latter on the sample (Figure 7.1a). The movement of the tip is operated by piezoelectric motors, providing the necessary precision at the atomic scale.

The interpretation of the image contrast is generally not trivial: the magnitude of the tunneling current is in fact both dependent on the distance between the tip and the sample (i.e. the topography of the sample) and the electronic state of the two tunneling systems themselves, i.e. tip and sample. A short motivation for this statement is provided here, and the interested reader is addressed to references[203-204] for more details.

Electron tunneling can be easily described analytically in one dimension by considering the solution of a time-independent Schrödinger equation for a potential barrier, which models the distance in vacuum between tip and sample. The solution of this equation can be described as a plane oscillatory wave which experiences exponential decay in the barrier. The transmission coefficient across the barrier is proportional to $e^{-\frac{2d}{\hbar}\sqrt{2m(V_b-E)}}$ where d is the barrier width, m is the electron mass, V_b the height of the potential barrier, and E the energy of the electron wave function.

One can notice that the tunneling probability is exponentially dependent on d, i.e. the distance between tip and sample, explaining the extraordinary resolution of the STM in this direction.

Models taking also into account the electronic structure of tip and sample have been established, and the tunneling probability can be derived from the Fermi golden rule. One can find an expression for the tunneling current I with the Bardeen formalism[205-206]:

$$I = \frac{2\pi e}{\hbar} \sum_{i,f} |M_{fi}|^2 \delta(E_{fin} - E_i)\, f_{FD}(E_{fin})[1 - f_{FD}(E_i + eV_0)] \qquad (7.1)$$

where e is the electron charge, M_{fi} is the matrix element, summed over all the possible final f and initial i states, and the Dirac delta ensures the conservation of energy from the initial state in the sample (E_i) to the final state in the tip (E_{fin}). The Fermi-Dirac distribution functions f_{FD} consider the number of electrons available for tunneling in the initial and final states at a given temperature T, when a bias V_0 is applied between the sample and the tip. Tunneling is therefore possible only from full (initial) to empty (final) states and the voltage V_0 is needed to introduce an offset

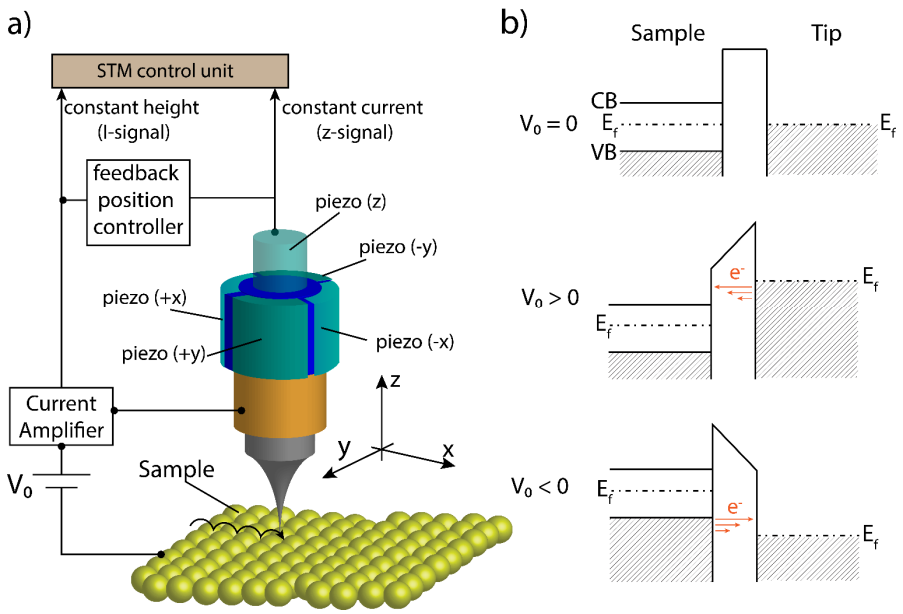

Figure 7.1: a) STM setup: the tip is scanned on the sample surface in the x and y directions with the corresponding piezo-motors and the tunneling current is recorded. The STM can work in constant height or in constant current mode, in the latter case a feedback loop is present to reposition the tip with the piezo-motor (z). b) An STM metallic tip can probe filled (dashed areas) or empty states of a semiconductor sample. On the top no net tunneling current is present, since the system is at equilibrium. If a positive voltage (V_0) is applied on the sample, one probes the empty states of the semiconductor, whereas if a negative bias is applied to the sample, the electrons are tunneling from the filled states of the sample to the tip.

between the Fermi levels of sample and tip, to allow tunneling and to reduce the tunneling barrier height. In an explicit form, the tunneling matrix is described as:

$$M_{fi} = \frac{\hbar^2}{2m} \int_{S_{tip/sample}} (\psi_{sample,i} \nabla \psi^*_{tip,f} - \psi^*_{tip,f} \nabla \psi_{sample,i}) d\boldsymbol{S}$$

where $\psi_{tip,i}$ and $\psi_{sample,f}$ are the wave functions for a generic initial state in the tip and a final state in the sample, respectively, and the integral is calculated over the surface $S_{tip/sample}$ of separation between the sample and the tip.

However, the wave functions embedded in the matrix element are in general unknown: it is useful to develop equation 7.1 in a more manageable way, i.e. in terms of the local density of states (LDOS), that is the distribution of electronic states in energy and space. That provided, a more practical formalism for the tunneling current can be found in the Tersoff-Hamann[206] approach, explicitly expressing the matrix element and considering a tip with a circular apex which center is placed at a distance z_0 from the surface, with a voltage V_0 between the sample and the tip. It can be shown that the current is actually proportional to the local density of states of the sample (at the Fermi energy E_f) at the tip position: $I \propto V_0 LDOS_S(E_f, z_0)$.

In this dissertation STM has been used to investigate semiconductors, that in general don't have available states at the Fermi level, and the LDOS is in general strongly dependent on energy. For this reason, when operating STM the choice of V_0 is important, since depending on its sign and magnitude one can probe empty or filled states (Figure 7.1b). This is even more important in case of III-V semiconductors, where filled and empty states are localized respectively on the V and III species due to the partially ionic bonding, and by switching the sign of the applied voltage one can complementarily probe both species. Changing the amplitude of V_0 is also a practical and quick way to distinguish topographical from electronic structure contrast in an STM image, since the latter are strongly dependent on the value of V_0.

The instrument is usually operated in constant current mode: a tunneling current set-point is fixed and the tip-sample distance z_0 is adjusted through a feedback loop and a height map can be obtained by scanning the tip across the sample.

Now, if V_0 falls within the band gap, there are not allowed states to tunnel and the feedback loop would try to decrease z_0 in order to reach the current set-point. This will continue until the tip crashes into the sample, since in the band gap there are not allowed states, regardless of z_0. For this reason, large biases of up to 3 V have been chosen when investigating cleaned InAs and even more for InAs with a thin thermal oxide layer on top, for which larger band gaps are expected.

STM provided a very useful information about the thermal oxide for passivating an InAs substrate in **Paper II**. An atomically ordered InAs surface has been found after

removing the native oxide with atomic hydrogen (Figure 7.2a), as expected. The thermal oxide was instead characterized by a low local order morphology (Figure 7.2b). This is an interesting result, since it means that the beneficial effects of the passivation with a thermal oxide reported in **Paper II** and by other authors[96] can be obtained even if no local order is preserved, or in other terms with less strict surface morphology control during processing.

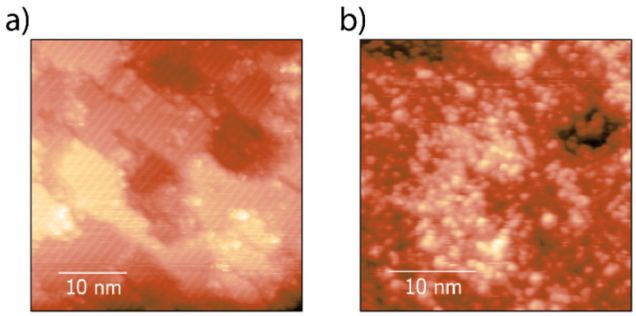

Figure 7.2: STM images of InAs samples a) InAs cleaned surface, rows of the atomic surface reconstruction are visible. Sample bias: 2 V, tunneling current: 130 mA. b) InAs surface after thermal oxidation: no local order is visible. Sample bias: 3 V, tunneling current: 130 mA. [Adapted from Paper II]

7.2 Low Energy Electron Diffraction

A complementary technique for surface analysis that I used in **Paper II** is low energy electron diffraction (LEED)[12, 207]. As the name suggests, this technique is based on the diffraction effect, and it measures symmetries on surfaces having some degree of order. More precisely, in a LEED setup (Figure 7.3a) the sample is exposed to an electron beam and the elastically backscattered electrons from the sample are measured (typically with energies between 10-10^3 eV). It is known that electrons can be considered as waves, and electrons with low energy, i.e. between 20 and 1000 eV, have wavelengths in the range of atomic spacing, and therefore atomic lattices can effectively act as diffraction gratings. The inelastic mean free path of electrons for that energy range is typically of few Å, which ensures that the diffraction peaks originate only from the outermost atomic layers of the surface. The distribution of the diffraction peaks recorded by the phosphor screen of a LEED depends on the pattern of the surface atoms: because of the conservation of electron momentum one can write the diffraction condition[11]: $\boldsymbol{k}_{i,||} = \boldsymbol{k}_{f,||} + \boldsymbol{g}$. where $\boldsymbol{k}_{(i,f),||}$ are the momentum components parallel to the surface respectively of the incident and backscattered electrons, and $\boldsymbol{g}$ is the reciprocal space lattice of the surface, defined as $\boldsymbol{g} = n\boldsymbol{a}^* + m\boldsymbol{b}^* = n\frac{\boldsymbol{a}}{2\pi} + m\frac{\boldsymbol{b}}{2\pi}$, where m and n are integers and ($\mathbf{a}$,$\mathbf{b}$) and ($\mathbf{a}^*$,$\mathbf{b}^*$) are the primitive vectors of real and reciprocal space, respectively. One

can therefore see that diffraction conditions are fulfilled at multiple distances of the reciprocal space unit cell.

It has been mentioned in Chapter 2 that semiconductor surfaces usually undergo reconstructions in order to minimize the surface energy. This rearrangement of the atomic distribution at the surface can result in completely different symmetries from the bulk, and usually the unit cells (or better, *meshes*) on the surface can be much larger than the ones of the bulk. Moreover, adsorbates can also be arranged in a regular array[140, 208] and change the diffraction distribution. Conversely, an amorphous oxide results in the disruption of the diffraction pattern.

In **Paper II**, the surface reconstruction of InAs(100) cleaned with atomic hydrogen was characterized and it was observed that the spots correspond to a 4×2 reconstruction (Figure 7.3b), in agreement with the spacing between the reconstruction meshes seen with STM (Figure 7.2a). This notation embodies information about the regular surface mesh. It was observed that the thin thermal oxide gave a weak 1×1 pattern, which is caused by the underneath InAs substrate (Figure 7.3b), with no ordering present at the surface.

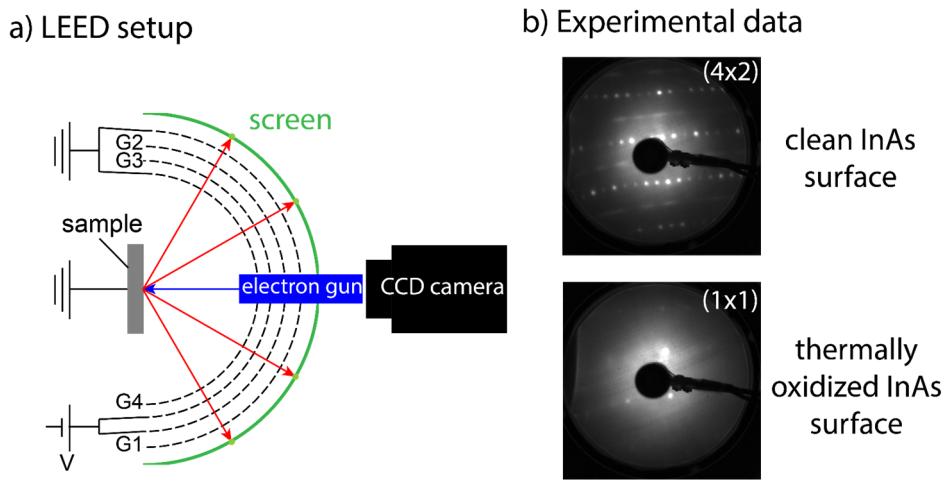

Figure 7.3: a) LEED setup: an electron beam is focused on the sample surface and gets diffracted (red arrows) and accelerated by the grids G1,…,G4 at a potential V. A CCD camera records the spots of a phosphor screen illuminated by the electrons. b) Experimental data of a clean InAs (4x2) and a thermally oxidized InAs (1x1). The LEED was taken with a voltage of 55 V at the grids. [Adapted from [209] and Paper II]

8. Concluding remarks and future developments

General conclusions

From the work discussed in the previous chapters, some general conclusion can be drawn as a common denominator among the variety of methods and samples.

A combination of different synchrotron X-ray based techniques is needed in order to fully characterize novel III-V nanostructures. Laboratory scale tools are still an indispensable fundament to be integrated with synchrotron radiation techniques, that in some cases provide the only possible solution available to fill the gap between processing, modelling and performance.

In this thesis, characterization results that are relevant for the improvement of III-V nanostructures have been presented in parallel with advances in the characterization methods themselves. Proof of principles and new approaches in characterization were successfully demonstrated, which have been shown (**Papers III-VII**) for AP-XPS of an ALD reaction, *operando* SPEM on NW devices, NW doping evaluation by XRF, and XRD imaging of NW arrays. This is just the beginning, these techniques offer a lot of flexibility and different *in situ* / *operando* conditions can be implemented, as mentioned in detail as possible developments at the end of this chapter. The results presented in this thesis can be valuable not only to the III-V community, but to a larger scientific audience.

Specific conclusions

There are also specific conclusions on the experiments which can have a broader relevance or, in other terms, practical indications to III-V nanostructure manufacturing and functionalization, and only the most important ones will be summarized here:

- An effective surface passivation can be obtained through a thermal oxide with specific stoichiometry (**Paper II**). This layer does not need to be crystalline to give improvements, but needs instead to be protected in vacuum. Regarding ALD (**Paper III**), needed afterwards, the AP-XPS puts in evidence the importance of the chemisorption step.

- A new nano-XRF approach for doping assessment in III-V NWs (**Paper V**) revealed that unintentional dopant incorporation can occur during *in situ* doping: this can have strong impact on solar cell performance, and our study highlights the need to investigate more this – rather neglected – aspect. Moreover, measuring dopant gradients is not only an exciting proof of principle of the nano-XRF technique: relying on the good spatial resolution it provides data valuable to verify theoretical models of dopant incorporation in NWs, which is not yet fully understood.
- Doping affects not only the bulk, but also the surface: for this reason, doping effects were studied with XPS based approaches, giving complementary information to nano-XRF. Local electronic effects of doping, such as the built-in potential of a *pn* junction, may differ substantially between the surface and the bulk counterpart (**Paper IV**). Surface and bulk can even respond differently to an externally applied electric field, which is especially important for NWs, where the surface can dominate the entire device behavior. The incorporation of dopants at the surface can also strongly affect the surface chemistry and morphology of NWs, and it has been shown that strong *p* doping of NWs produced via aerotaxy can inhibit the growth of the native oxide (**Paper I**), which can be an interesting side effect in surface passivation of highly doped NWs.
- Finally, FFXDM showed the strong correlation between structure and growth parameters of nano-pyramids for LEDs (**Papers VI and VII**). The statistically robust results gave clear indications towards NW processing in order to fabricate more homogeneous structures.

Possible developments

Beyond the results presented in this thesis a number of specific future extensions with exciting relevance for III-V nanostructures are suggested here:

- It would be interesting to extend the thermal oxide passivation approach to other III-V materials, characterize it with XPS as in **Paper II** and see if improvements in electrical behavior are obtained.
- It was observed that a thermal oxide layer has a reproducible stoichiometry, different to that of the native oxide (**Paper II**). It would be interesting to study the effect of self-cleaning of ALD on this oxide with AP-XPS (like in **Paper III**), since it was noted that the self-cleaning is not homogeneous, but starts from the less stable oxides (As_2O_5), later involving In-oxides and As_2O_3. One may expect different time scales and efficiency for the self-cleaning effect when starting from the thermal oxide with a different stoichiometry, which might result in an improved quality of the semiconductor/high-κ oxide interface.

- The III-V interfaces between semiconductor and high-κ oxide obtained by ALD are still critical. Ongoing XPS studies suggest that the interfacial III-V oxide is selectively removed by hydrogen cleaning on III-V substrates (InAs, GaAs) covered by thin high-κ layers, which itself seem to remain unaffected by the process. While the chemistry can be known from XPS, it would be interesting to probe the surface electronic state and the local structure by using STM and scanning tunneling spectroscopy (STS). An in progress experiment suggests that STS across thin high-κ layers is possible. STS and STM could monitor the evolution of the surface electronic states.

- The incorporation of Zn dopant is difficult to model, and can have strong effects not only on the bulk but also on the surface of NWs. Moreover, not all incorporated dopant atoms are necessarily electronically active dopants. Additional information about this aspect may be obtained by combining a nano-XRF campaign with a nano-Extended X-ray Absorption Fine Structure (nano-EXAFS) experiment around the Zn-K_α absorption edge. The absorption fine structure would put in evidence the local chemical environment of the dopants, contributing to understand how the dopants are incorporated.

- An interesting effect which has been seen in SPEM is that a current run along a NW causes a reduction of the amount of native oxide. This could be a very useful cleaning technique, since it is not requiring any chemicals and that can be easily integrated in device fabrication and testing. Further investigation would be needed, by for instance performing and comparing electrical measurements on a sample cleaned with a standard technique (e.g. annealing with atomic H) and with this new approach.

- An interesting current development of spatially resolved XPS consists in the so called dynamic high pressure XPS[158, 210], which is basically a combination of SPEM with AP-XPS, by introducing gases through a very thin nozzle around the sample, creating steep local pressure gradients. Even if restrictions are present on the gas type (e.g. it is not possible to mimic ALD in this setup like in **Paper III**), *in situ* experiments, like controlled oxidation or nitridation, which may affect the surface state of NWs, are an interesting possibility.

- Strain and tilt are difficult to disentangle in a FFXDM experiment. This aspect could be better understood by performing FFXDM on different Bragg reflections. A structural simulation of the nano-pyramid arrays made with finite element modeling (FEM) might be very useful for completing the interpretation of the FFXDM data.

The motivation of this thesis consisted in moving one step forward towards more efficient novel devices and it has been demonstrated that only a combination of cutting edge characterization tools can fill the gap between processing and performance. Moreover, it has been shown that in nanoscience surface, bulk, and electronic properties cannot be treated as compartmentalized topics, but they coexist and interact in the same system, and all of them need to be kept into consideration simultaneously to obtain more efficient devices.

References

1. Cook, J.; Oreskes, N.; Doran, P., T.; Anderegg, W., R. L.; Verheggen, B.; Maibach, E., W. ; Stuart, C., J.; Lewandowsky, S.; G. Skuce, A.; Green, S., A.; Nuccitelli, D.; Jacobs, P.; Richardson, M.; Winkler, B.; Painting, R.; Rice, K., Consensus on consensus: a synthesis of consensus estimates on human-caused global warming. *Environmental Research Letters* **2016,** *11* (4), 048002.
2. O'Mara, W.; Herring, R. B.; Hunt, L. P., *Handbook of Semiconductor Silicon Technology*. Crest Publishing House: 2007; p 816.
3. Takagi, S.; Zhang, R.; Suh, J.; Kim, S.-H.; Yokoyama, M.; Nishi, K.; Takenaka, M., III–V/Ge channel MOS device technologies in nano CMOS era. *Japanese Journal of Applied Physics* **2015,** *54* (6S1), 06FA01.
4. del Alamo, J. A., Nanometre-scale electronics with III-V compound semiconductors. *Nature* **2011,** *479* (7373), 317-323.
5. Mårtensson, T.; Svensson, C. P. T.; Wacaser, B. A.; Larsson, M. W.; Seifert, W.; Deppert, K.; Gustafsson, A.; Wallenberg, L. R.; Samuelson, L., Epitaxial III−V Nanowires on Silicon. *Nano Letters* **2004,** *4* (10), 1987-1990.
6. Oktyabrsky, S., *Fundamentals of iii-v semiconductor mosfets*. Springer: [Place of publication not identified], 2014.
7. Sze, S. M., *Physics of semiconductor devices*. Interscience: New York, 1969.
8. Neamen, D. A., *Semiconductor physics and devices : basic principles*. McGraw-Hill Higher Education: New York, 2012.
9. Wallentin, J.; Borgström, M. T., Doping of semiconductor nanowires. *Journal of Materials Research* **2011,** *26* (17), 2142-2156.
10. Momma, K.; Izumi, F., VESTA 3 for three-dimensional visualization of crystal, volumetric and morphology data. *J. Appl. Crystallogr.* **2011,** *44*, 1272-1276.
11. Mönch, W., *Semiconductor surfaces and interfaces*. Springer: Berlin, 2010.
12. Brillson, L. J., Surfaces and Interfaces of Electronic Materials. **2012**.
13. Burda, C.; Chen, X.; Narayanan, R.; El-Sayed, M. A., Chemistry and Properties of Nanocrystals of Different Shapes. *Chemical Reviews* **2005,** *105* (4), 1025-1102.
14. Davies, J. H., The physics of low-dimensional semiconductors : an introduction. **1998**.
15. Liu, H.; Neal, A. T.; Zhu, Z.; Luo, Z.; Xu, X.; Tománek, D.; Ye, P. D., Phosphorene: An Unexplored 2D Semiconductor with a High Hole Mobility. *ACS Nano* **2014,** *8* (4), 4033-4041.

16. Timm, R.; Hjort, M.; Fian, A.; Thelander, C.; Lind, E.; Andersen, J. N.; Wernersson, L. E.; Mikkelsen, A., Interface composition of atomic layer deposited HfO2 and Al2O3 thin films on InAs studied by X-ray photoemission spectroscopy. *Microelectronic Engineering* **2011,** *88* (7), 1091-1094.
17. Caroff, P.; Bolinsson, J.; Johansson, J., Crystal Phases in III--V Nanowires: From Random Toward Engineered Polytypism. *IEEE Journal of Selected Topics in Quantum Electronics* **2011,** *17* (4), 829-846.
18. Hiruma, K.; Murakoshi, H.; Yazawa, M.; Katsuyama, T., Self-organized growth of GaAsInAs heterostructure nanocylinders by organometallic vapor phase epitaxy. *Journal of Crystal Growth* **1996,** *163* (3), 226-231.
19. Johansson, J.; Dick, K. A., Recent advances in semiconductor nanowire heterostructures. *CrystEngComm* **2011,** *13* (24), 7175-7184.
20. Tomioka, K.; Yoshimura, M.; Fukui, T., A III-V nanowire channel on silicon for high-performance vertical transistors. *Nature* **2012,** *488* (7410), 189-192.
21. Yi, G.-C., *Semiconductor Nanostructures for Optoelectronic Devices Processing, Characterization and Applications*. Springer Berlin: Berlin, 2014.
22. Anttu, N., Geometrical optics, electrostatics, and nanophotonic resonances in absorbing nanowire arrays. *Opt. Lett.* **2013,** *38* (5), 730-732.
23. Svensson, J.; Dey, A. W.; Jacobsson, D.; Wernersson, L. E., III-V Nanowire Complementary Metal-Oxide Semiconductor Transistors Monolithically Integrated on Si. *Nano Letters* **2015,** *15* (12), 7898-7904.
24. Dick, K., A; Caroff, P.; Bolinsson, J.; Messing, M. E.; Johansson, J.; Deppert, K.; Wallenberg, R. L.; Samuelson, L., Control of III–V nanowire crystal structure by growth parameter tuning. *Semiconductor Science and Technology* **2010,** *25* (2), 024009.
25. Hobbs, R. G.; Petkov, N.; Holmes, J. D., Semiconductor Nanowire Fabrication by Bottom-Up and Top-Down Paradigms. *Chemistry of Materials* **2012,** *24* (11), 1975-1991.
26. Mandl, B.; Stangl, J.; Hilner, E.; Zakharov, A. A.; Hillerich, K.; Dey, A. W.; Samuelson, L.; Bauer, G.; Deppert, K.; Mikkelsen, A., Growth Mechanism of Self-Catalyzed Group III−V Nanowires. *Nano Letters* **2010,** *10* (11), 4443-4449.
27. Dagytė, V. Growth and optical properties of III-V semiconductor nanowires: : Studies relevant for solar cells. Doctoral thesis, Solid State Physics, Lund University, Lund, Sweden, 2018.
28. Otnes, G.; Heurlin, M.; Graczyk, M.; Wallentin, J.; Jacobsson, D.; Berg, A.; Maximov, I.; Borgström, M. T., Strategies to obtain pattern fidelity in nanowire growth from large-area surfaces patterned using nanoimprint lithography. *Nano Research* **2016,** *9* (10), 2852-2861.
29. Otnes, G.; Borgström, M. T., Towards high efficiency nanowire solar cells. *Nano Today* **2017,** *12*, 31-45.
30. Wagner, R. S.; Ellis, W. C., Vapor-liquid-solid mechanism of single crystal growth. *Applied Physics Letters* **1964,** *4* (5), 89-90.
31. Hjort, M. III–V Nanowire Surfaces. PhD thesis, Lund University, Lund, 2014.

32. Jacobsson, D.; Panciera, F.; Tersoff, J.; Reuter, M. C.; Lehmann, S.; Hofmann, S.; Dick, K. A.; Ross, F. M., Interface dynamics and crystal phase switching in GaAs nanowires. *Nature* **2016,** *531*, 317.

33. Berg, A.; Lenrick, F.; Vainorius, N.; Beech, J. P.; Wallenberg, L. R.; Borgström, M. T., Growth parameter design for homogeneous material composition in ternary Ga x In 1− x P nanowires. *Nanotechnology* **2015,** *26* (43), 435601.

34. Ameruddin, A. S.; Caroff, P.; Tan, H. H.; Jagadish, C.; Dubrovskii, V. G., Understanding the growth and composition evolution of gold-seeded ternary InGaAs nanowires. *Nanoscale* **2015,** *7* (39), 16266-16272.

35. Bertness, K. A.; Sanford, N. A.; Barker, J. M.; Schlager, J. B.; Roshko, A.; Davydov, A. V.; Levin, I., Catalyst-free growth of GaN nanowires. *Journal of Electronic Materials* **2006,** *35* (4), 576-580.

36. Koester, R.; Hwang, J. S.; Durand, C.; Le Si Dang, D.; Eymery, J., Self-Assembled Growth of Catalyst-Free GaN Wires by MOVPE. *Nanotechnology* **2010,** *21*, 015602.

37. Bi, Z.; Gustafsson, A.; Lenrick, F.; Lindgren, D.; Hultin, O.; Wallenberg, L. R.; Ohlsson, B. J.; Monemar, B.; Samuelson, L., High In-content InGaN nano-pyramids: Tuning crystal homogeneity by optimized nucleation of GaN seeds. *Journal of Applied Physics* **2018,** *123* (2), 025102.

38. Heurlin, M.; Magnusson, M. H.; Lindgren, D.; Ek, M.; Wallenberg, L. R.; Deppert, K.; Samuelson, L., Continuous gas-phase synthesis of nanowires with tunable properties. *Nature* **2012,** *492*, 90.

39. Deppert, K.; Bovin, J.-O.; Malm, J.-O.; Samuelson, L., A new method to fabricate size-selected compound semiconductor nanocrystals: aerotaxy. *Journal of Crystal Growth* **1996,** *169* (1), 13-19.

40. Deppert, K.; Magnusson, M. H.; Samuelson, L.; Malm, J.-O.; Svensson, C.; Bovin, J.-O., Size-selected nanocrystals of III–V semiconductor materials by the aerotaxy method. *Journal of Aerosol Science* **1998,** *29* (5), 737-748.

41. Metaferia, W.; Persson, A. R.; Mergenthaler, K.; Yang, F.; Zhang, W.; Yartsev, A.; Wallenberg, R.; Pistol, M.-E.; Deppert, K.; Samuelson, L.; Magnusson, M. H., GaAsP Nanowires Grown by Aerotaxy. *Nano Letters* **2016,** *16* (9), 5701-5707.

42. Metaferia, W.; Sivakumar, S.; Persson, A. R.; Geijselaers, I.; Wallenberg, R. L.; Deppert, K.; Samuelson, L.; Magnusson, M. H., n -type doping and morphology of GaAs nanowires in Aerotaxy. *Nanotechnology* **2018,** *29* (28), 285601.

43. Barrigón, E.; Hultin, O.; Lindgren, D.; Yadegari, F.; Magnusson, M. H.; Samuelson, L.; Johansson, L. I. M.; Björk, M. T., GaAs Nanowire pn-Junctions Produced by Low-Cost and High-Throughput Aerotaxy. *Nano Letters* **2018,** *18* (2), 1088-1092.

44. Yang, F.; Messing, M. E.; Mergenthaler, K.; Ghasemi, M.; Johansson, J.; Wallenberg, L. R.; Pistol, M.-E.; Deppert, K.; Samuelson, L.; Magnusson, M. H., Zn-doping of GaAs nanowires grown by Aerotaxy. *Journal of Crystal Growth* **2015,** *414*, 181-186.

45. Lenggoro, I. W.; Xia, B.; Okuyama, K.; de la Mora, J. F., Sizing of Colloidal Nanoparticles by Electrospray and Differential Mobility Analyzer Methods. *Langmuir* **2002,** *18* (12), 4584-4591.

46. Algra, R. E.; Verheijen, M. A.; Borgstrom, M. T.; Feiner, L.-F.; Immink, G.; van Enckevort, W. J. P.; Vlieg, E.; Bakkers, E. P. A. M., Twinning superlattices in indium phosphide nanowires. *Nature* **2008,** *456* (7220), 369-372.
47. Cherns, D.; Henley, S. J.; Ponce, F. A., Edge and screw dislocations as nonradiative centers in InGaN/GaN quantum well luminescence. *Applied Physics Letters* **2001,** *78* (18), 2691-2693.
48. Weisbuch, C.; Piccardo, M.; Martinelli, L.; Iveland, J.; Peretti, J.; Speck, J. S., The efficiency challenge of nitride light-emitting diodes for lighting. *physica status solidi (a)* **2015,** *212* (5), 899-913.
49. https://www.nobelprize.org/prizes/physics/2014/press-release/. https://www.nobelprize.org/prizes/physics/2014/press-release/ (accessed 8th of February 2019).
50. Nakamura, S.; Senoh, M.; Iwasa, N.; Nagahama, S., High-Brightness InGaN Blue, Green and Yellow Light-Emitting Diodes with Quantum Well Structures. *Jpn. J. Appl. Phys.* **1995,** *34*, L797.
51. Langer, T.; Kruse, A.; Ketzer, F. A.; Schwiegel, A.; Hoffmann, L.; Jönen, H.; Bremers, H.; Rossow, U.; Hangleiter, A., Origin of the "green gap": Increasing nonradiative recombination in indium-rich GaInN/GaN quantum well structures. *physica status solidi c* **2011,** *8* (7-8), 2170-2172.
52. Zhu, D.; Wallis, D. J.; Humphreys, C. J., Prospects of III-nitride optoelectronics grown on Si. *Reports on Progress in Physics* **2013,** *76* (10), 106501.
53. Vurgaftman, I.; Meyer, J. R., Band parameters for nitrogen-containing semiconductors. *Journal of Applied Physics* **2003,** *94* (6), 3675-3696.
54. Vurgaftman, I.; Meyer, J. R.; Ram-Mohan, L. R., Band parameters for III–V compound semiconductors and their alloys. *Journal of Applied Physics* **2001,** *89* (11), 5815-5875.
55. Waltereit, P.; Brandt, O.; Trampert, A.; Grahn, H. T.; Menniger, J.; Ramsteiner, M.; Reiche, M.; Ploog, K. H., Nitride semiconductors free of electrostatic fields for efficient white light-emitting diodes. *Nature* **2000,** *406*, 865.
56. Speck, J. S.; Chichibu, S. F., Nonpolar and Semipolar Group III Nitride-Based Materials. *MRS Bulletin* **2009,** *34* (5), 304-312.
57. Zhang, Y.; Wu, J.; Aagesen, M.; Liu, H., III–V nanowires and nanowire optoelectronic devices. *Journal of Physics D: Applied Physics* **2015,** *48* (46), 463001.
58. Wallentin, J.; Anttu, N.; Asoli, D.; Huffman, M.; Aberg, I.; Magnusson, M. H.; Siefer, G.; Fuss-Kailuweit, P.; Dimroth, F.; Witzigmann, B.; Xu, H. Q.; Samuelson, L.; Deppert, K.; Borgstrom, M. T., InP Nanowire Array Solar Cells Achieving 13.8% Efficiency by Exceeding the Ray Optics Limit. *Science* **2013,** *339* (6123), 1057-1060.
59. Åberg, I.; Vescovi, G.; Asoli, D.; Naseem, U.; Gilboy, J. P.; Sundvall, C.; Dahlgren, A.; Svensson, K. E.; Anttu, N.; Björk, M. T.; Samuelson, L., A GaAs Nanowire Array Solar Cell With 15.3% Efficiency at 1 Sun. *IEEE Journal of Photovoltaics* **2016,** *6* (1), 185-190.

60. Lee, J.-H., Bulk FinFETs: Design at 14 nm Node and Key Characteristics. In *Nano Devices and Circuit Techniques for Low-Energy Applications and Energy Harvesting*, Kyung, C.-M., Ed. Springer Netherlands: Dordrecht, 2016; pp 33-64.

61. Riel, H.; Wernersson, L.-E.; Hong, M.; del Alamo, J. A., III–V compound semiconductor transistors—from planar to nanowire structures. *MRS Bulletin* **2014,** *39* (8), 668-677.

62. Chen, Q.; Yang, W., (Invited) The Scaling-Down and Performance Optimization of InAs Nanowire Field Effect Transistors. *ECS Transactions* **2018,** *86* (7), 41-49.

63. Wernersson, L.-E., III–V nanowires for logics and beyond. *Microelectronic Engineering* **2015,** *147*, 344-348.

64. Houssa, M.; Chagarov, E.; Kummel, A., Surface Defects and Passivation of Ge and III–V Interfaces. *MRS Bulletin* **2009,** *34* (7), 504-513.

65. Wallace, R. M.; McIntyre, P. C.; Kim, J.; Nishi, Y., Atomic Layer Deposition of Dielectrics on Ge and III–V Materials for Ultrahigh Performance Transistors. *MRS Bulletin* **2009,** *34* (7), 493-503.

66. Winn, D. L.; Hale, M. J.; Grassman, T. J.; Sexton, J. Z.; Kummel, A. C.; Passlack, M.; Droopad, R., Electronic properties of adsorbates on GaAs(001)-c(2×8)/(2×4). *The Journal of Chemical Physics* **2007,** *127* (13), 134705.

67. Robertson, J.; Guo, Y.; Lin, L., Defect state passivation at III-V oxide interfaces for complementary metal–oxide–semiconductor devices. *Journal of Applied Physics* **2015,** *117* (11), 112806.

68. Spicer, W. E.; Lindau, I.; Skeath, P.; Su, C. Y.; Chye, P., Unified Mechanism for Schottky-Barrier Formation and III-V Oxide Interface States. *Physical Review Letters* **1980,** *44* (6), 420-423.

69. Schwartz, G. P., Analysis of Native Oxide-Films and Oxide Substrate Reactions on Iii-V-Semiconductors Using Thermochemical Phase-Diagrams. *Thin Solid Films* **1983,** *103* (1-2), 3-16.

70. Hollinger, G.; Skheytakabbani, R.; Gendry, M., Oxides on Gaas and Inas Surfaces - an X-Ray-Photoelectron-Spectroscopy Study of Reference Compounds and Thin Oxide Layers. *Physical Review B* **1994,** *49* (16), 11159-11167.

71. Hinkle, C.; Brennan, B.; McDonnell, S.; Milojevic, M.; Sonnet, A.; Zhernokletov, D.; Galatage, R.; Vogel, E.; Wallace, R., High-k Oxide Growth on III-V Surfaces: Chemical Bonding and MOSFET Performance. *ECS Transactions* **2011,** *35* (3), 403-413.

72. Wang, W.; Hinkle, C. L.; Vogel, E. M.; Cho, K.; Wallace, R. M., Is interfacial chemistry correlated to gap states for high-k/III–V interfaces? *Microelectronic Engineering* **2011,** *88* (7), 1061-1065.

73. Hinkle, C. L.; Vogel, E. M.; Ye, P. D.; Wallace, R. M., Interfacial chemistry of oxides on InxGa(1−x)As and implications for MOSFET applications. *Current Opinion in Solid State and Materials Science* **2011,** *15* (5), 188-207.

74. Gougousi, T., Atomic layer deposition of high-k dielectrics on III–V semiconductor surfaces. *Progress in Crystal Growth and Characterization of Materials* **2016,** *62* (4), 1-21.

75. Melitz, W.; Shen, J.; Lee, S.; Lee, J. S.; Kummel, A. C.; Droopad, R.; Yu, E. T., Scanning tunneling spectroscopy and Kelvin probe force microscopy investigation of Fermi energy level pinning mechanism on InAs and InGaAs clean surfaces. *Journal of Applied Physics* **2010,** *108* (2).
76. Haruhiro, O.; Jia-Fa, F.; Yasuo, N.; Hirohiko, S.; Masaharu, O., Universal Passivation Effect of (NH 4) 2 S x Treatment on the Surface of III-V Compound Semiconductors. *Japanese Journal of Applied Physics* **1991,** *30* (3A), L322.
77. Chellappan, R. K.; Li, Z. S.; Hughes, G., Synchrotron radiation photoemission study of the thermal annealing and atomic hydrogen cleaning of native oxide covered InAs(100) surfaces. *Applied Surface Science* **2013,** *276*, 609-612.
78. Bell, G. R.; Kaijaks, N. S.; Dixon, R. J.; McConville, C. F., Atomic hydrogen cleaning of polar III–V semiconductor surfaces. *Surface Science* **1998,** *401* (2), 125-137.
79. Martinelli, V.; Šiller, L.; Betti, M. G.; Mariani, C.; del Pennino, U., Surface modification of InAs(110) surface by low energy ion sputtering. *Surface Science* **1997,** *391* (1), 73-80.
80. Tuominen, M.; Lang, J.; Dahl, J.; Kuzmin, M.; Yasir, M.; Makela, J.; Osiecki, J. R.; Schulte, K.; Punkkinen, M. P. J.; Laukkanen, P.; Kokko, K., Oxidized crystalline (3 x 1)-O surface phases of InAs and InSb studied by high-resolution photoelectron spectroscopy. *Applied Physics Letters* **2015,** *106* (1).
81. Galitsyn, Y. G.; Moshchenko, S. P.; Suranov, A. S., Reconstruction transition (4×2) → (2×4) on the (001) surfaces of InAs and GaAs. *Semiconductors* **2000,** *34* (2), 174-180.
82. Haywood, S. K.; Martin, R. W.; Mason, N. J.; Walker, P. J., Growth of InAs by MOVPE using TBAs and TMIn. *Journal of Electronic Materials* **1990,** *19* (8), 783-788.
83. Caymax, M.; Brammertz, G.; Delabie, A.; Sioncke, S.; Lin, D.; Scarrozza, M.; Pourtois, G.; Wang, W.-E.; Meuris, M.; Heyns, M., Interfaces of high-k dielectrics on GaAs: Their common features and the relationship with Fermi level pinning (Invited Paper). *Microelectronic Engineering* **2009,** *86* (7), 1529-1535.
84. Thompson, S. E.; Parthasarathy, S., Moore's law: the future of Si microelectronics. *Materials Today* **2006,** *9* (6), 20-25.
85. Wilk, G. D.; Wallace, R. M.; Anthony, J. M., High-κ gate dielectrics: Current status and materials properties considerations. *Journal of Applied Physics* **2001,** *89* (10), 5243-5275.
86. Huang, M. L.; Chang, Y. C.; Chang, C. H.; Lee, Y. J.; Chang, P.; Kwo, J.; Wu, T. B.; Hong, M., Surface passivation of III-V compound semiconductors using atomic-layer-deposition-grown Al2O3. *Applied Physics Letters* **2005,** *87* (25), 252104.
87. Parsons, G. N.; George, S. M.; Knez, M., Progress and future directions for atomic layer deposition and ALD-based chemistry. *MRS Bulletin* **2011,** *36* (11), 865-871.
88. George, S. M., Atomic Layer Deposition: An Overview. *Chemical Reviews* **2010,** *110* (1), 111-131.

89. Leskelä, M.; Ritala, M., Atomic Layer Deposition Chemistry: Recent Developments and Future Challenges. *Angewandte Chemie International Edition* **2003,** *42* (45), 5548-5554.
90. Kirk, A. P.; Milojevic, M.; Kim, J.; Wallace, R. M., An in situ examination of atomic layer deposited alumina/InAs(100) interfaces. *Applied Physics Letters* **2010,** *96* (20).
91. Milojevic, M.; Aguirre-Tostado, F. S.; Hinkle, C. L.; Kim, H. C.; Vogel, E. M.; Kim, J.; Wallace, R. M., Half-cycle atomic layer deposition reaction studies of Al2 O3 on In0.2 Ga0.8 As (100) surfaces. *Applied Physics Letters* **2008,** *93* (20).
92. Huang, M. L.; Chang, Y. H.; Lin, T. D.; Lin, H. Y.; Liu, Y. T.; Pi, T. W.; Hong, M.; Kwo, J., Growth mechanism of atomic layer deposited Al2O3 on GaAs(001)-4 × 6 surface with trimethylaluminum and water as precursors. *Applied Physics Letters* **2012,** *101* (21), 212101.
93. Hackley, J. C.; Gougousi, T., Properties of atomic layer deposited HfO2 thin films. *Thin Solid Films* **2009,** *517* (24), 6576-6583.
94. Timm, R.; Fian, A.; Hjort, M.; Thelander, C.; Lind, E.; Andersen, J. N.; Wernersson, L.-E.; Mikkelsen, A., Reduction of native oxides on InAs by atomic layer deposited Al2O3 and HfO2. *Applied Physics Letters* **2010,** *97*, 132904.
95. Kang, Y.-S.; Kim, D.-K.; Jeong, K.-S.; Cho, M.-H.; Kim, C. Y.; Chung, K.-B.; Kim, H.; Kim, D.-C., Structural Evolution and the Control of Defects in Atomic Layer Deposited HfO2–Al2O3 Stacked Films on GaAs. *ACS Applied Materials & Interfaces* **2013,** *5* (6), 1982-1989.
96. Ko, H.; Takei, K.; Kapadia, R.; Chuang, S.; Fang, H.; Leu, P. W.; Ganapathi, K.; Plis, E.; Kim, H. S.; Chen, S. Y.; Madsen, M.; Ford, A. C.; Chueh, Y. L.; Krishna, S.; Salahuddin, S.; Javey, A., Ultrathin compound semiconductor on insulator layers for high-performance nanoscale transistors. *Nature* **2010,** *468* (7321), 286-289.
97. Wang, C. H.; Wang, S. W.; Doornbos, G.; Astromskas, G.; Bhuwalka, K.; Contreras-Guerrero, R.; Edirisooriya, M.; Rojas-Ramirez, J. S.; Vellianitis, G.; Oxland, R.; Holland, M. C.; Hsieh, C. H.; Ramvall, P.; Lind, E.; Hsu, W. C.; Wernersson, L.-E.; Droopad, R.; Passlack, M.; Diaz, C. H., InAs hole inversion and bandgap interface state density of 2 × 1011 cm−2 eV−1 at HfO2/InAs interfaces. *Applied Physics Letters* **2013,** *103* (14), 143510.
98. https://www.nobelprize.org/prizes/physics/1901/rontgen/facts/. (accessed 5th of February 2019).
99. McMorrow, D.; Als-Nielsen, J., Elements of modern x-ray physics. **2013**.
100. Baruchel, J., *Neutron and synchrotron radiation for condensed matter studies : HERCULES Higher European Research Course for Users of Large Experimental Systems Vol. 2, Vol. 2*. Springer ; Les Ed. de Physique: Berlin; Heidelberg; Les Ulis, 1994.
101. Willmott, P., An introduction to synchrotron radiation : techniques and applications. **2013**.
102. Margaritondo, G., *Introduction to synchrotron radiation*. Oxford University Press: New York, 1988.
103. Mimura, H.; Handa, S.; Kimura, T.; Yumoto, H.; Yamakawa, D.; Yokoyama, H.; Matsuyama, S.; Inagaki, K.; Yamamura, K.; Sano, Y.; Tamasaku, K.; Nishino, Y.;

Yabashi, M.; Ishikawa, T.; Yamauchi, K., Breaking the 10[thinsp]nm barrier in hard-X-ray focusing. *Nat Phys* **2010,** *6* (2), 122-125.

104. Döring, F.; Robisch, A. L.; Eberl, C.; Osterhoff, M.; Ruhlandt, A.; Liese, T.; Schlenkrich, F.; Hoffmann, S.; Bartels, M.; Salditt, T.; Krebs, H. U., Sub-5 nm hard x-ray point focusing by a combined Kirkpatrick-Baez mirror and multilayer zone plate. *Opt. Express* **2013,** *21* (16), 19311-19323.
105. Hertz, H., Ueber einen Einfluss des ultravioletten Lichtes auf die electrische Entladung. *Annalen der Physik* **1887,** *267* (8), 983-1000.
106. Einstein, A., Über einen die Erzeugung und Verwandlung des Lichtes betreffenden heuristischen Gesichtspunkt. *Annalen der Physik* **1905,** *322* (6), 132-148.
107. Shayesteh, P. Atomic Layer Deposition and Immobilised Molecular Catalysts Studied by In and Ex Situ Electron Spectroscopy. Doctoral thesis, Faculty of Science, Department of Physics, Lund University, Lund, Sweden, 2019.
108. Woodruff, D. P.; Delchar, T. A., *Modern techniques of surface science*. Cambridge Univ. Press: Cambridge, 2003.
109. Hüfner, S., *Photoelectron spectroscopy : principles and applications*. Springer: Berlin, 2003.
110. Johansson, N. Synchrotron-based in situ electron spectroscopy applied to oxide formation and catalysis. Doctoral thesis, Faculty of Science, Department of Physics, Lund University, Lund, Sweden, 2017.
111. Berglund, C. N.; Spicer, W. E., Photoemission Studies of Copper and Silver: Theory. *Physical Review* **1964,** *136* (4A), A1030-A1044.
112. Bagus, P. S.; Ilton, E. S.; Nelin, C. J., The interpretation of XPS spectra: Insights into materials properties. *Surface Science Reports* **2013,** *68* (2), 273-304.
113. Seah, M. P.; Briggs, A. T. R., *Practical surface analysis. Auger and X-ray photoelectron spectroscopy Volume 1 Volume 1*. Wiley: New York, 1990.
114. Andersen, J. N.; Almbladh, C.-O., High resolution core level photoemission of clean and adsorbate covered metal surfaces. *Journal of Physics: Condensed Matter* **2001,** *13* (49), 11267.
115. Koenig, M. F.; Grant, J. T., Comparison of factor analysis and curve-fitting for data analysis in XPS. *Journal of Electron Spectroscopy and Related Phenomena* **1986,** *41* (1), 145-156.
116. Nelin, C. J.; Bagus, P. S.; Brown, M. A.; Sterrer, M.; Freund, H.-J., Analysis of the Broadening of X-ray Photoelectron Spectroscopy Peaks for Ionic Crystals. *Angewandte Chemie International Edition* **2011,** *50* (43), 10174-10177.
117. Cole, R. J.; Brooks, N. J.; Weightman, P., Madelung Potentials and Disorder Broadening of Core Photoemission Spectra in Random Alloys. *Physical Review Letters* **1997,** *78* (19), 3777-3780.
118. Doniach, S.; Sunjic, M., Many-electron singularity in X-ray photoemission and X-ray line spectra from metals. *Journal of Physics C: Solid State Physics* **1970,** *3* (2), 285.
119. https://srdata.nist.gov/xps/main_search_menu.aspx NIST X-ray Photoelectron Spectroscopy Database (accessed 16th of February 2019).

120. Zhang, Z.; Yates, J. T., Band Bending in Semiconductors: Chemical and Physical Consequences at Surfaces and Interfaces. *Chemical Reviews* **2012,** *112* (10), 5520-5551.
121. Waldrop, J. R.; Kowalczyk, S. P.; Grant, R. W., Correlation of Fermi-level energy and chemistry at InP(100) interfaces. *Applied Physics Letters* **1983,** *42* (5), 454-456.
122. Seah, M. P.; Dench, W. A., Quantitative electron spectroscopy of surfaces: A standard data base for electron inelastic mean free paths in solids. *Surface and Interface Analysis* **1979,** *1* (1), 2-11.
123. Jablonski, A.; Powell, C. J., Effective attenuation lengths for quantitative determination of surface composition by Auger-electron spectroscopy and X-ray photoelectron spectroscopy. *Journal of Electron Spectroscopy and Related Phenomena* **2017,** *218*, 1-12.
124. Lindau, I.; Spicer, W. E., The probing depth in photoemission and auger-electron spectroscopy. *Journal of Electron Spectroscopy and Related Phenomena* **1974,** *3* (5), 409-413.
125. Niemantsverdriet, J. W., Spectroscopy in catalysis : an introduction. **2010**.
126. Knudsen, J.; Andersen, J. N.; Schnadt, J., A versatile instrument for ambient pressure x-ray photoelectron spectroscopy: The Lund cell approach. *Surface Science* **2016,** *646*, 160-169.
127. Salmeron, M.; Schlögl, R., Ambient pressure photoelectron spectroscopy: A new tool for surface science and nanotechnology. *Surface Science Reports* **2008,** *63* (4), 169-199.
128. Bluhm, H.; Hävecker, M.; Knop-Gericke, A.; Kiskinova, M.; Schlögl, R.; Salmeron, M., In Situ X-Ray Photoelectron Spectroscopy Studies of Gas-Solid Interfaces at Near-Ambient Conditions. *MRS Bulletin* **2007,** *32* (12), 1022-1030.
129. Arble, C.; Jia, M.; Newberg, J. T., Lab-based ambient pressure X-ray photoelectron spectroscopy from past to present. *Surface Science Reports* **2018,** *73* (2), 37-57.
130. Kaya, S.; Ogasawara, H.; Näslund, L.-Å.; Forsell, J.-O.; Casalongue, H. S.; Miller, D. J.; Nilsson, A., Ambient-pressure photoelectron spectroscopy for heterogeneous catalysis and electrochemistry. *Catalysis Today* **2013,** *205*, 101-105.
131. Schnadt, J.; Knudsen, J.; Andersen, J. N.; Siegbahn, H.; Pietzsch, A.; Hennies, F.; Johansson, N.; Martensson, N.; Ohrwall, G.; Bahr, S.; Mahl, S.; Schaff, O., The new ambient-pressure X-ray photoelectron spectroscopy instrument at MAX-lab. *Journal of Synchrotron Radiation* **2012,** *19* (5), 701-704.
132. Yamamoto, S.; Bluhm, H.; Andersson, K.; Ketteler, G.; Ogasawara, H.; Salmeron, M.; Nilsson, A., In situ x-ray photoelectron spectroscopy studies of water on metals and oxides at ambient conditions. *Journal of Physics: Condensed Matter* **2008,** *20* (18), 184025.
133. Urpelainen, S.; Sathe, C.; Grizolli, W.; Agaker, M.; Head, A. R.; Andersson, M.; Huang, S.-W.; Jensen, B. N.; Wallen, E.; Tarawneh, H.; Sankari, R.; Nyholm, R.; Lindberg, M.; Sjoblom, P.; Johansson, N.; Reinecke, B. N.; Arman, M. A.; Merte, L. R.; Knudsen, J.; Schnadt, J.; Andersen, J. N.; Hennies, F., The SPECIES beamline at the MAX IV Laboratory: a facility for soft X-ray RIXS and APXPS. *Journal of Synchrotron Radiation* **2017,** *24* (1), 344-353.

134. Siegbahn, H.; Siegbahn, K., ESCA applied to liquids. *Journal of Electron Spectroscopy and Related Phenomena* **1973,** *2* (3), 319-325.
135. Joyner, R. W.; Roberts, M. W.; Yates, K., A "high-pressure" electron spectrometer for surface studies. *Surface Science* **1979,** *87* (2), 501-509.
136. Ruppender, H. J.; Grunze, M.; Kong, C. W.; Wilmers, M., In situ X-ray photoelectron spectroscopy of surfaces at pressures up to 1 mbar. *Surface and Interface Analysis* **1990,** *15* (4), 245-253.
137. Shavorskiy, A.; Karslioglu, O.; Zegkinoglou, I.; Bluhm, H., Synchrotron-based Ambient Pressure X-ray Photoelectron Spectroscopy. *Synchrotron Radiation News* **2014,** *27* (2), 14-23.
138. Ogletree, D. F.; Bluhm, H.; Lebedev, G.; Fadley, C. S.; Hussain, Z.; Salmeron, M., A differentially pumped electrostatic lens system for photoemission studies in the millibar range. *Review of Scientific Instruments* **2002,** *73* (11), 3872-3877.
139. Timm, R.; Hjort, M.; Fian, A.; Borg, B. M.; Thelander, C.; Andersen, J. N.; Wernersson, L.-E.; Mikkelsen, A., Interface composition of InAs nanowires with Al2O3 and HfO2 thin films. *Applied Physics Letters* **2011,** *99* (22), 222907.
140. Zhernokletov, D. M.; Laukkanen, P.; Dong, H.; Galatage, R. V.; Brennan, B.; Yakimov, M.; Tokranov, V.; Kim, J.; Oktyabrsky, S.; Wallace, R. M., Surface and interfacial reaction study of InAs(100)-crystalline oxide interface. *Applied Physics Letters* **2013,** *102* (21).
141. He, G.; Chen, X.; Sun, Z., Interface engineering and chemistry of Hf-based high-k dielectrics on III–V substrates. *Surface Science Reports* **2013,** *68* (1), 68-107.
142. Rodríguez-Reyes, J. C. F.; Teplyakov, A. V., Mechanisms of adsorption and decomposition of metal alkylamide precursors for ultrathin film growth. *Journal of Applied Physics* **2008,** *104* (8), 084907.
143. Hayes Griffith, O.; Engel, W., Historical perspective and current trends in emission microscopy, mirror electron microscopy and low-energy electron microscopy: An introduction to the proceedings of the second international symposium and workshop on emission microscopy and related techniques. *Ultramicroscopy* **1991,** *36* (1), 1-28.
144. Günther, S.; Kaulich, B.; Gregoratti, L.; Kiskinova, M., Photoelectron microscopy and applications in surface and materials science. *Progress in Surface Science* **2002,** *70* (4-8), 187-260.
145. Barinov, A.; Dudin, P.; Gregoratti, L.; Locatelli, A.; Onur Menteş, T.; Ángel Niño, M.; Kiskinova, M., Synchrotron-based photoelectron microscopy. *Nuclear Instruments and Methods in Physics Research, Section A: Accelerators, Spectrometers, Detectors and Associated Equipment* **2009,** *601* (1-2), 195-202.
146. Margaritondo, G., Photoelectron spectromicroscopy and spectronanoscopy at synchrotrons: Growing impact on life sciences and materials science. *Journal of Electron Spectroscopy and Related Phenomena* **2010,** *178-179* (C), 273-291.
147. Hitchcock, A. P., Soft X-ray spectromicroscopy and ptychography. *Journal of Electron Spectroscopy and Related Phenomena* **2015,** *200*, 49-63.
148. Casalis, L.; Jark, W.; Kiskinova, M.; Lonza, D.; Melpignano, P.; Morris, D.; Rosei, R.; Savoia, A.; Abrami, A.; Fava, C.; Furlan, P.; Pugliese, R.; Vivoda, D.; Sandrin, G.; Wei, F. Q.; Contarini, S.; DeAngelis, L.; Gariazzo, C.; Nataletti, P.; Morrison, G.

R., ESCA microscopy beamline at ELETTRA. *Review of Scientific Instruments* **1995,** *66* (10), 4870-4875.

149. https://www.elettra.trieste.it/elettra-beamlines/escamicroscopy.html (accessed 31th December 2018).
150. Ade, H.; Kirz, J.; Hulbert, S. L.; Johnson, E. D.; Anderson, E.; Kern, D., X-ray spectromicroscopy with a zone plate generated microprobe. *Applied Physics Letters* **1990,** *56* (19), 1841-1843.
151. Ade, H.; Kirz, J.; Hulbert, S.; Johnson, E.; Anderson, E.; Kern, D., Images of a microelectronic device with the X1-SPEM, a first generation scanning photoemission microscope at the National Synchrotron Light Source. *Journal of Vacuum Science and Technology A: Vacuum, Surfaces and Films* **1991,** *9* (3), 1902-1906.
152. Ko, C. H.; Kirz, J.; Ade, H.; Johnson, E.; Hulbert, S.; Anderson, E., Development of a second generation scanning photoemission microscope with a zone plate generated microprobe at the National Synchrotron Light Source. *Review of Scientific Instruments* **1995,** *66* (2), 1416-1418.
153. Chao, W.; Harteneck, B. D.; Liddle, J. A.; Anderson, E. H.; Attwood, D. T., Soft X-ray microscopy at a spatial resolution better than 15 nm. *Nature* **2005,** *435*, 1210.
154. Chao, W.; Kim, J.; Rekawa, S.; Fischer, P.; Anderson, E. H., Demonstration of 12 nm Resolution Fresnel Zone Plate Lens based Soft X-ray Microscopy. *Opt. Express* **2009,** *17* (20), 17669-17677.
155. Li, K.; Jacobsen, C., More are better, but the details matter: combinations of multiple Fresnel zone plates for improved resolution and efficiency in X-ray microscopy. *Journal of Synchrotron Radiation* **2018,** *25* (4), 1048-1059.
156. Rösner, B.; Koch, F.; Döring, F.; Guzenko, V. A.; Meyer, M.; Ornelas, J. L.; Späth, A.; Fink, R. H.; Stanescu, S.; Swaraj, S.; Belkhou, R.; Watts, B.; Raabe, J.; David, C., 7 nm Spatial Resolution in Soft X-ray Microscopy. *Microscopy and Microanalysis* **2018,** *24* (S2), 270-271.
157. Avila, J.; Razado-Colambo, I.; Lorcy, S.; Lagarde, B.; Giorgetta, J.-L.; Polack, F.; C. Asensio, M., ANTARES, a scanning photoemission microscopy beamline at SOLEIL. *Journal of Physics: Conference Series* **2013,** *425* (19), 192023.
158. Amati, M.; Barinov, A.; Feyer, V.; Gregoratti, L.; Al-Hada, M.; Locatelli, A.; Mentes, T. O.; Sezen, H.; Schneider, C. M.; Kiskinova, M., Photoelectron microscopy at Elettra: Recent advances and perspectives. *Journal of Electron Spectroscopy and Related Phenomena* **2018,** *224*, 59-67.
159. Abyaneh, M. K.; Gregoratti, L.; Amati, M.; Dalmiglio, M.; Kiskinova, M., Scanning Photoelectron Microscopy: a Powerful Technique for Probing Micro and Nano-Structures. *e-Journal of Surface Science and Nanotechnology* **2011,** *9*, 158-162.
160. Zakharov, A. A.; A.Mikkelsen; Andersen, J. N., Recent advances in imaging of properties and growth of low dimensional structures for photonics and electronics by XPEEM. *Journal of Electron Spectroscopy and Related Phenomena* **2012,** *185* (10), 417-428.
161. Otnes, G.; Barrigón, E.; Sundvall, C.; Svensson, K. E.; Heurlin, M.; Siefer, G.; Samuelson, L.; Åberg, I.; Borgström, M. T., Understanding InP Nanowire Array

Solar Cell Performance by Nanoprobe-Enabled Single Nanowire Measurements. *Nano Letters* **2018,** *18* (5), 3038-3046.

162. Black, L. E.; Cavalli, A.; Verheijen, M. A.; Haverkort, J. E. M.; Bakkers, E. P. A. M.; Kessels, W. M. M., Effective Surface Passivation of InP Nanowires by Atomic-Layer-Deposited Al2O3 with POx Interlayer. *Nano Letters* **2017,** *17* (10), 6287-6294.
163. Chia, A. C. E.; LaPierre, R. R., Analytical model of surface depletion in GaAs nanowires. *Journal of Applied Physics* **2012,** *112* (6), 063705.
164. Fanetti, M.; Ambrosini, S.; Amati, M.; Gregoratti, L.; Abyaneh, M. K.; Franciosi, A.; Chia, A. C. E.; LaPierre, R. R.; Rubini, S., Monitoring the Fermi-level position within the bandgap on a single nanowire: A tool for local investigations of doping. *Journal of Applied Physics* **2013,** *114* (15).
165. Persson, O.; Webb, J. L.; Dick, K. A.; Thelander, C.; Mikkelsen, A.; Timm, R., Scanning Tunneling Spectroscopy on InAs–GaSb Esaki Diode Nanowire Devices during Operation. *Nano Letters* **2015,** *15* (6), 3684-3691.
166. Hjort, M.; Wallentin, J.; Timm, R.; Zakharov, A. A.; Håkanson, U.; Andersen, J. N.; Lundgren, E.; Samuelson, L.; Borgström, M. T.; Mikkelsen, A., Surface Chemistry, Structure, and Electronic Properties from Microns to the Atomic Scale of Axially Doped Semiconductor Nanowires. *ACS Nano* **2012,** *6* (11), 9679-9689.
167. Kronik, L.; Shapira, Y., Surface photovoltage phenomena: theory, experiment, and applications. *Surface Science Reports* **1999,** *37* (1), 1-206.
168. Renault, O.; Morin, J.; Tchoulfian, P.; Chevalier, N.; Feyer, V.; Pernot, J.; Schneider, C. M., Spectroscopic XPEEM of highly conductive SI-doped GaN wires. *Ultramicroscopy* **2015,** *159*, 476-481.
169. Webb, J. L.; Knutsson, J.; Hjort, M.; McKibbin, S. R.; Lehmann, S.; Thelander, C.; Dick, K. A.; Timm, R.; Mikkelsen, A., Imaging Atomic Scale Dynamics on III-V Nanowire Surfaces During Electrical Operation. *Sci Rep-Uk* **2017,** *7*.
170. Melitz, W.; Shen, J.; Kummel, A. C.; Lee, S., Kelvin probe force microscopy and its application. *Surface Science Reports* **2011,** *66* (1), 1-27.
171. Duan, X.; Huang, Y.; Cui, Y.; Wang, J.; Lieber, C. M., Indium phosphide nanowires as building blocks for nanoscale electronic and optoelectronic devices. *Nature* **2001,** *409*, 66.
172. Li, N.; Tan, T. Y.; Gosele, U., Transition region width of nanowire hetero- and pn-junctions grown using vapor-liquid-solid processes. *Applied Physics a-Materials Science & Processing* **2008,** *90* (4), 591-596.
173. Otnes, G.; Heurlin, M.; Zeng, X.; Borgström, M. T., InxGa1–xP Nanowire Growth Dynamics Strongly Affected by Doping Using Diethylzinc. *Nano Letters* **2017,** *17* (2), 702-707.
174. De Boer, D. K. G., Calculation of x-ray fluorescence intensities from bulk and multilayer samples. *X-Ray Spectrometry* **1990,** *19* (3), 145-154.
175. Sherman, J., The theoretical derivation of fluorescent X-ray intensities from mixtures. *Spectrochimica Acta* **1955,** *7*, 283-306.

176. Solé, V. A.; Papillon, E.; Cotte, M.; Walter, P.; Susini, J., A multiplatform code for the analysis of energy-dispersive X-ray fluorescence spectra. *Spectrochimica Acta Part B: Atomic Spectroscopy* **2007,** *62* (1), 63-68.

177. Shiraiwa, T.; Fujino, N., Theoretical Calculation of Fluorescent X-Ray Intensities in Fluorescent X-Ray Spectrochemical Analysis. *Japanese Journal of Applied Physics* **1966,** *5* (10), 886.

178. Grieken, R. v.; Markowicz, A., *Handbook of X-ray spectrometry*. Marcel Dekker: New York, 2002.

179. Thompson, A. C.; Center for, X. r. O.; Lawrence Berkeley National, L.; Advanced Light, S., *X-ray data booklet*. Lawrence Berkeley National Laboratory, University of California: Berkeley, Calif., 2001.

180. Sitko, R.; Zawisz, B., Quantification in X-Ray Fluorescence Spectrometry. In *X-ray Spectroscopy*, Sharma, S. K., Ed. InTechOpen: 2012.

181. Solé, V. A., Manual for PyMCA software. ESRF: 2016.

182. Henke, B. L.; Gullikson, E. M.; Davis, J. C., X-Ray Interactions: Photoabsorption, Scattering, Transmission, and Reflection at E = 50–30000 eV, Z = 1–92. *At. Data Nucl. Data Tables* **1993,** *54*, 181.

183. Martinez-Criado, G.; Villanova, J.; Tucoulou, R.; Salomon, D.; Suuronen, J. P.; Laboure, S.; Guilloud, C.; Valls, V.; Barrett, R.; Gagliardini, E.; Dabin, Y.; Baker, R.; Bohic, S.; Cohen, C.; Morse, J., ID16B: a hard X-ray nanoprobe beamline at the ESRF for nano-analysis. *Journal of Synchrotron Radiation* **2016,** *23*, 344-352.

184. Dayeh, S. A.; Chen, R.; Ro, Y. G.; Sim, J., Progress in doping semiconductor nanowires during growth. *Materials Science in Semiconductor Processing* **2017,** *62* (Supplement C), 135-155.

185. Perea, D. E.; Lensch, J. L.; May, S. J.; Wessels, B. W.; Lauhon, L. J., Composition analysis of single semiconductor nanowires using pulsed-laser atom probe tomography. *Applied Physics A* **2006,** *85* (3), 271-275.

186. Perea, D. E.; Hemesath, E. R.; Schwalbach, E. J.; Lensch-Falk, J. L.; Voorhees, P. W.; Lauhon, L. J., Direct measurement of dopant distribution in an individual vapour–liquid–solid nanowire. *Nature Nanotechnology* **2009,** *4*, 315.

187. Chayanun, L.; Dagytė, V.; Troian, A.; Salomon, D.; Borgström, M.; Wallentin, J., Spectrally resolved x-ray beam induced current in a single InGaP nanowire. *Nanotechnology* **2018,** *29* (45), 454001.

188. Kriegner, D.; Persson, J. M.; Etzelstorfer, T.; Jacobsson, D.; Wallentin, J.; Wagner, J. B.; Deppert, K.; Borgström, M. T.; Stangl, J., Structural investigation of GaInP nanowires using X-ray diffraction. *Thin Solid Films* **2013,** *543*, 100-105.

189. Dick, K. A.; Bolinsson, J.; Borg, B. M.; Johansson, J., Controlling the Abruptness of Axial Heterojunctions in III–V Nanowires: Beyond the Reservoir Effect. *Nano Letters* **2012,** *12* (6), 3200-3206.

190. Hjort, M.; Wallentin, J.; Timm, R.; Zakharov, A. A.; Andersen, J. N.; Samuelson, L.; Borgström, M. T.; Mikkelsen, A., Doping profile of InP nanowires directly imaged by photoemission electron microscopy. *Applied Physics Letters* **2011,** *99* (23), 233113.

191. Warren, B. E., *X-ray diffraction*. Reading, Mass. : Addison-Wesley, cop. 1969: 1969.
192. Miao, J.; Ishikawa, T.; Robinson, I. K.; Murnane, M. M., Beyond crystallography: Diffractive imaging using coherent x-ray light sources. *Science* **2015,** *348* (6234), 530.
193. Stankevič, T.; Hilner, E.; Seiboth, F.; Ciechonski, R.; Vescovi, G.; Kryliouk, O.; Johansson, U.; Samuelson, L.; Wellenreuther, G.; Falkenberg, G.; Feidenhans'l, R.; Mikkelsen, A., Fast Strain Mapping of Nanowire Light-Emitting Diodes Using Nanofocused X-ray Beams. *ACS Nano* **2015,** *9* (7), 6978-6984.
194. Stankevič, T.; Dzhigaev, D.; Bi, Z.; Rose, M.; Shabalin, A.; Reinhardt, J.; Mikkelsen, A.; Samuelson, L.; Falkenberg, G.; Vartanyants, I. A.; Feidenhans'l, R., Strain mapping in an InGaN/GaN nanowire using a nano-focused x-ray beam. *Applied Physics Letters* **2015,** *107* (10), 103101.
195. Snigirev, A.; Kohn, V.; Snigireva, I.; Souvorov, A.; Lengeler, B., Focusing high-energy x rays by compound refractive lenses. *Appl. Opt.* **1998,** *37* (4), 653-662.
196. Simons, H.; King, A.; Ludwig, W.; Detlefs, C.; Pantleon, W.; Schmidt, S.; Stöhr, F.; Snigireva, I.; Snigirev, A.; Poulsen, H. F., Dark-field X-ray microscopy for multiscale structural characterization. *Nature Communications* **2015,** *6*, 6098.
197. Schülli, T. U.; Leake, S. J., X-ray nanobeam diffraction imaging of materials. *Current Opinion in Solid State and Materials Science* **2018,** *22* (5), 188-201.
198. ESRF ID01 beamline web page. http://www.esrf.eu/home/UsersAndScience/Experiments/XNP/ID01/new-frontpage-files/FFDXM.html (accessed 17/01/2019).
199. Hilhorst, J.; Marschall, F.; Tran Thi, T. N.; Last, A.; Schulli, T. U., Full-field X-ray diffraction microscopy using polymeric compound refractive lenses. *Journal of Applied Crystallography* **2014,** *47* (6), 1882-1888.
200. Bi, Z.; Lenrick, F.; Colvin, J.; Gustafsson, A.; Hultin, O.; Nowzari, A.; Lu, T.; Wallenberg, L.; Timm, R.; Mikkelsen, A.; Ohlsson, B. J.; Storm, K.; Monemar, B.; Samuelson, L., InGaN platelets: synthesis and applications towards green and red light emitting diodes. *Submitted* **2019**.
201. Fini, P.; Marchand, H.; Ibbetson, J. P.; DenBaars, S. P.; Mishra, U. K.; Speck, J. S., Determination of tilt in the lateral epitaxial overgrowth of GaN using X-ray diffraction. *Journal of Crystal Growth* **2000,** *209* (4), 581-590.
202. Wernicke, T.; Schade, L.; Netzel, C.; Rass, J.; Hoffmann, V.; Ploch, S.; Knauer, A.; Weyers, M.; Schwarz, U.; Kneissl, M., Indium incorporation and emission wavelength of polar, nonpolar and semipolar InGaN quantum wells. *Semiconductor Science and Technology* **2012,** *27* (2), 024014.
203. Voigtländer, B., Scanning probe microscopy : atomic force microscopy and scanning tunneling microscopy. **2015**.
204. Hawkes, P. W.; Spence, J. C. H. e., *SCIENCE OF MICROSCOPY*. SPRINGER: 2016.
205. Bardeen, J., Tunnelling from a Many-Particle Point of View. *Physical Review Letters* **1961,** *6* (2), 57-59.

206. Tersoff, J.; Hamann, D. R., Theory of the scanning tunneling microscope. *Physical Review B* **1985,** *31* (2), 805-813.
207. Attard, G.; Barnes, C., *Surfaces*. Oxford University Press: Oxford, 2011.
208. Qin, X.; Wang, W.-E.; Droopad, R.; Rodder, M. S.; Wallace, R. M., A crystalline oxide passivation on In0.53Ga0.47As (100). *Journal of Applied Physics* **2017,** *121* (12), 125302.
209. Rullik, L. Industrial Alloys Studied by Surface Sensitive Techniques. Doctoral thesis, Faculty of Science, Physics Department, Lund university, Lund, Sweden, 2018.
210. Gregoratti, L.; Al-Hada, M.; Amati, M.; Brescia, R.; Roccella, D.; Sezen, H.; Zeller, P., Spatially Resolved Photoelectron Spectroscopy from Ultra-high Vacuum to Near Ambient Pressure Sample Environments. *Topics in Catalysis* **2018,** *61* (12), 1274-1282.

Printed by Media-Tryck, Lund 2019 NORDIC SWAN ECOLABEL 3041 0903

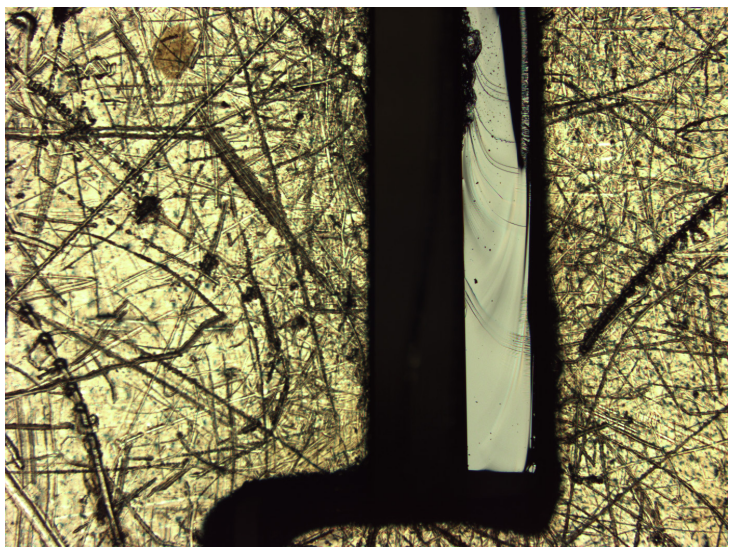

Even Pollock would have loved doing cross-sectional STM!

Faculty of Science
Department of Physics
Division of Synchrotron Radiation Research
Lund University
ISBN 978-91-7753-978-0